Role of Print Architecture on Fracture Behavior of Additively Manufactured ABS: Opto-Mechanical Investigations

by

John Ponniah Isaac

A dissertation submitted to the Graduate Faculty of
Auburn University
in partial fulfillment of the
requirements for the Degree of
Doctor of Philosophy

Auburn, Alabama
May 6, 2023

Keywords: Additive Manufacturing, Fracture Mechanics, Digital Image Correlation, Strain Rate Effects, Material Characterization

Approved by

Hareesh V. Tippur, Chair, McWane Professor of Mechanical Engineering
Jeffrey C. Suhling, Quina Distinguished Professor of Mechanical Engineering
Nima Shamsaei, Philpott-WestPoint Stevens Distinguished Professor of Mechanical Engineering
James S. Davidson, Gottlieb Professor of Civil Engineering

Abstract

Acrylonitrile Butadiene Styrene or ABS is a popular and inexpensive isotropic, amorphous thermoplastic widely used for Additive Manufacturing (AM) of engineering parts. An AM process called Fused Filament Fabrication (FFF) that involves layer-by-layer deposition of melted thermoplastic wire through a heated nozzle along predetermined paths is common for printing thermoplastics such as ABS. Individual layers printed during AM can be configured differently and could introduce anisotropy into the part due to weaker planes between individual beads even when the feedstock is isotropic. The feasibility of tailoring these individual layers in different directions and designing print architectures introduces uncertainty in the mechanical behavior of AM parts. Hence, the role of the print architecture on mechanical failure and fracture properties must be critically evaluated. In this work, AM ABS parts with three different in-plane print architectures, namely $[0^o/90^o]_n$, $[45^o/-45^o]_{n,}$ and $[0^o/45^o/90^o/-45^o]_n$, are considered and their elastic and fracture properties have been evaluated under quasi-static and high strain rate loading using full-field optical techniques used in conjunction with a hybrid experimental-numerical method.

The full-field measurement of local in-plane displacements is performed optically up to crack initiation and during crack growth using Digital Image Correlation (DIC) method in quasi-statically and dynamically loaded AM ABS specimens. The early part of the dissertation details the challenges associated with the prevailing approaches of extracting fracture properties from full-field displacement data obtained from DIC. To overcome the limitations, a method of analyzing DIC data by transferring it to a corresponding Finite Element (FE) model for computing the energy release rate as the *J*-integral and then partitioning it into individual stress intensity factors is developed. Details of this "Hybrid DIC-FE" methodology are presented before undertaking experimental work.

In the next part of the work, the tensile and fracture behaviors of three in-plane print architectures, namely $[0^o/90^o]_n$, $[45^o/-45^o]_n$, and $[0^o/45^o/90^o/-45^o]_n$ orientations, under quasi-static loading conditions are examined. Uniaxial tension experiments are performed on dog-bone-shaped AM ABS specimens and quasi-static fracture experiments on edge-notched symmetric three-point bend specimens using a universal testing machine. Even though the printed architectures show macroscopic elastic isotropy, significant differences in the failure strain, crack initiation and growth parameters, and failure modes among the three architectures are observed. These differences are explained using tests performed on comparable unidirectional prints. The results suggest that $[0^o/45^o/90^o/-45^o]_n$ is preferable to the other two more common configurations for a relatively gradual failure behavior and higher resistance to crack growth.

The next part examines the high strain rate fracture behaviors of three different print architectures, namely $[0^o/90^o]_n$, $[45^o/-45^o]_n$, and $[0^o/45^o/90^o/-45^o]_n$ in-plane orientations, under stress-wave loading conditions and compares the results with the quasi-static counterparts. Elastic properties under high strain rate loading are measured on printed cubes using ultrasonic transducers. The high strain rate fracture experiments are carried out on V-notched AM ABS specimens using a modified-Hopkinson pressure bar apparatus. Distinct crack initiation and growth behaviors with different failure modes are observed in the three architectures under quasi-static and high strain rate loading conditions despite macroscale elastic isotropy. The results favor $[0^o/45^o/90^o/-45^o]_n$ architecture due to a better crack growth behavior relative to the other two print architectures, suggesting that the fracture performance can be enhanced via print architecture.

The final section of this dissertation details the effect of print architecture on the mixed-mode fracture behavior of AM ABS specimens. An Arcan loading apparatus that allows for direct optical measurements in the crack tip vicinity is developed and mixed-mode (I/II) experiments

under quasi-static loading are performed for the three architectures studied in this work. Distinct failure loads, load-point displacement at failure, and failure modes are observed under different loading conditions ranging from mode-I, mixed-mode (I/II), and mode-II conditions. The optical measurements from DIC are used with the hybrid DIC-FE methodology to extract energy release rates and stress intensity factors. The critical values at crack initiation are identified and the fracture envelopes are plotted to evaluate the mixed-mode (I/II) performance for all three architectures. Significant differences in the behaviors are observed, with the $[0^o/45^o/90^o/-45^o]_n$ architecture having a better fracture profile among the three architectures studied. Fracture mechanisms at play are further explained via fractography using images of crack paths and fractured cross-sections.

Acknowledgments

I would like to thank my advisor Dr. Hareesh V. Tippur for providing me with a great opportunity to join his research group at Auburn University. It would be very remiss of me not to acknowledge the amount of time and effort he has spent on me to shape my professional career. His constant support and guidance have made this dissertation possible. I am immensely grateful to Dr. Jeffrey Suhling for providing me with an assistantship when I joined Auburn. Without him, this journey wouldn't have begun. I would like to thank my committee members Dr. Jeffrey Suhling, Dr. Nima Shamsaei, and Dr. James Davidson for supporting my research and serving on my defense. I would like to acknowledge Dr. Daniel Silva for serving as the graduate school representative for my dissertation. Additionally, I would like to thank Dr. Shamsaei for allowing me to work with the National Center for Additive Manufacturing Excellence (NCAME). Also, I would like to express my sincere appreciation to Dr. Prabhakar Clement for continuing to be an exceptional mentor from my undergraduate years.

The friendships and memories from my time in Auburn are something that I will cherish and remember fondly. My friends Bhargav, Abhishek, Robin, Vignesh, Arjun, Akshay, Ravi, and Siva have been a positive influence and helped me in more ways than I can imagine.

Last but not the least, I would like to thank my parents- J.P. Isaac and Beulah Rubarani, for all their love and unwavering belief in me. Everything I possess and value in my life stems from their sacrifice and relentless support. I am thankful to my wife, Joyce, for always being there for me. Her continued motivation has inspired me to be a better person. I dedicate this dissertation to my parents and wife.

Table of Contents

List of Tables

List of Figures

List of Abbreviations

A1	$[0^o/90^o]_n$ Architecture
A2	$[45^o/-45^o]_n$ Architecture
A3	$[0^o/45^o/90^o/-45^o]_n$ Architecture
ABS	Acrylonitrile Butadiene Styrene
AM	Additive Manufacturing/Manufactured
BAAM	Big Area Additive Manufacturing
CAD	Computer-Aided Design
DIC	Digital Image Correlation
FDM	Fused Deposition Modelling
FE/FEA	Finite Element Analysis
FFF	Fused Filament Fabrication
GMTS	Generalized Maximum Tangential Stress
LEFM	Linear Elastic Fracture Mechanics
MTS	Maximum Tangential Stress
PA	Polyamide-12
PET	Polyethylene Terephthalate
PLA	Polylactic Acid
PVA	Polyvinyl Alcohol
ROI	Region-Of-Interest
SCB	Semi-Circular Beam
TPU	Thermoplastic Polyurethane

Chapter 1. Introduction

1.1 Motivation

Additive Manufacturing (AM) has become a popular advanced manufacturing process for building 3D objects layer-by-layer [1]. AM was introduced first in the 1980s to aid in the specialized needs of model-making and rapid prototyping[2, 3]. With the eventual growth of computer-aided design (CAD) and manufacturing capabilities, AM or 3D printing has seen tremendous growth in the past decade. Figure 1.1 demonstrates the basic principles involved in the AM process [4]. The first step in the AM process is to design the object of interest (in this case, the coffee mug) using CAD. Then the design is sliced digitally into layers in the next step. The sliced layer information and the dimensions of the object are used to generate the material deposition paths that will drive the nozzle of the machine in specified paths to manufacture the desired object. Fabricating objects with overhanging portions (in this case, the handles of the mug) is made possible by designing support structures that are easy to remove during the post-printing step. AM provides the ability to manufacture multifunctional parts with complex geometries with relative ease compared to traditional practices for polymers such as injection molding. With the potential to decrease the lead manufacturing time and lower the weight of structural components by optimizing the deposition paths [5], AM has established itself as the leading manufacturing technique of this generation. Engineering parts of different materials such as plastics, metals, and ceramics, are currently being manufactured through AM. Because of its capability to produce parts with complex geometries on demand and/or in limited quantities, AM has been incorporated in all

major technology sectors globally and has found numerous applications in the automotive, aerospace, and medical industries. According to a recent report on the industry adoption of AM [6], 47% of manufacturers, 22.1% of automotive manufacturers, 12.5% of product development manufacturers, and 4.8% of medical manufacturers utilize AM. The use of AM in the aerospace, education, defense, construction, and electronics industries has also been on the rise. With the unprecedented growth of AM, failure characterization must be carried out to evaluate the potential adverse effects that may arise in the service of AM engineering parts.

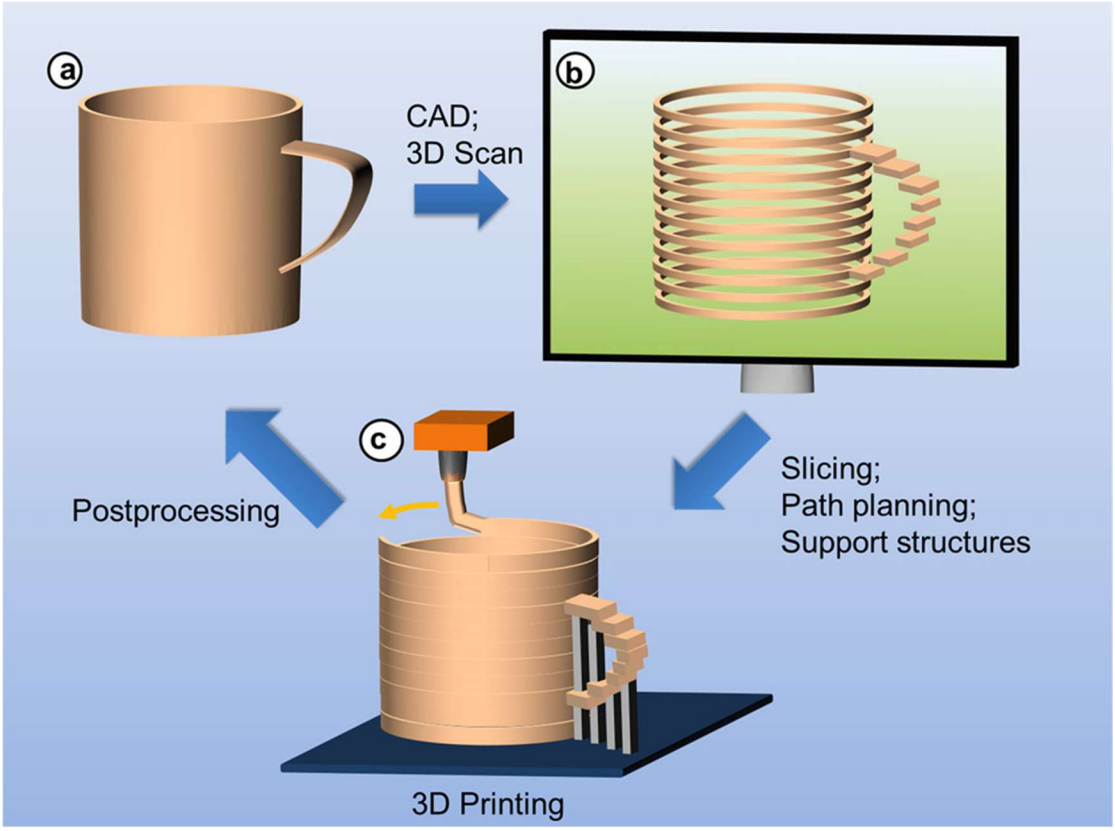

Figure 1.1: Demonstration of steps involved in Additive Manufacturing or 3D printing [4].

Based on the principle behind the solidification process, AM can be classified into different groups such as material extrusion, vat polymerization, directed energy deposition, powder bed fusion, etc. Fused Filament Fabrication (FFF) or Fused Deposition Modeling (FDM) is one of the various types of AM material extrusion processes used extensively to print thermoplastics [7].

Figure 1.2 shows a schematic of the FFF process [8].In FFF, thermoplastics available as filament/wire stock are melted and deposited via heated nozzles layer-by-layer on a heated bed in pre-determined computer-generated deposition paths [9]. Due to low melting points, thermoplastics such as Polylactic Acid (PLA), Acrylonitrile Butadiene Styrene (ABS), Polyethylene Terephthalate (PET) , Polyamide-12 (PA), and Polyvinyl Alcohol (PVA) are some of the polymers commonly printed using FFF. However, the printing process introduces artifacts in the printed parts which affect their mechanical and failure characteristics and hence need to be investigated when parts are to meet critical functionality. In addition to this, prescribing the print path of the nozzle (or rastering) potentially introduces anisotropy in terms of weak planes in AM parts [10]. Hence, the role of print architecture on general mechanical failure and fracture properties needs to be studied carefully [11].

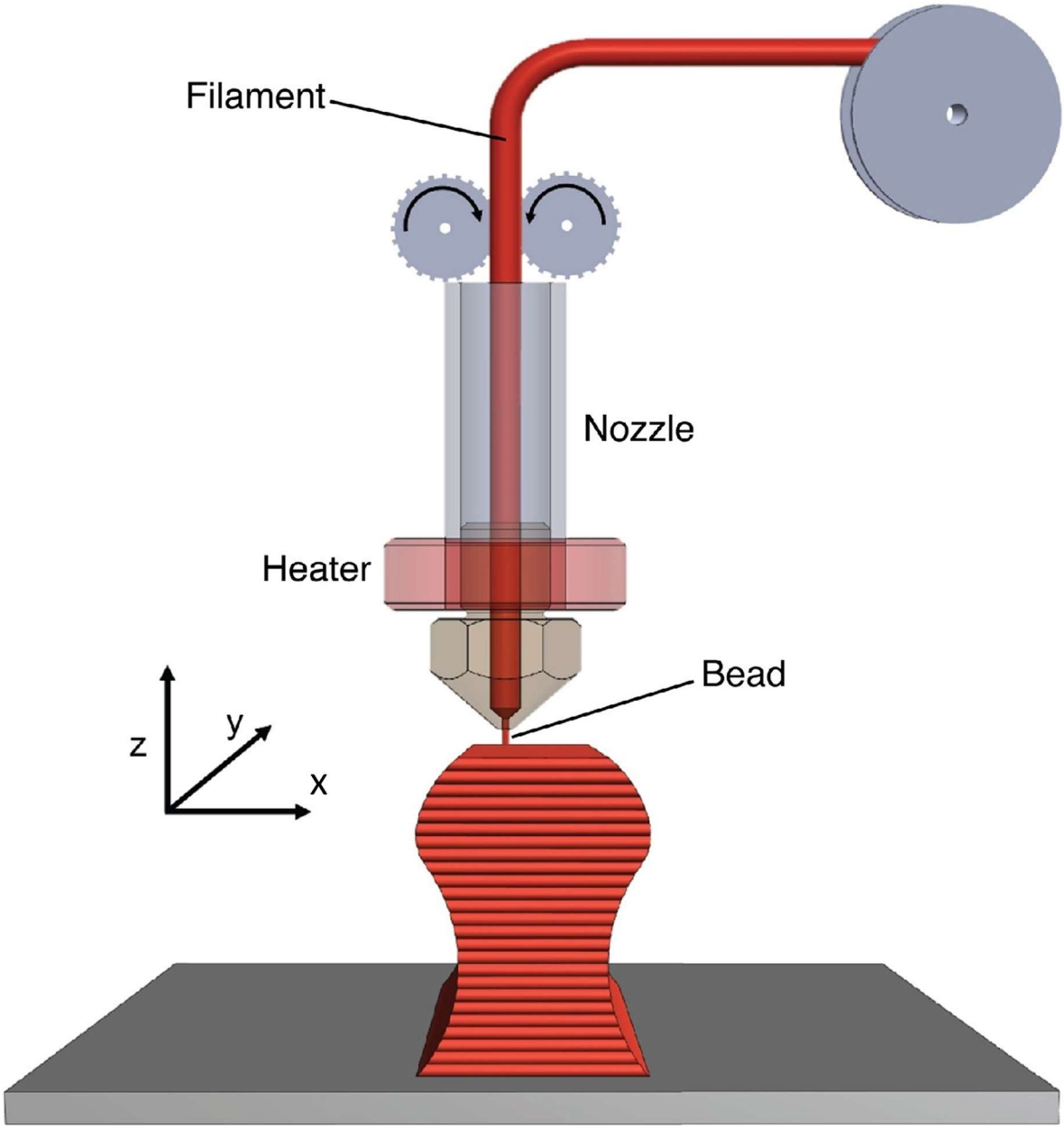

Figure 1.2: Schematic of Fused Filament Fabrication (FFF) process [8].

One of the popular amorphous thermoplastics used in FFF or FDM is Acrylonitrile Butadiene Styrene or ABS [12]. Various other thermoplastics, possessing different characteristics such as biocompatibility and/or compliance, are also used in disparate, sometimes unconventional applications such as dental and medical field (implants, prosthetics), furniture and fashion industry (shoes, watches), aviation and automotive field (fuel injection nozzle) [13, 14]. Since polymers

like ABS have found their way into all facets of daily life, it is important to understand the effects of the printing parameters and architectures before employing ABS parts produced by AM for everyday use.

Turning to the fracture mechanics aspects emphasized in this dissertation, three modes of fracture are identified in traditional fracture mechanics (Figure 1.3). They are identified as mode-I, mode-II, and mode-III fractures. The classification is based on the loading direction relative to the crack. When the crack flank experiences symmetric normal forces, the resulting fracture is called Mode-I or the crack opening mode (Figure 1.3(a)). When the crack flank experiences asymmetric in-plane shear forces, the resulting fracture is called mode-II or the crack sliding mode (Figure 1.3(b)). When the crack flank experiences out-of-plane shear forces, it results in mode-III or the crack tearing mode (Figure 1.3(c)). When a combination of forces is acting on the crack flanks, it is referred to as mixed-mode loading. When a crack is under the influence of normal and in-plane shear forces, it is often referred to as 2D in-plane mixed-mode loading. Often during the service of engineering parts, they not only experience normal loading but are also subjected to shear loading. In general, studying mixed-mode fracture behavior is challenging. The nature of the architectures formed by the deposition paths in FFF adds complexity to studying and understanding the mixed-mode fracture behavior of FFF parts. Hence, it is crucial to understand the mixed-mode fracture behavior of AM ABS in addition to the traditional Mode-I fracture behavior.

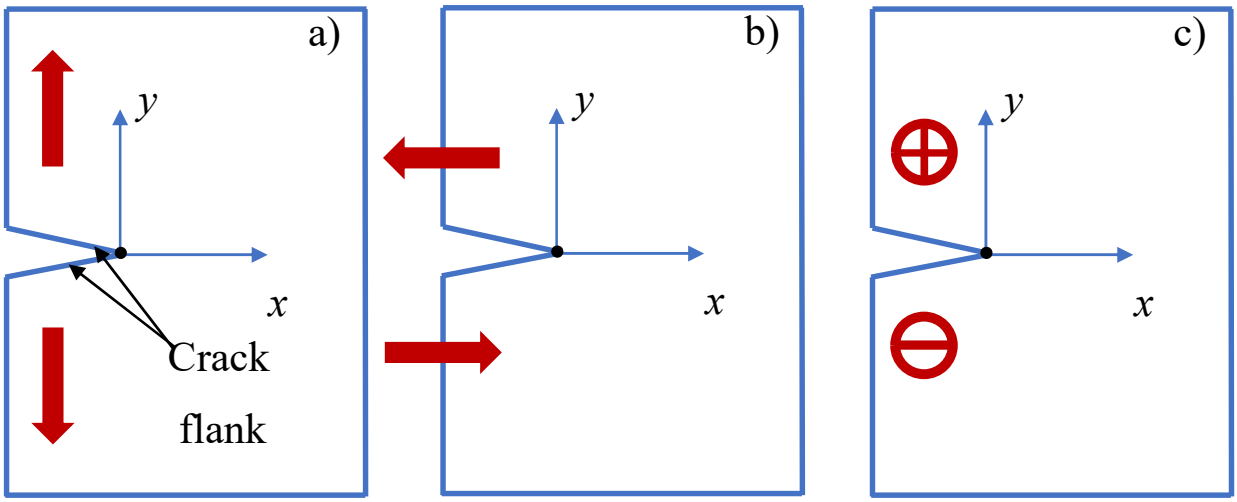

Figure 1.3: Different modes of fracture: (a) Mode-I, (b) Mode-II, and (c) Mode-III.

For studying and understanding fracture behavior at a fundamental level, implementing full-field visualization techniques become invaluable. Full-field visualization techniques provide ways to measure local mechanical quantities of interest such as displacements and strains. These measured quantities help us in extracting fracture parameters and enable us to fully appreciate the intricate local failure mechanisms at play. Understanding the need for such full-field measurements, all the fracture experiments in this work have been carried out with the aid of Digital Image Correlation (DIC).

1.2 Literature Review

In the following, background literature relevant to the current research is provided. Primarily, mechanical and fracture properties evaluation of AM ABS parts under quasi-static loading are reviewed. This is followed by the literature available on the high strain rate fracture studies of AM

ABS. Finally, research works reported on the mixed-mode fracture properties of AM ABS are presented.

The effects of build direction and raster orientation on mechanical failure were studied in [15] by performing tension tests. Three different build orientations (horizontal, side, and vertical) and four different raster orientations (±45°, 0°, 90°, and 0°/90°) were considered. The stress-strain curves from the tensile experiments are shown in Figure 1.4. Brittle failure was observed for the 0°, 90°, and 0°/90° raster orientations while the ±45° raster displayed softening before failure resulting in the greatest elongation-at-break value due to the effects of shear. Among the build orientations, horizontal and side build orientations had better responses than vertical build. The differences between the prints were explained using fractographic analyses to emphasize the significance of print architecture on mechanical strength. This study proved that the mechanical response of FFF ABS could be altered with the raster orientations/print architecture.

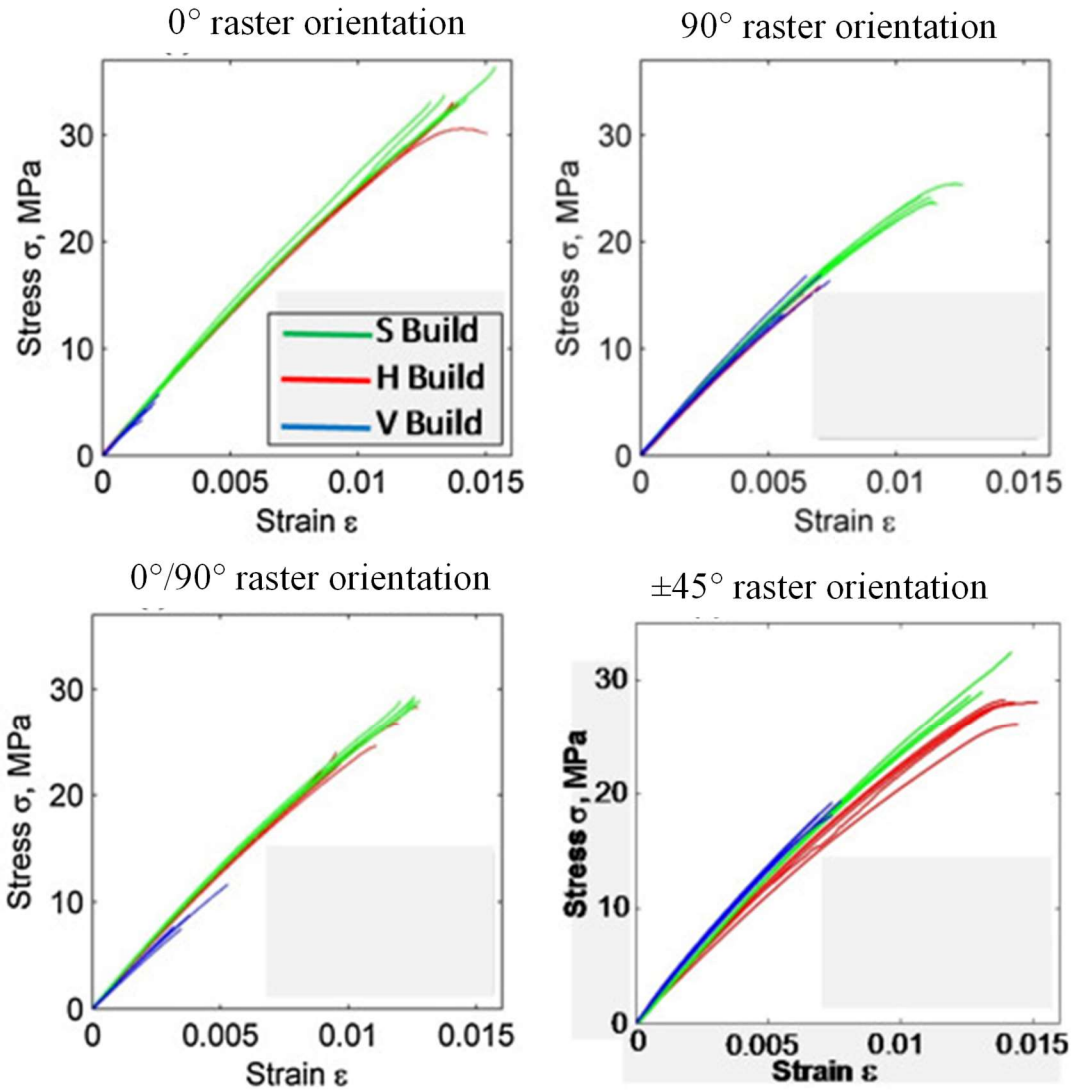

Figure 1.4: Tensile stress-strain curves for three different build orientations and four different raster orientations [15].

The size-dependent anisotropy in terms of flexural moduli and strain distributions in two unidirectionally printed ABS beams measured using DIC were reported in [16]. Some studies have focused on enhancing the fracture properties of printed parts by predefining nozzle paths based on the knowledge of stresses acting on the parts [17]. The fracture toughness was found to increase in additively printed ABS samples under mixed-mode loading when the deposition path was guided by the principal stress directions [18]. Some studies have also shown that the infill pattern

and the build direction with respect to the pre-crack affect the failure parameters [19-22]. Currently, woven multi-laminate composites are being additively manufactured and this has resulted in increased shear strength [23]. With ABS as the copolymer and thermoplastic polyurethane (TPU) as an additive, a polymer matrix was manufactured using the FFF process and was found to have enhanced adhesive (bonding strength) properties [24]. The presence of TPU increased the interlayer adhesion between the printed layers without compromising the yield strength for contents of TPU up to 20 weight percentages. In terms of fracture properties, layer orientation, build orientation, and infill percentages were found to be the main factors controlling the fracture toughness of AM parts produced through the FFF process [25-29]. Single-edge notched bend testing of FFF ABS was carried out for three build orientations (horizontal, vertical, and oblique) and their fracture properties were studied [28]. The fracture responses of this study are shown in Figure 1.5. Vertical build orientation was found to have a brittle response while the horizontal and the oblique builds had a ductile response along with approximately an order of magnitude higher energy absorption.

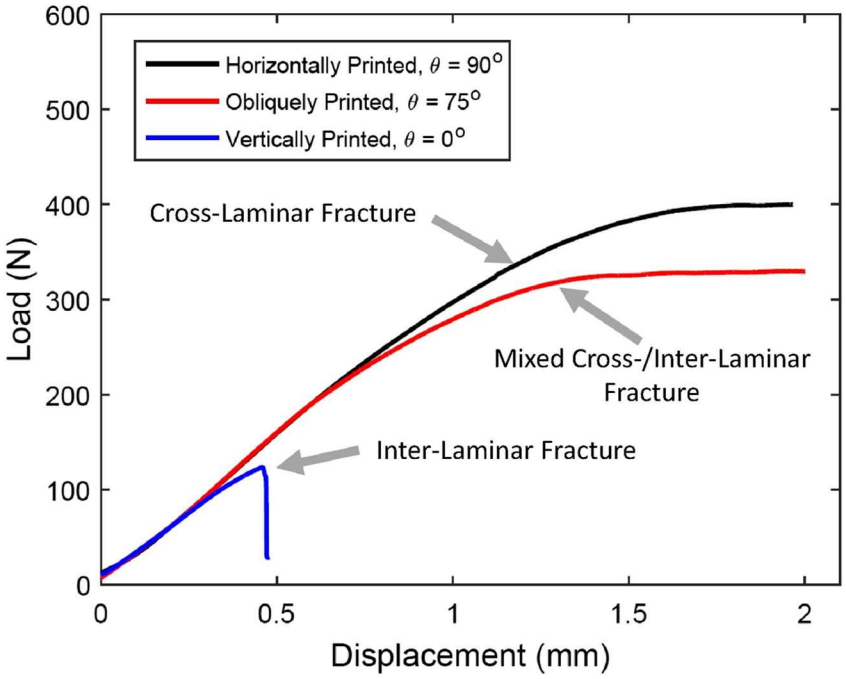

Figure 1.5: Fracture responses of single-edge notched specimens illustrating the effects of build orientation [28].

Since polymer-based AM parts are used extensively in day-to-day applications [4] with the potential of AM to produce critical load-bearing parts, it is important to study the differences in behaviors of these materials because of factors such as the layer architecture in detail. Although some previous works [21, 22, 25, 28] have reported on fracture behavior in terms of crack initiation, most have relied on far-field load or load-point displacement measurements. Some [16, 22] have utilized optical imaging during tests but quantitative local measurements have not been incorporated to study the crack growth behavior in detail. Thus, no work has been reported on both the crack initiation and growth behaviors based on local mechanical fields to reveal the intricacies of the fracture behavior of 3D-printed parts.

The effect of strain rate on the tensile strength of ABS manufactured via FFF was studied in [30-32] and increased moduli and tensile strengths were observed at higher loading rates. Tensile

results from [30] are shown in Figure 1.6. Figure 1.6(a) and Figure 1.6(b) show the increase in elastic modulus and tensile strength with the strain rate. It can also be observed that the filament with the smaller radii had better mechanical properties.

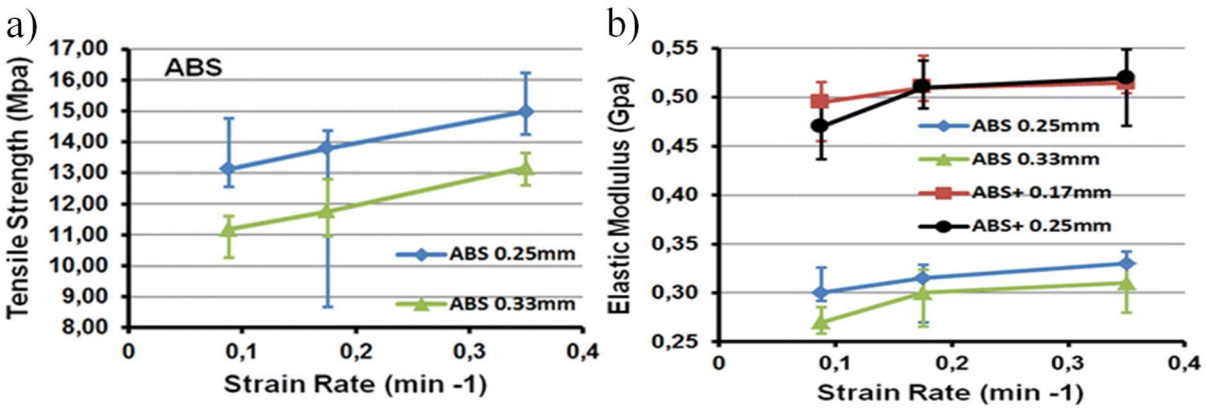

Figure 1.6: Effect of strain rate on FFF ABS. (a) and (b) shows the variation of tensile strength and elastic modulus under different strain rates for FFF ABS filaments of two different radii [30].

Dynamic shear and fracture behavior of bulk ABS under dynamic loading were studied in [33] and an increase in yield stress, shear modulus, and stress softening amplitude was observed. A few other works have studied strain-rate sensitivity of fracture properties of ABS AM parts under dynamic loading conditions, and variation in crack initiation toughness with respect to raster orientations was reported [26, 34]. The dynamic crack initiation was calculated to evaluate the effect of build orientations [26]. Two different build orientations (horizontal and vertical) and two raster orientations (0/90° and ±45°) were considered and their dynamic fracture initiation toughness values were calculated from strain gages mounted on the long bar in their modified-Hopkinson apparatus. The results are shown in Figure 1.7. In horizontal build, ±45° raster orientation had higher dynamic initiation toughness compared to the 0/90° orientation. The vertical build (0°) had better initiation toughness than the horizontal build. This study proved that the effect of build orientation and raster orientation was evident in the dynamic fracture properties as well.

With the knowledge that both bulk ABS and FFF ABS exhibit strain-rate dependencies, it is important to study the fracture behavior at elevated loading rates as well. Considering this, the high strain rate Mode-I fracture behavior was studied in this work with the help of a highspeed camera aiding in full-field visualization.

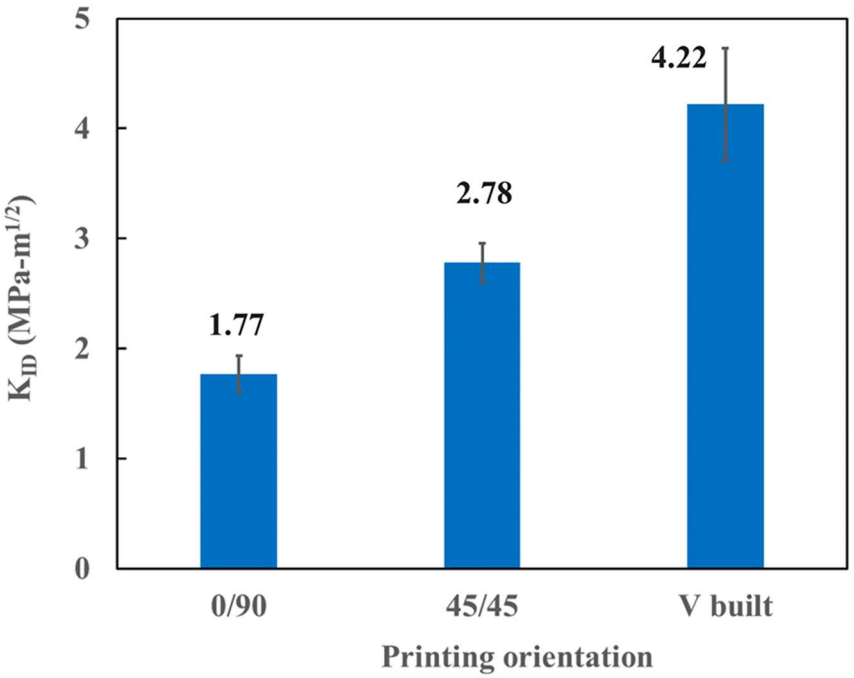

Figure 1.7: Effect of printing orientation on dynamic fracture initiation toughness [26].

Some studies have been carried out to explore the mixed-mode fracture properties in FFF polymers. The effect of layer orientation on the 2D mixed-mode fracture behavior was investigated for FFF polycarbonate specimens using a semi-circular beam (SCB) bending setup [35]. Fracture properties were obtained using the failure load data and the fracture envelope was plotted. It was found that the generalized maximum tangential stress (GMTS) criteria gave a better prediction than the maximum tangential stress (MTS) criteria for FDM polycarbonate. FFF ABS specimens with ±45° layers were subjected to SCB bending experiments to investigate the role of mode-mixity and rate of loading [36]. The specimens absorbed higher energies in the dynamic loading cases compared to the static counterparts in all mixities ranging from pure mode-I to pure mode-

II. Higher energy absorption was observed in mixed-mode and mode-II loading conditions than in mode-I conditions. Further fractographic results showed that zig-zag crack growth was minimized when the loading approached dominant mode-II and when tested under a high rate of loading. Additionally, there are a few works where mixed-mode fracture tests have been performed on AM polymers using a modified Arcan fixture [37]. Arcan loading fixtures have been widely used to perform Mode-I, Mode-II, and mixed-mode (I/II, I/III) fracture toughness tests. The Arcan apparatus was originally developed to produce a uniform state of plane stress in solid specimens, and they were primarily used for the biaxial testing of materials [38-40]. Mixed-mode fracture properties of FFF polylactic acid (PLA) with different infill percentages manufactured with ±45° architecture were evaluated using an Arcan loading fixture [41]. Critical SIFs were calculated from experimentally measured critical/failure loads and correctional factors from finite element analysis. The results showed that with an increase in infill, the fracture toughness increased at all mode-mixities. Also, as the mode-mixity increased from mode-I to mode-II, the fracture toughness increased for each of the infills. The mixed-mode fracture behavior of FFF ABS was studied with the help of the Arcan fixture to investigate the specimen thickness required to satisfy plane-strain conditions [42]. SIFs and energy release rate were calculated using finite element correction factors and it was concluded that a thickness of 10 mm was sufficient to achieve plane-strain condition. Mixed-mode fracture properties of FFF ABS for different infill patterns (line, hexagon, triangle, and 3D infill) at 70% infill were studied using a modified Arcan setup [43]. Line infill pattern was found to have higher initiation toughness at all the different loading angles than its counterparts owing to the lower density of polygonal elements in other infill patterns. No work has been performed to directly compute the mode-I and mode-II SIFs based on the local mechanical fields. Global measurements combined with finite element analysis have been the norm for

calculating fracture properties until now. Considering the complex nature of the rastering of layers and the anisotropy in terms of the fracture plane in FFF ABS, it is important to explore the extraction of fracture parameters from local measurements.

To emphasize the importance of local measurements obtained from full-field visualization techniques, the following literature on the mechanical characterization of other AM materials studied using DIC has been reviewed. The measurement and determination of the mechanical properties of large-scale additively manufactured (BAAM-Big Area Additive Manufacturing) polymer test coupons were enhanced by incorporating DIC into tensile experiments [44]. With AM techniques like BAAM [45, 46], where the bead sizes can be in the order of multiple millimeters, standard test coupons fail to capture the unique and necessary information about the bonding between beads/layers. In such cases, DIC becomes a key component to measure mechanical properties. In the above work, elastic modulus, Poisson's ratio, and stress-strain curves were successfully calculated from the DIC data. Further, post-fracture fractographic analysis agreed well with the propagation behaviors obtained from imaging via DIC. DIC strain fields obtained prior to fracture are shown in Figure 1.8. The effect of build orientation and raster orientation on the fracture behavior of AM carbon fiber reinforced polymer was examined with the help of DIC [47]. Fracture experiments were carried out on compact-tension specimens. The results of force-displacement curves and the crack opening strain fields for one build orientation are shown in Figure 1.9. The full-field visualization technique of DIC was successfully implemented to elucidate the experimentally observed fracture trends.

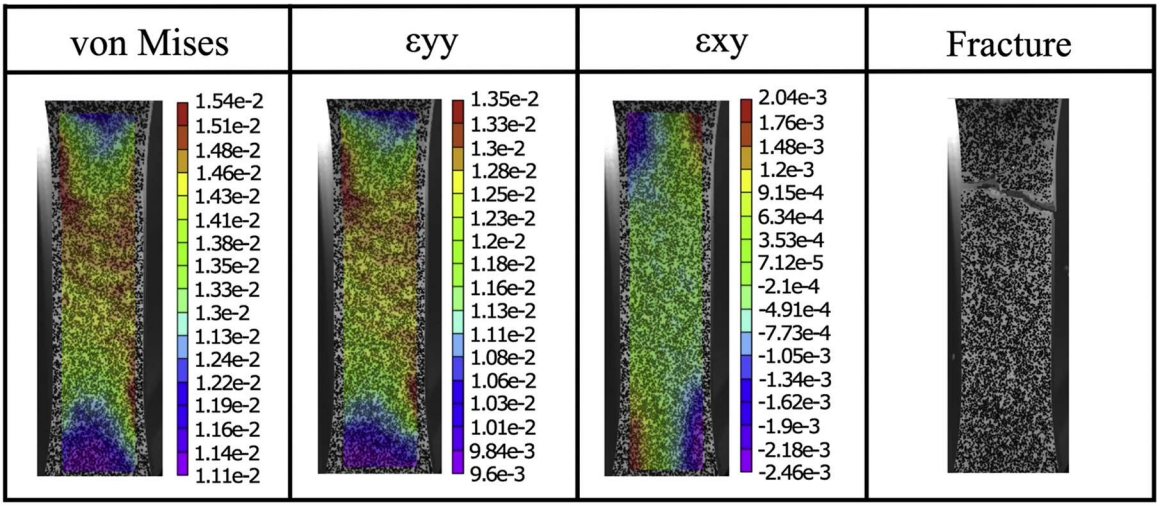

Figure 1.8: DIC strain fields at an instant before fracture [44].

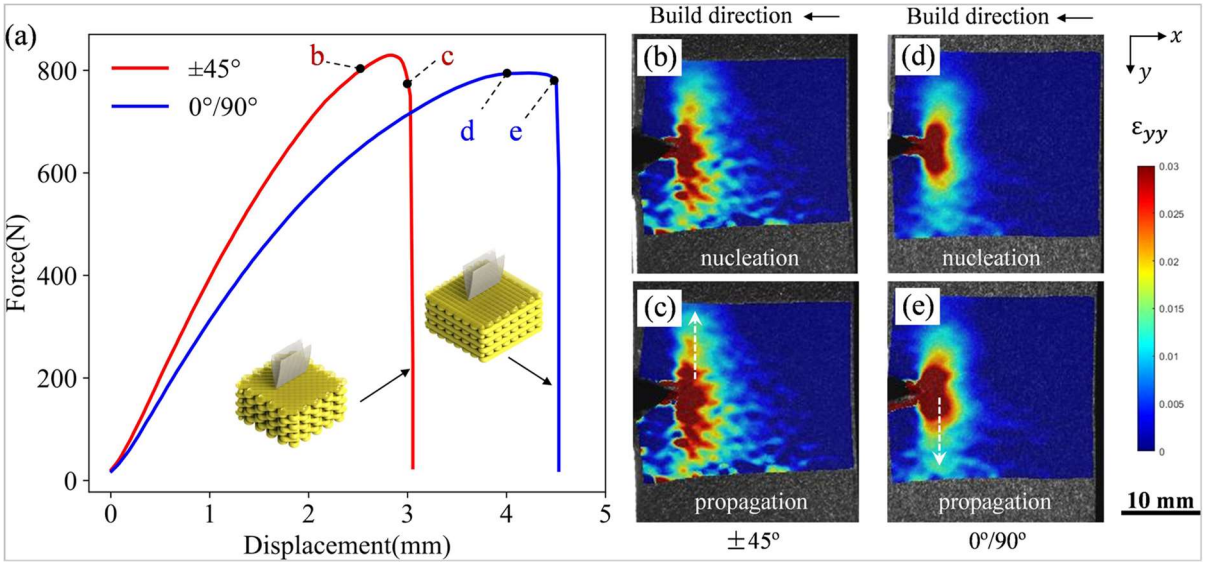

Figure 1.9: (a) Globally measured force-displacement curves, (b)-(e) Crack opening strain fields from DIC at the crack nucleation and propagation phases for the two raster orientations studied in this work [47].

1.3 Research objectives

The literature review indicates that full-field visualization techniques have not been incorporated into investigating the complete fracture behavior of AM ABS including crack initiation and propagation. The effect of print architecture or raster orientations is something that has the potential to alter the nature of mechanical and fracture response. Considering the strain rate dependence of ABS, the mechanical and fracture properties under high strain rates must be examined as well. Thus, it is hypothesized here that a tensile and fracture mechanics study on AM ABS that incorporates full-field visualization methods can better reveal the effects of print architecture and strain rate. Hence, the objective of this dissertation is to formulate an opto-mechanical approach coupled with fractography to investigate the role of print architecture and strain rate on the failure mechanics of additively printed ABS. The specific tasks for achieving the above objective are as follows:

- Develop a robust hybrid DIC-FE approach to evaluate fracture parameters,
- Perform tensile and mode-I fracture experiments under quasi-static loading conditions aided by DIC,
- Perform high strain rate mode-I fracture experiments with a modified-Hopkinson pressure bar setup and implement DIC with the aid of a high-speed camera,
- Develop an Arcan loading fixture capable of testing AM ABS in 2D mixed-mode loading conditions,
- Perform quasi-static fracture experiments with the Arcan loading fixture coupled with DIC with different mode-mixities ranging from pure mode-I to pure mode-II,
- Perform fractography to obtain the crack paths and fractured cross-sections of tensile and fracture specimens,

- Link macro measurements and micro-scale observations to understand the effects of print architecture on pure and mixed-mode fracture behaviors.

1.4 Organization of the dissertation

This dissertation is organized into six chapters including the Introduction. In Chapter 2, information about DIC and the implemented hybrid DIC-FE methodology is explained in detail. Chapter 3 contains the experimental details and results from uniaxial tension experiments and quasi-static fracture experiments. Details on ultrasonic measurements and high strain rate fracture experiments are provided in Chapter 4 along with the discussion of results. Chapter 5 comprises the mixed-mode (I/II) fracture experiments, information on the Arcan apparatus, and a discussion of fracture behavior under different mode-mixities. Finally, the major conclusions of this dissertation and potential future topics are recorded in Chapter 6.

Chapter 2. Hybrid DIC-FE Approach

In this chapter, Information about the optical method DIC and the hybrid DIC-FE approach developed in this research are provided. The working principles of DIC and its execution are detailed first. This is followed by the concerns involved in implementing traditional fracture parameter extraction calculations for AM polymers. Then, the development of the hybrid DIC-FE methodology and its advantages are described.

2.1 Digital Image Correlation

Digital Image Correlation is a popular full-field optical metrology technique commonly used for non-contact, vision-based strain analysis and is widely used to measure surface deformations[48]. In this work, the 2D-DIC method was used to measure two orthogonal in-plane displacement components on the specimen surface in the vicinity of a growing crack[49-51].

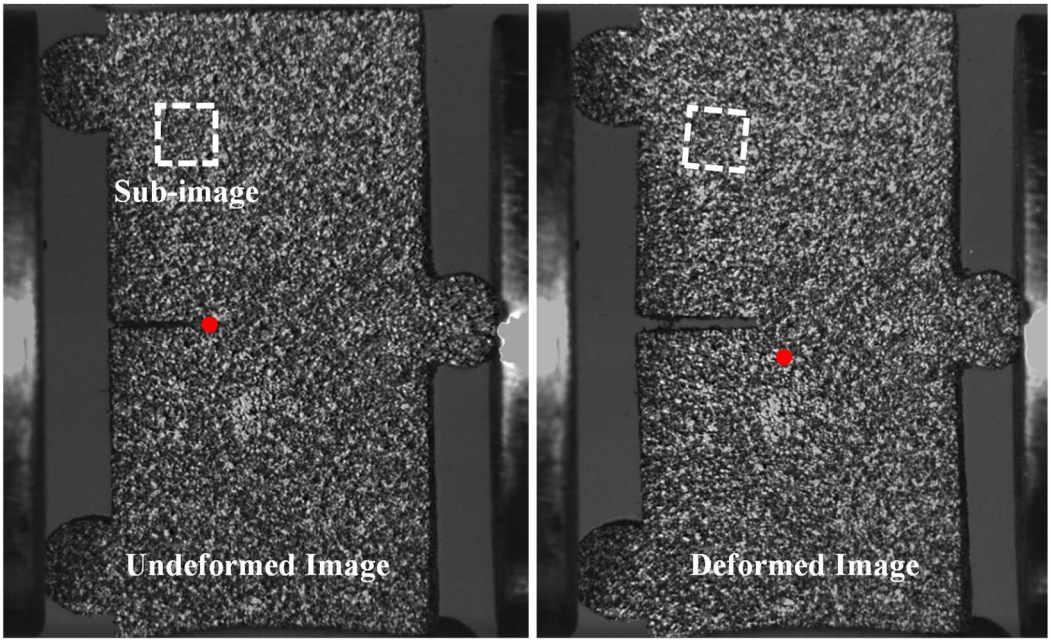

Figure 2.1: Speckle images recorded by the camera in undeformed and deformed states.

The working principle of 2D-DIC is as follows: A random coat of black and white speckle pattern is applied to a surface of the specimen and this surface is imaged using a digital camera before and during deformation. Images recorded during different stages of deformation are collected along with an image before deformation and are spatially correlated. During the correlation step, the undeformed (before loading) and the deformed (during/after loading) images are divided into a specific number of sub-images (made of pixel arrays). Now, each sub-image in the undeformed state is selected and its corresponding sub-image in the deformed states is located by precisely matching the grayscale values of the undeformed and deformed sub-images. Once the deformed sub-image is located, the distance moved by this particular sub-image with respect to the undeformed image can be calculated. Thus, the in-plane displacement over the whole specimen surface can be quantified by repeating the sub-image location process for all the sub-images in the undeformed state. To locate and match the sub-images based on grayscale values, a correlation coefficient is generally used. The correlation in this work was performed using the ARAMIS® image analysis software (v6.2.0). ARAMIS® does not share the details of its exact correlation function because of proprietary reasons and hence, a commonly used correlation function is explained below[51, 52]:

Figure 2.2 shows a schematic of undeformed and deformed sub-images and the notations involved in the correlation function. An iterative approach is employed to get the best match of sub-images from the undeformed and deformed states. This is achieved by minimizing the 2D cross-correlation coefficient C by using a nonlinear optimization techbnique. The cross-correlation coefficient C is defined as,

$$C\left(u, v, \frac{\partial u}{\partial x}, \frac{\partial u}{\partial y}, \frac{\partial v}{\partial x}, \frac{\partial v}{\partial y}\right) = 1 - \frac{\sum_{i,j}\left[F(x_i, y_j) - \bar{F}\right]\left[G(x_i^*, y_j^*) - \bar{G}\right]}{\sqrt{\sum_{i,j}[(F(x_i, y_j) - \bar{F})^2]\ \sum_{i,j}[(\,G(x_i^*, y_j^*) - \bar{G})^2]}} \tag{2.1}$$

In the above equation, $F(x_i, y_j)$ is the pixel intensity or the grayscale value at a point (x_i, y_j) in the undeformed image and $G(x_i^*, y_j^*)$ is the gray scale value at a point (x_i^*, y_j^*) in the deformed image. $\bar{F}$ and $\bar{G}$ denote the mean values of the intensity matrices *F* and *G*. The points (x_i, y_j) and (x_i^*, y_j^*) are related by the in-plane deformation that occurs between the two images. Provided that the deformation is in a plane perpendicular to the optical axis of the camera, the relation between (x_i, y_j) and (x_i^*, y_j^*) can be approximated by a 2D affine transformation,

$$x^* = x + u + \frac{\partial u}{\partial x}\Delta x + \frac{\partial u}{\partial y}\Delta y$$
$$y^* = y + v + \frac{\partial v}{\partial x}\Delta x + \frac{\partial v}{\partial y}\Delta y \qquad (2.2)$$

Here, u and v are local translations of the center of the deformed sub-image in the *X* and *Y* directions, respectively. The distances from the center of the sub-image to a generic point (x, y) are denoted by Δx and Δy. Thus, the correlation coefficient C, which is a function of displacements and displacement gradients, is minimized by searching for the optimum values of displacements and their gradients by using algorithms such as the Newton-Raphson method.

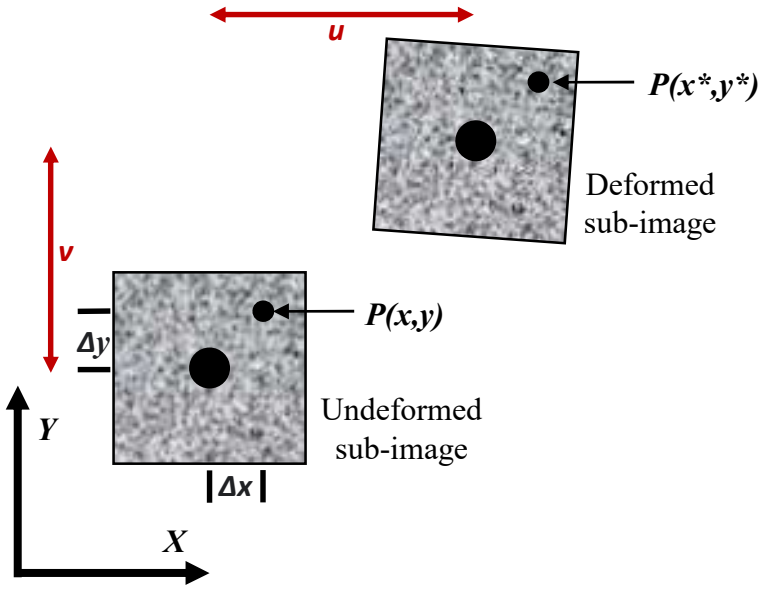

Figure 2.2: Sub-images location in DIC.

In this work, the optical technique of 2D-DIC was implemented in the tensile and fracture experiments under quasi-static loading conditions to measure the orthogonal in-plane displacements over the specimen surface using a slow-rate digital camera. A high-speed camera was used in recording speckle patterns on the specimen surface during high strain rate fracture experiments as well. DIC parameters for each set of experiments are provided along with the results section.

2.2 Extraction of fracture parameters

2.2.1 Conventional methodology

In many previous studies on traditional structural materials, the measured displacements obtained from DIC are used in conjunction with the theoretical asymptotic expressions and over-deterministic least-squares analyses to determine the crack tip fracture parameters such as Stress Intensity Factors (SIFs)[49-51, 53-56]. The procedure to obtain SIFs along with the theoretical

equations for crack tip displacements is discussed next. The orthogonal in-plane displacements measured from DIC are combined with both crack opening and crack sliding displacements fields to extract the required SIFs. The theoretical asymptotic expressions for displacements fields for a stationary crack are given by [57],

$$u(r,\theta) = \sum_{n=1}^{\infty} \frac{(K_I)_n}{2\mu} \frac{r^{n/2}}{\sqrt{2\pi}} \left\{ \kappa \cos\frac{n}{2}\theta - \frac{n}{2}\cos\left(\frac{n}{2}-2\right)\theta + \left\{\frac{n}{2} + (-1)^n\right\}\cos\frac{n}{2}\theta \right\} + \sum_{n=1}^{\infty} \frac{(K_{II})_n}{2\mu} \frac{r^{n/2}}{\sqrt{2\pi}} \left\{ \kappa \sin\frac{n}{2}\theta - \frac{n}{2}\sin\left(\frac{n}{2}-2\right)\theta + \left\{\frac{n}{2} - (-1)^n\right\}\sin\frac{n}{2}\theta \right\}, \tag{2.3}$$

$$v(r,\theta) = \sum_{n=1}^{\infty} \frac{(K_I)_n}{2\mu} \frac{r^{n/2}}{\sqrt{2\pi}} \left\{ \kappa \sin\frac{n}{2}\theta + \frac{n}{2}\sin\left(\frac{n}{2}-2\right)\theta - \left\{\frac{n}{2} + (-1)^n\right\}\sin\frac{n}{2}\theta \right\} + \sum_{n=1}^{\infty} \frac{(K_{II})_n}{2\mu} \frac{r^{n/2}}{\sqrt{2\pi}} \left\{ -\kappa \cos\frac{n}{2}\theta - \frac{n}{2}\cos\left(\frac{n}{2}-2\right)\theta + \left\{\frac{n}{2} - (-1)^n\right\}\cos\frac{n}{2}\theta \right\}. \tag{2.4}$$

In the above equations, $u(r,\theta)$ and $v(r,\theta)$ are crack opening and crack sliding displacements, (r,θ) are crack tip polar coordinates, κ is $(3-v)/(1+v)$ for plane stress conditions, and μ and v are shear modulus and Poisson's ratio. The coefficients $(K_I)_n$ and $(K_{II})_n$ of the leading terms $(n=1)$ are the mode-I and mode-II SIFs. For mode-I problems, K_I can be extracted from $u(r,\theta)$ equations as they are the dominant in-plane displacement. However, when it's a mixed-mode problem, radial $(r(r,\theta))$ and/or tangential $(\theta(r,\theta))$ displacement fields are used to accurately extract $K_I$and K_{II} [58]. The radial and tangential displacement fields can be computed by transforming the $u(r,\theta)$ and $v(r,\theta)$ displacement fields as per the following equation,

$$\begin{pmatrix} r(r,\theta) \\ \theta(r,\theta) \end{pmatrix} = \begin{pmatrix} \cos\theta & \sin\theta \\ -\sin\theta & \cos\theta \end{pmatrix} \begin{pmatrix} u(r,\theta) \\ v(r,\theta) \end{pmatrix} \tag{2.5}$$

For extracting the SIFs from displacement data, the crack tip location must be known. Displacement data in the region around the crack tip were collected within the limits of $(0.3 < \frac{r}{B} < 1.6)$ and $(-120° < \theta < 120°)$ where B is the specimen thickness. The collected displacement data coupled with the theoretical displacement field equations are employed to carry out an over-deterministic least square analysis [59] for extracting $K_I$and K_{II}. In this work, the computation of SIFs was attempted using the radial displacement field equations.

2.2.2 Limitations of employing displacement fields

The measured fracture parameters are generally sensitive to the number of terms of the asymptotic displacement field employed, the rigid body motions/rotations suffered by the specimen during deformation, the domain over which the data is extracted, out-of-plane displacements due to crack tip triaxiality, etc. The results often are sensitive to the location of the crack tip in the speckle image and/or the displacement field. To emphasize the shortcomings in implementing this approach for AM polymers, a speckle image and its corresponding displacement contours from an AM ABS specimen during crack growth are shown in Figure 2.3 as an example. It can be seen that the precise identification of the crack tip is not possible because of the jagged crack front and inelastic deformations around the crack tip from the enlarged speckle image shown. Identification of the crack tip can only be narrowed down to a small region. To quantify the errors associated with SIFs because of incorrect crack tip selection, the best crack tip location was chosen via visual inspection of speckle images and displacement contours for a mode-I fracture experiment of AM ABS specimen before crack initiation. A set of four different crack tip locations were chosen subsequently around the apparent crack tip based on the best guess. These five crack tip locations were supplied as input for the least-squares analyses and the resulting mode-I SIF, K_I, is shown in Figure 2.3. The average error due to the different crack tip locations was ~15%

when compared to the theoretical closed-form solution (Eq. 3.1) based on LEFM. To highlight the variance in SIFs from the domain/region over which the data is extracted for the least-square analysis, Figure 2.4 shows the resulting K_I values for three different regions along with the theoretical values. The three regions chosen are shown in Figure 2.4, where r is the radial distance from the crack tip and B is the specimen thickness. The average error over the data extraction domains is ~20%. In traditional materials such as epoxies and acrylic, the identification of crack tip is relatively simpler due to the lack of inelastic deformations around the crack tip and the absence of texture on the specimen surface. However, the AM architectures create a considerable challenge for identifying precise crack tip location and data collection domain. The errors caused by such uncertainties are significant and cannot be overlooked. Hence, there was a need for a newer approach to extract fracture properties.

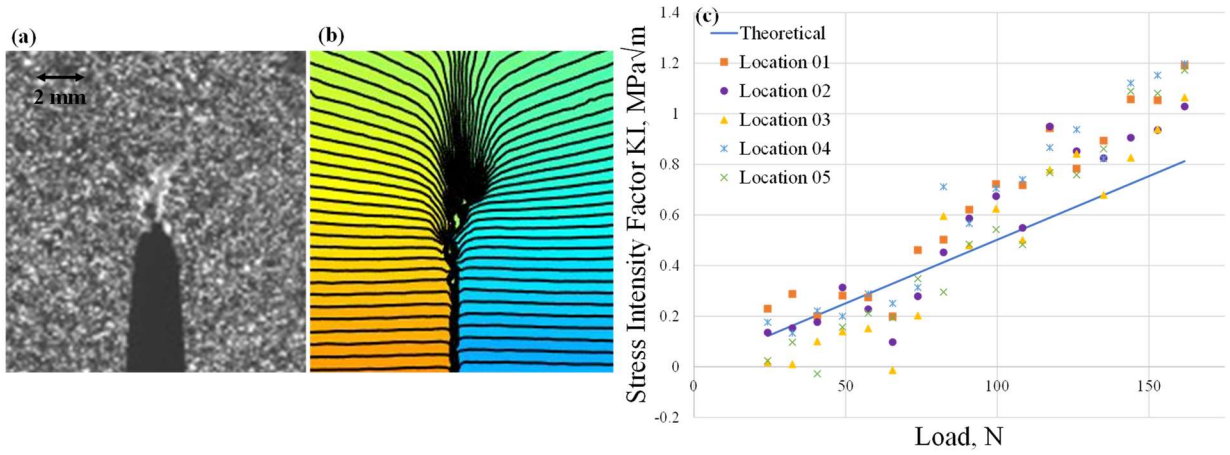

Figure 2.3: Uncertainty of crack tip location on extracted fracture parameters: (a) Speckle images and (b) displacement contours recorded for AM ABS specimen during crack growth. (c) SIFs extracted for different crack tip locations.

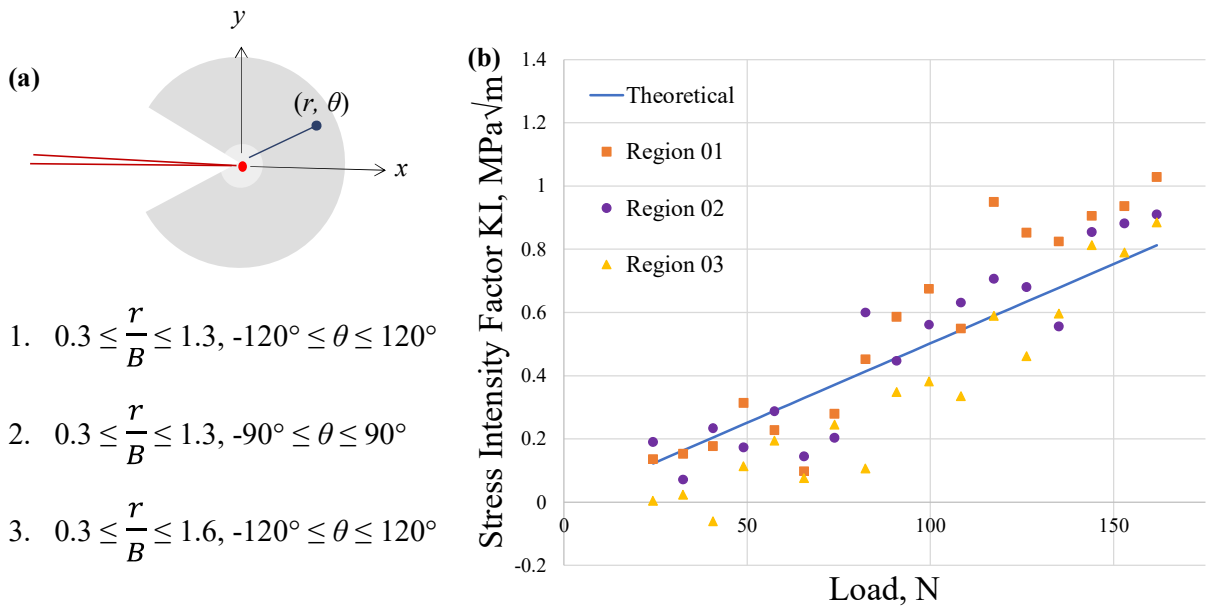

Figure 2.4: Effects of data extraction domains on estimated fracture parameters: (a) Domains/regions over which SIF was utilized, and (b) SIFs extracted for different regions.

2.2.3 Hybrid DIC-FE Approach

In LEFM, the energy release rate is defined as the rate at which the stored energy is transformed into surface energy as the crack extends. The definition includes plastic and kinetic energy transformations when material nonlinearity and dynamic fracture events are involved. The energy release rate can be evaluated using a path-independent integral known as the *J*-integral. The path independence of the quantity of interest mitigates some of the concerns involved with fracture parameters evaluation using the least-squares error minimization analyses.

The 2D-DIC method gives us in-plane displacements over the whole specimen surface. The displacements can be numerically differentiated to find the strain fields and other deformation gradients. The numerically obtained derivatives from DIC are often noisy, particularly when deformations are small. Figure 2.5 and Figure 2.6 shows experimentally measured displacement and resulting normal strain fields from DIC for a typical quasi-static fracture and high strain rate

fracture experiment on AM ABS, respectively. As can be observed, the strain fields (Figure 2.5(b) and Figure 2.6(b)) obtained from displacements via differentiation are very noisy when compared to the noise level in the displacement component fields (Figure 2.5(a) and Figure 2.6(a)) . The strain components from DIC prove themselves to be useful in highlighting the nature of strains and their magnitude from a global perspective. However, to perform local qualitative analysis along a certain path/location, as is the case in finding the *J*-integral, the strain data does not offer much help. Considering these, a simpler method of transferring the two measured orthogonal displacement data arrays from DIC into a 2D finite element model as surface (boundary) input to compute the energy release rate is considered.

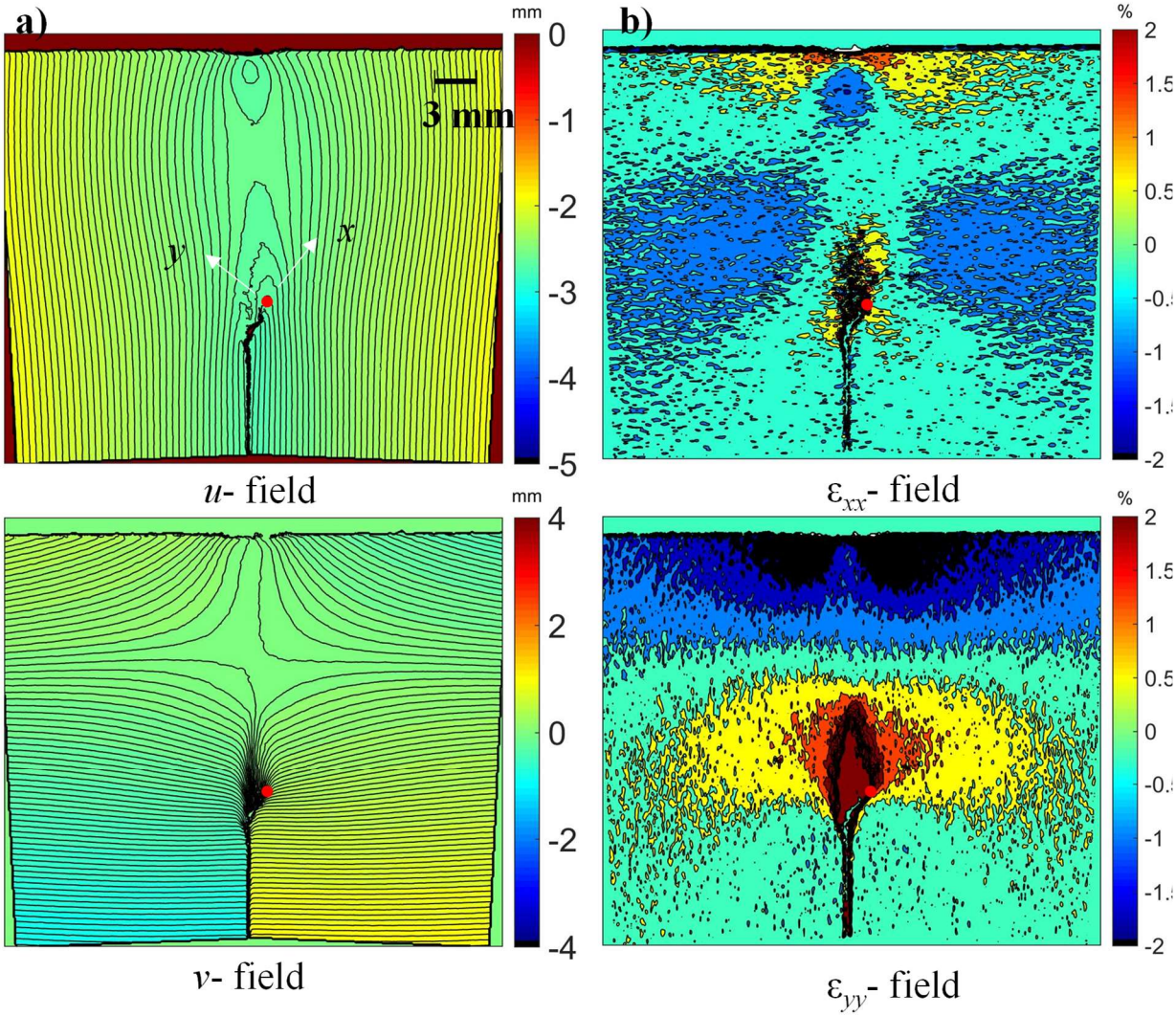

Figure 2.5: Two orthogonal displacement fields from quasi-static fracture experiment, *u* and *v* in the *x* and *y*-directions (a) and the corresponding normal strain fields (b) from DIC at a time instant/load step (load = 1082 N). A higher noise level in the strain field relative to the displacement fields is evident. (The displacement contour increment in (a) is 50 μm.)

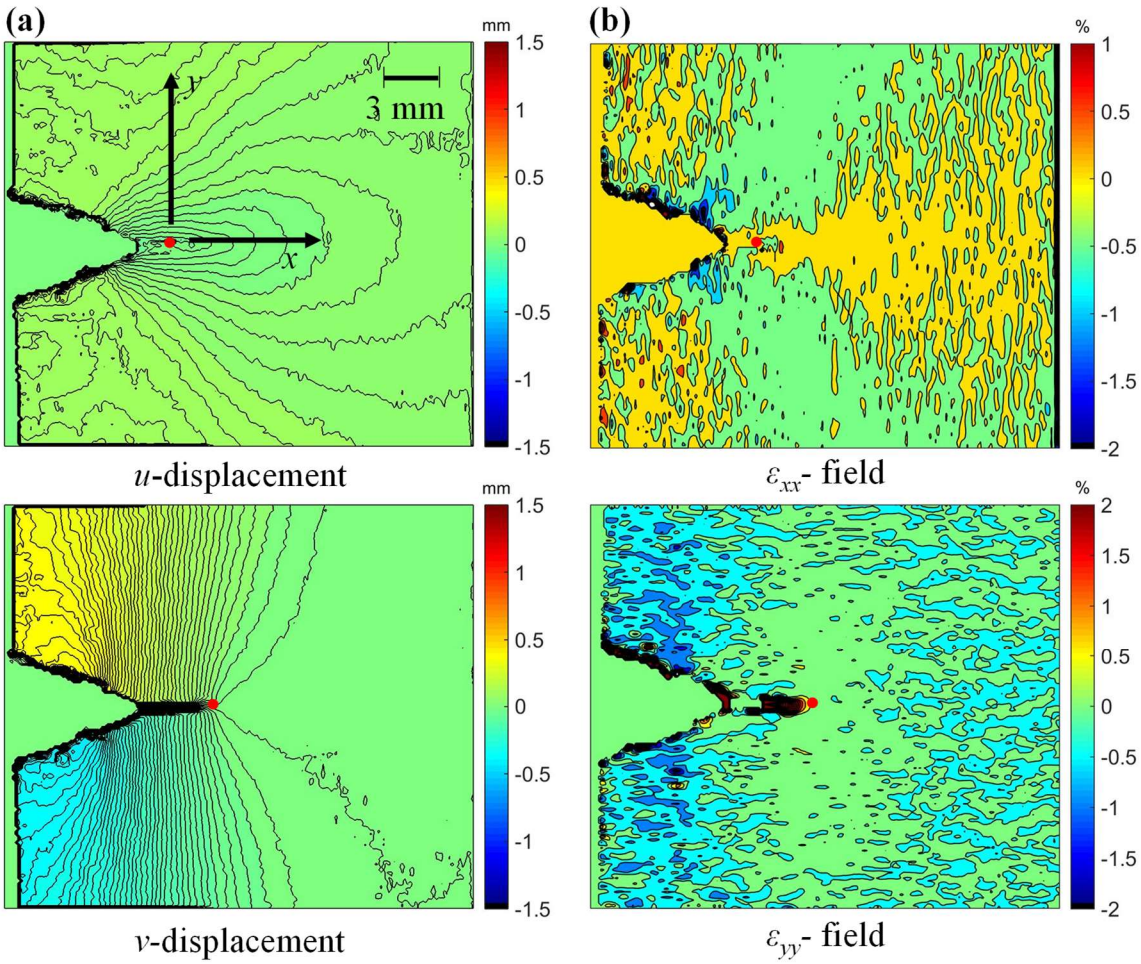

Figure 2.6: Two orthogonal displacement fields from high strain rate fracture experiment, u and v in the x- and y-directions (a) and the corresponding normal strain fields (b) from DIC at a time instant/load step.

The deformation gradients needed to calculate fracture parameters namely the path-independent J-integral[60, 61] can be expressed as,

$$J = \lim_{\Gamma \to 0} \int_{\Gamma} \left(W\delta_{1i} - \sigma_{ij} \frac{\partial u_j}{\partial x_1} \right) n_i dC, \ (\mathrm{i,j} = 1,2; x_1 = \mathrm{x}, x_2 = y) \tag{2.6}$$

In the above, W is the strain energy density ($= \frac{1}{2}\sigma_{ij}\varepsilon_{ij}$), σ_{ij} and u_j are the Cartesian components of the stress ($\sigma_{11} = \sigma_{xx}, \sigma_{12} = \sigma_{xy}$, etc.) and displacements ($u_1 = u, u_2 = v$), n_i are components of the unit vector normal to the counterclockwise contour path Γ, δ_{1i} is the Kronecker delta and dC is the arc length along the contour. Being a path independent quantity, the J-integral is often

evaluated as a line integral. But it can also be expressed as area or surface integrals. The *J*-integral for computing the energy release rate using *domain (area) integral* is defined as,

$$J = \int_A \left(-W\delta_{1i} + \sigma_{ij} \frac{\partial u_j}{\partial x_1} \right) \frac{\partial q_1}{\partial x_1} dA, \ (\mathrm{i,j} = 1,2) \tag{2.7}$$

In the above equation, A is the area of the domain/ribbon of elements encircling the crack tip, q_1 is a sufficiently smooth weighting function, and all other parameters are as defined previously. Furthermore, this approach allows the decomposition of the computed *J*-integral subsequently into individual stress intensity factors (K_I and K_{II}) using mode-partitioning based assumed pure mode auxiliary fields[62, 63] with known stress intensity factors and invoking small-scale yielding. This allows additional insight into the fracture modes at play in 3D-printed architectures. Accordingly, this new approach was adopted in this work.

In DIC, the recorded images in the reference and deformed states are segmented into subsets/sub-images of gray scales. Subsequently, the displaced location of a subset in the deformed state is determined relative to its undeformed state using a grayscale correlation algorithm. In doing so, each displacement data point in the full field is an average value computed over the corresponding subset *at its center*. To implement the proposed approach, careful meshing was carried out in such a way that these displacement locations match the nodal locations in the finite element model consisting of a square grid of quad elements parallel and perpendicular to the specimen edges. It should be noted, however, that when the crack followed a kinked path relative to its initial orientation, the neighborhood of the crack (region adjacent to the flanks) was discretized along a band using quad elements, and the nodes were inputted with *interpolated* displacement boundary conditions from DIC subsets. When there was an increase in length or change in direction, FE models were updated with the new crack tip location; the new crack orientation was identified relative to the previous step. It should also be noted that the crack tip

was modeled simply as a sharp discontinuity since the *measured* displacements were used as 'input' to the FE model to *dictate* the post-processing of DIC data to find the *J*-integral and then SIFs via mode-partitioning approach. Hence, it should be noted that the sharpness of the crack tip in the model is unimportant; it is only the location and the orientation that matters.

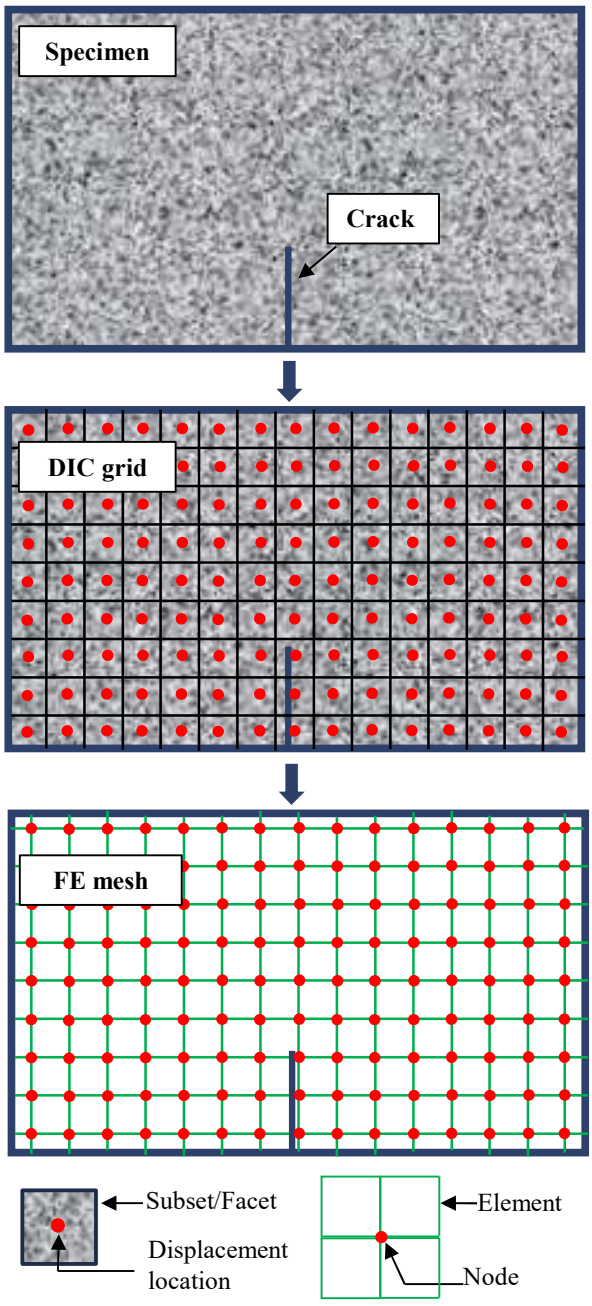

Figure 2.7: The approach to computing the *J*-integral and SIFs by transferring DIC data into FE discretization for domain integration and mode-partitioning. The red dots are the center of the sub-image and nodes of the FE grid.

A schematic of the steps followed in this approach is shown in Figure 2.7. Experimentally measured displacement components from DIC were then imported as nodal 'boundary conditions' for the discretized field. The FE model was then run using ABAQUS structural analysis software (v.16.1) after identifying the current crack tip position and its orientation to evaluate the fracture parameters using in-built algorithms. Using the computed *J*-integral, the two stress intensity factors (SIFs) K_I and K_{II} were calculated via the interaction integral method [63] and small-scale yielding assumption. The mode partitioning of the *J*-integral is based on the following approach. For a linear elastic solid, $J = \left(\frac{1}{8\pi}\right)[K^T B^{-1} K]$ where, B is the so-called pre-logarithmic energy factor matrix [63-66] and $K = [K_I, K_{II}]^T$. For a homogeneous, isotropic material and plane stress conditions, $J = \frac{1}{E}({K_I}^2 + K_{II}^2)$ where, K_I and K_{II} are pure mode-I and mode-II SIFs. K_I and K_{II} are calculated from the computed *J* -integral using the interaction integral method:

$$J = \frac{1}{8\pi}[K_I B_{11}^{-1} K_I + 2K_I B_{12}^{-1} K_{II}] \tag{2.8}$$

For an auxiliary pure mode-I stress field with SIF k_I, the *J*-integral is:

$$J_{aux}^{I} = \frac{1}{8\pi} k_I B_{11}^{-1} k_I \tag{2.9}$$

Superimposing the auxiliary field onto the actual field yields,

$$J_{tot}^{I} = \frac{1}{8\pi}[(K_I + k_I) B_{11}^{-1} (K_I + k_I) + 2(K_I + k_I) B_{12}^{-1} K_{II}] \tag{2.10}$$

Therefore, the interaction integral is,

$$J_{int}^{I} = J_{tot}^{I} - J - J_{aux}^{I} = \frac{k_I}{4\pi}\,(B_{11}^{-1}\,K_I + B_{12}^{-1}\,K_{II}) \tag{2.11}$$

Repeating the calculations for mode-II, we can arrive at

$$J_{int}^{II} = J_{tot}^{II} - J - J_{aux}^{II} = \frac{k_{II}}{4\pi}\,(B_{21}^{-1}\,K_I + B_{22}^{-1}\,K_{II}) \tag{2.12}$$

where the auxiliary pure mode-II stress field with SIF k_{II} is superposed onto the actual field. By solving the above two equations by assigning unit values for the auxiliary SIFs, individual SIFs K_I and K_{II} can be computed.

The fracture parameters are reported by ABAQUS for different contours. The first contour corresponds to the ring of elements encircling and embracing the crack tip and the second includes the first and the second rings, and so on. That is, as the contour number increases, the radial extent of the domain around the crack tip used for computing the *J*-integral increases. Since, the discretization corresponds to the sub-image overlap used while performing DIC (sub-image size = 25×25 pixels and step size = 5 pixels, scale factor (optical magnification) ~ 0.030 mm/pixel), each additional ring corresponds to the radial increment equal to the sub-image overlap × the scale factor. Figure 2.8 shows two examples of such plots of the *J*-integral and the corresponding K_I and K_{II} values in terms of the contour numbers at crack initiation for the A1 and A2 architectures. Evidently, the values do not show path independence in the very close vicinity of the crack tip (up to contour #7 or ~1 mm) due to a combination of out-of-plane displacements due to triaxial effects, inelastic deformations violating small-scale yielding assumptions, and the finite element size and shape functions, among others. However, at larger distances of 2.25-7 mm (*r/B* ratio ~ 0.4-1.2, where *r* is the radial distance from the crack tip and *B* is the specimen thickness) away from the crack tip, the values are rather stable and nearly constant with ~4% variation. These stable values, averaged over contours 15-45 or 2.25 mm-7 mm (shaded region in Figure 2.8), were recovered as the *J*-integral. Subsequently, fracture modes were partitioned to obtain K_I and K_{II} for that time instant or load step. In the FE computations, four node bilinear plane stress quadrilateral element (CPS4R) of size 0.15 mm (scale factor × step size) with two degrees of freedom per node was

used. It should be noted that this element's shape and size were preferred to match the DIC grid. The potential error in the computed *J*-integral and SIFs due to crack tip location from the speckle images and the displacement contours was examined. The location of the crack tip was found to be within 2 pixels. Similar computation of fracture parameters with different crack tip locations to quantify the error associated with the identification of precise crack tip location was carried out and the results are shown in Figure 2.9. The resulting variability of the *J*-Integral and SIFs was less than 2%. The traditional approach provided an error of ~15%.

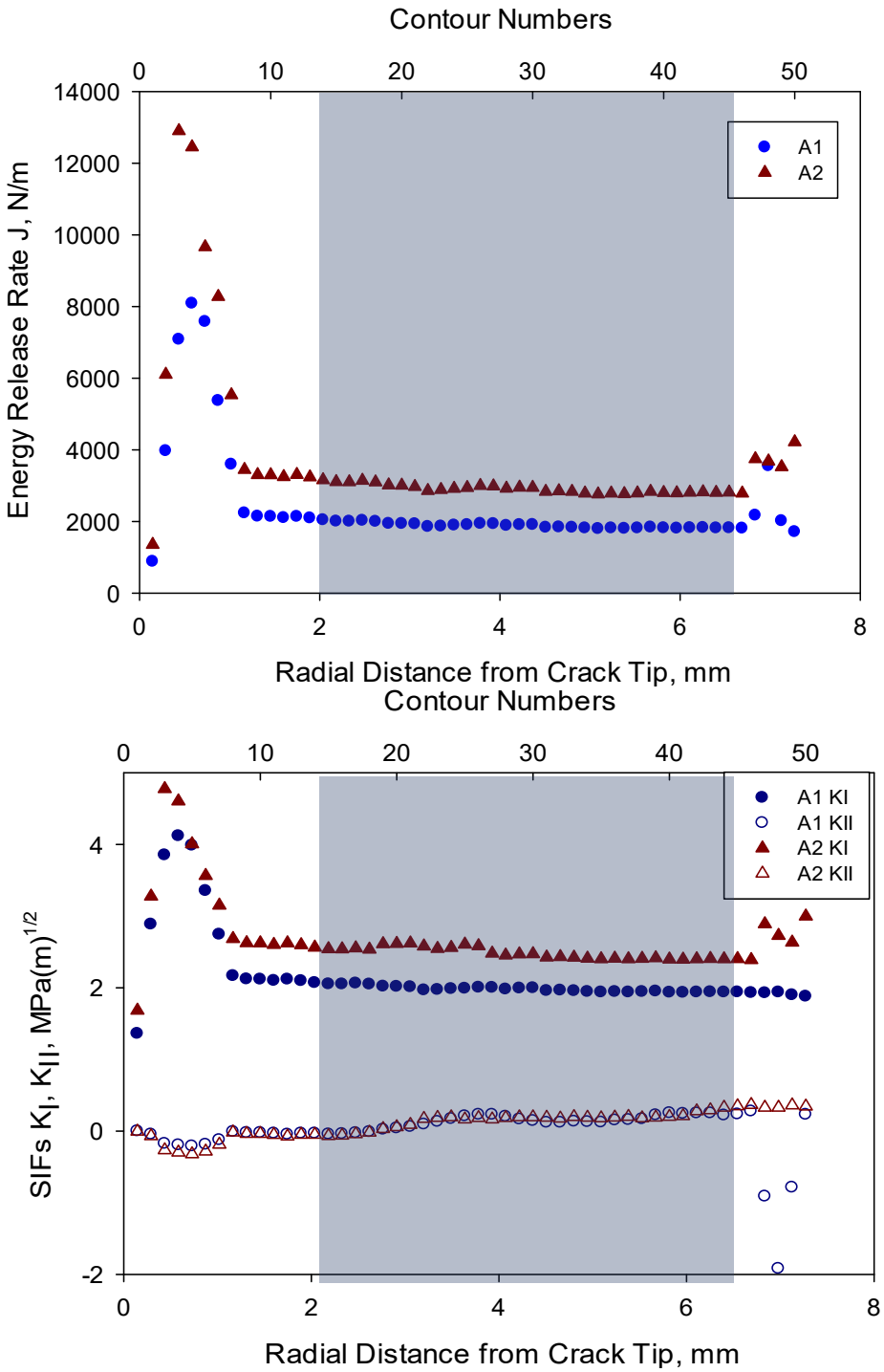

Figure 2.8: Variation of computed *J*-value and SIFs for AM ABS at an instant during crack growth.

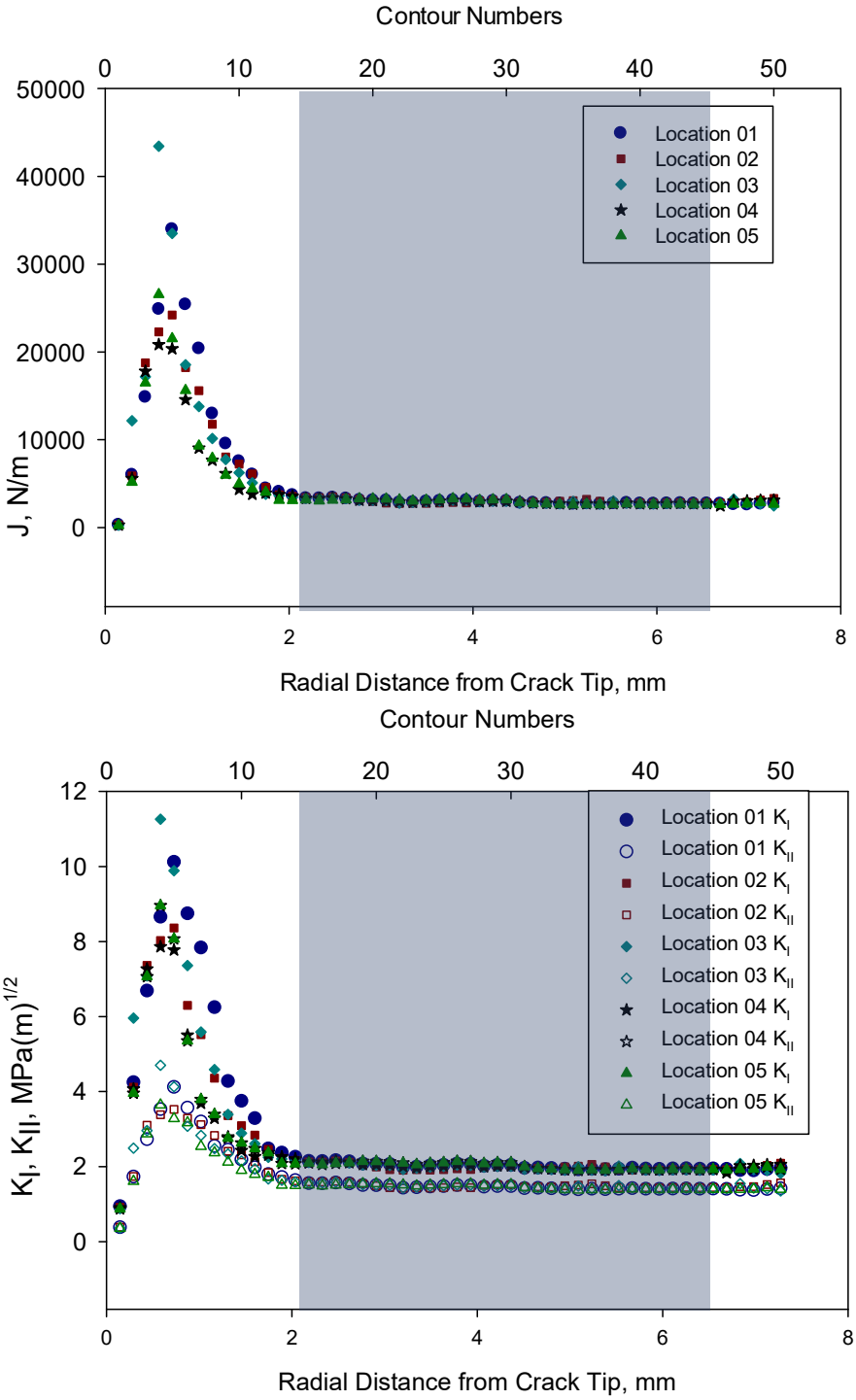

Figure 2.9: Variation of computed *J*-value and SIFs for AM ABS at an instant during crack growth. Each data set corresponds to five different crack tip locations due to identification errors. Contour #15-45 corresponding to approx. 2.25-7 mm or *r/B* ratio of 0.4-1.2 was used to find the average. The *J*-value and SIFs varies by < 5% in the shaded part for each location and < 2% between different locations.

Chapter 3. Quasi-Static Fracture

In this chapter, information about specimen preparation and details on the three print architectures studied in this work are detailed. This is followed by the tensile and fracture tests carried out under quasi-static loading conditions. Experimental details for each of the experiments are provided first, followed by the results and a discussion of the results. Fractography details are included as well.

3.1 Specimen preparation

A Cubicon 3DP-110F printer was used to print all specimens studied in this work. The desired geometry was modeled using Solidworks® and exported to a slicer software as a stereolithographic (.STL) file. All print settings and modifications were finalized using the slicer software and a G-code was generated and exported to the printer. Planar architectures namely, $[0^o]_n$, $[90^o]_n$, $[0^o/90^o]_n$, $[45^o/-45^o]_n$, and $[0^o/45^o/90^o/-45^o]_n$ were printed with identical printer parameters listed in Table 3.1. It should be noted that $[0^o/90^o]_n$ and $[45^o/-45^o]_n$ are default architectures in most 3D printers and the rationale for these architectures from the mechanical performance perspective is mostly intuitive. Therefore, for starters, the $[0^o/45^o/90^o/-45^o]_n$ architecture was chosen beside the $[0^o/90^o]_n$ and $[45^o/-45^o]_n$ to demonstrate that there could be other raster patterns among the infinite number of possibilities for achieving better mechanical performance. To further analyze the observed responses for the three print architectures and to know the contribution and behavior of each layer, unidirectional architectures were designed as *reference* architectures. The $[0^o]_n$ and $[90^o]_n$ architectures were used as reference architectures to explain the mechanical responses observed in mixed-direction builds namely $[0^o/90^o]_n$, $[45^o/-45^o]_n$, and $[0^o/45^o/90^o/-45^o]_n$. A 100% infill option

was selected for all architectures to obtain fully dense specimens and to avoid the effects of any additional porosity other than the one inherent to the printing process itself.

Table 3.1 – 3D printer parameters.

Print parameters	Values	Print parameters	Values
Extruder temperature	240 ºC	Layer thickness	0.2 mm
Bed temperature	115 ºC	Wall thickness	0.8 mm
Chamber temperature	50 ºC	Infill speed	80 mm/s
Flow	100%	Retraction Speed	40 mm/s

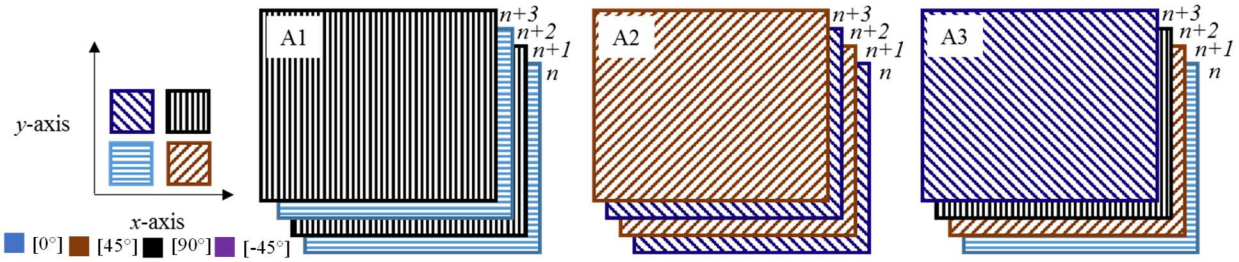

Figure 3.1: Build direction of each layer of print architectures designated A1, A2, and A3. A serpentine pattern was adopted during the printing of each layer of the architecture. *The hatch marks in each layer correspond to 0º, 45º, 90º, -45º directions.*

During printing, the outer wall was deposited first in each layer of the specimen and then the printer nozzle was moved in directions specific to the above patterns in the *x*-*y* plane. A schematic of the layer buildup (in the *z*-direction) used for the three architectures is shown in Figure 3.1. For the two *reference architectures* namely $[0º]_n$, $[90º]_n$, deposition in the *x*-*y* plane was all either parallel or perpendicular to the *x*-direction within the outer wall and simply repeated in the *z*-direction until the desired thickness was reached. Within each layer, the nozzle followed a serpentine path. In the mixed-direction prints such as $[0º/90º]_n$ configuration, a repeating two-layer buildup was adopted. That is, the printer nozzle was moved parallel to the *x*-axis for the first

layer and perpendicular to the *x*-axis for the second layer, and so on. This was repeated in the *z*-direction. Similarly, in the $[45^o/-45^o]_n$ architecture, the first layer was at 45º to the *x*-axis and the second layer was at -45º to the *x*-axis. In the $[0^o/45^o/90^o/-45^o]_n$ architecture, on the other hand, a repeating four-layer buildup of a combination of the two preceding architectures was implemented. That is, the first layer was along 0º, the second was along 45º, the third was along 90º and the fourth was along -45º to the *x*-axis. The subsequent layers were repeated thereafter. *Henceforth, for simplicity of description,* $[0^o/90^o]_n$, $[45^o/-45^o]_n$, *and* $[0^o/45^o/90^o/-45^o]_n$ *architectures will be identified as* A1, A2 *and* A3*, respectively.* Although ABS is a nominally isotropic material, because of the differences in raster orientations, anisotropy in terms of weak planes occurs in the printed specimens.

3.2 Experimental details

3.2.1 Tensile tests

First, uniaxial tension tests were carried out on all three print architectures A1, A2, and A3, described earlier. An Instron 4465 mechanical tester fitted with a 5 kN load cell was used to carry out tests on dog-bone-shaped specimens of 8 mm width and 4 mm thickness in the gage section. Figure 3.2 shows the dimensions of the specimen used. They were sprayed with fine mists of black and white paint to create random speckles on one of the surfaces to perform 2D-DIC in the gage section and measure in-plane deformations. A PointGrey camera (2048×2048 pixels resolution fitted with an 18-108 mm focal length macro zoom lens) recorded the event at a rate of 2 frames per second (fps). The region of interest (ROI) captured by the camera is highlighted on the specimen geometry by the red dotted lines. Figure 3.3 shows a photograph of the tensile testing setup. The specimen's surface with the speckle pattern was illuminated by ordinary polychromatic

lamps during the experiment. The experiments were performed in displacement control mode at a crosshead speed of 0.05 mm/s. During each test, time, load, and crosshead displacement data were all recorded until the specimen failed.

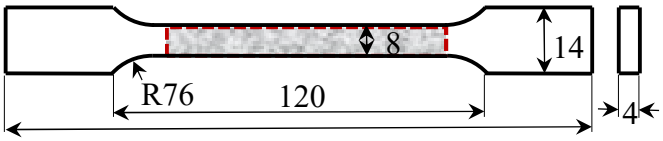

Figure 3.2: Tension specimen geometry. (*All dimensions are in mm*)

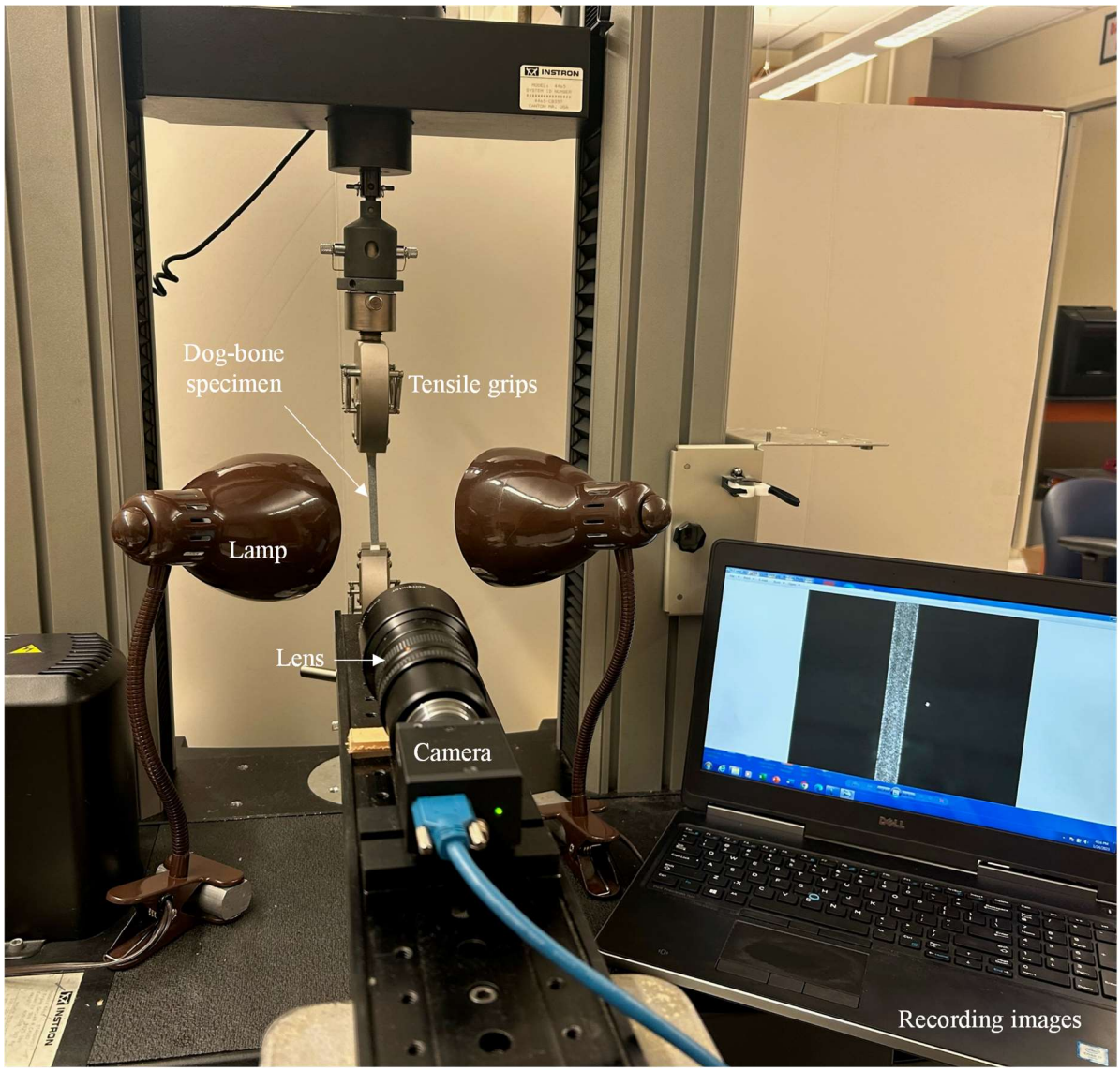

Figure 3.3: Tensile testing setup.

3.2.2 Tension and shear tests on reference architectures

Uniaxial tension and pure shear tests were carried out next on the two reference architectures with $[0^o]_n$ and $[90^o]_n$ raster orientation. This included separate uniaxial tension tests on plain $[0^o]_n$ and $[90^o]_n$ architectures, and Iosipescu shear tests[67] on $[0^o]_n$ samples. Uniaxial tension specimens' geometry is the same one as shown in Figure 3.2. Iosipescu shear test specimen geometry and loading configuration are shown in Figure 3.4. As noted earlier, in these reference architectures, all the layers over the entire build thickness in the *z*-direction of the sample were unidirectional but other specimen details were the same as the ones used for A1, A2, and A3.

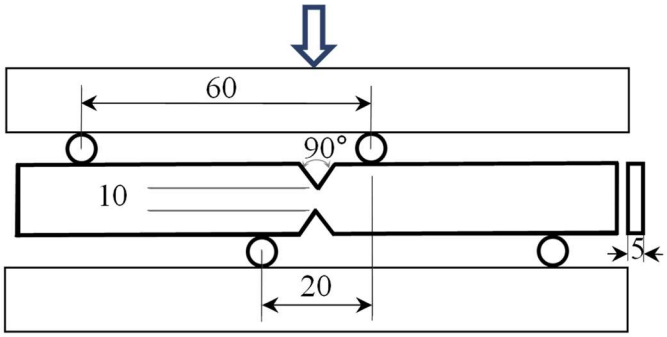

Figure 3.4: Iosipescu shear tests specimen geometry and loading configuration. (*All dimensions are in mm*)

3.2.3 Fracture tests

Next, fracture tests were carried out under quasi-static loading conditions on all three print architectures - A1, A2, and A3. Figure 3.5 shows dimensions of edge-notched symmetric three-point bend specimens. A 9 mm long notch was inserted into the specimen edge using a 0.3 mm thick circular saw at the mid-span and its root was sharpened by scoring the notch-front with a razor blade to achieve a sharp starter crack (Figure 3.5). Again, an Instron 4465 mechanical tester with a 5 kN load cell, equipped with a roller loading pin of diameter 0.5 inch, was used to carry

out these experiments at a crosshead speed of 0.007 mm/s and time, load, and crosshead displacement data were all recorded during each test. As in the tension tests, a fine coat of random speckles was sprayed on one of the surfaces of the specimen to perform DIC and quantify in-plane displacements. Again, the PointGrey camera was used to record the speckle images at 2 fps during tests. As in the tension tests, specimens of all three architectures were tested until crack initiation and significant growth occurred. A summary of the experimental parameters related to 2D-DIC is listed in Table 3.2. Figure 3.6 shows a photograph of the fracture test setup.

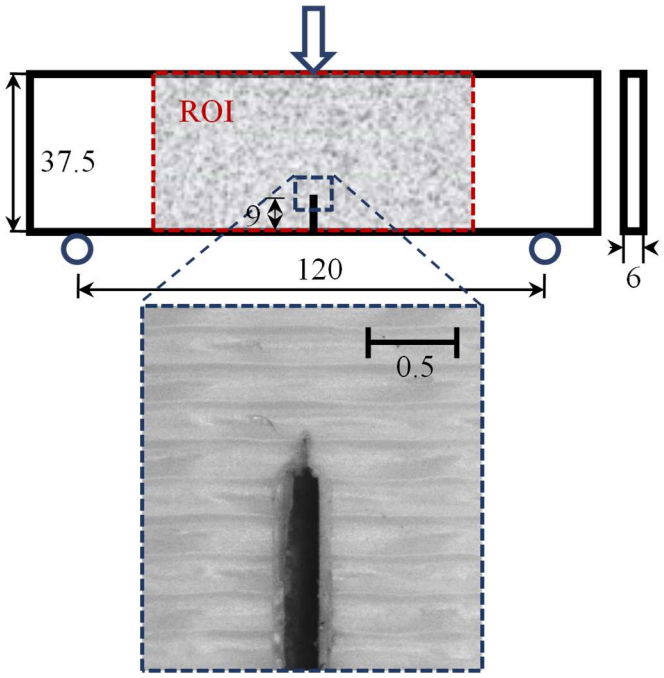

Figure 3.5: Quasi-static fracture specimen loading and geometry with an inset of the crack tip sharpened by a razor blade. (*All dimensions are in mm*)

Table 3.2 – DIC parameters associated with the quasi-static fracture experiments.

Hardware Parameters		**Analysis Parameters**	
Camera Manufacturer Model Image Resolution	Point Grey Grasshopper3 GS3-U3-41C6M 2048 x 2048	Software Package Name Manufacturer	Aramis® 6.2.0 GOM
Lens Manufacturer Model Focal Length	Computar Lens 18-108 mm	Image Filtering	None
FOV	60 mm x 60 mm	Sub-image/Subset Size	25 x 25
Image Scale	33.3 pixel/mm	Step Size	5
Stereo-Angle	N/A	Subset Shape Function	Affine
Stand-Off Distance	0.8 m	Data Processing and Filtering for QOIs	None
Image Acquisition Rate	2 fps	Noise-floor and Bias of QOIs	1 μm
Patterning Technique	Spray painted		
Approx. Feature Size	5 pixels		

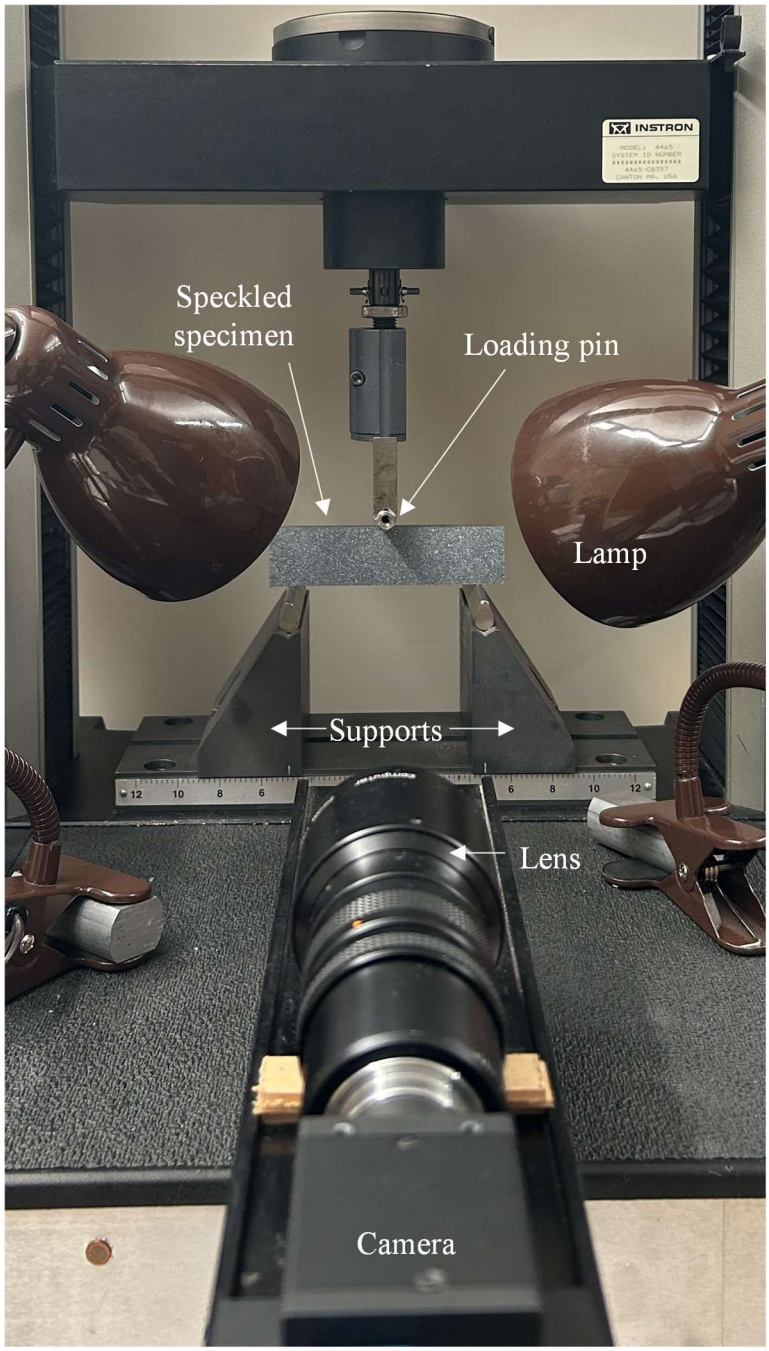

Figure 3.6: Quasi-static fracture test setup.

3.3 Results

3.3.1 Tension tests

The tensile stress-strain responses on two sets of specimens of all three architectures were measured. Results for one of the two sets are shown in Figure 3.7.

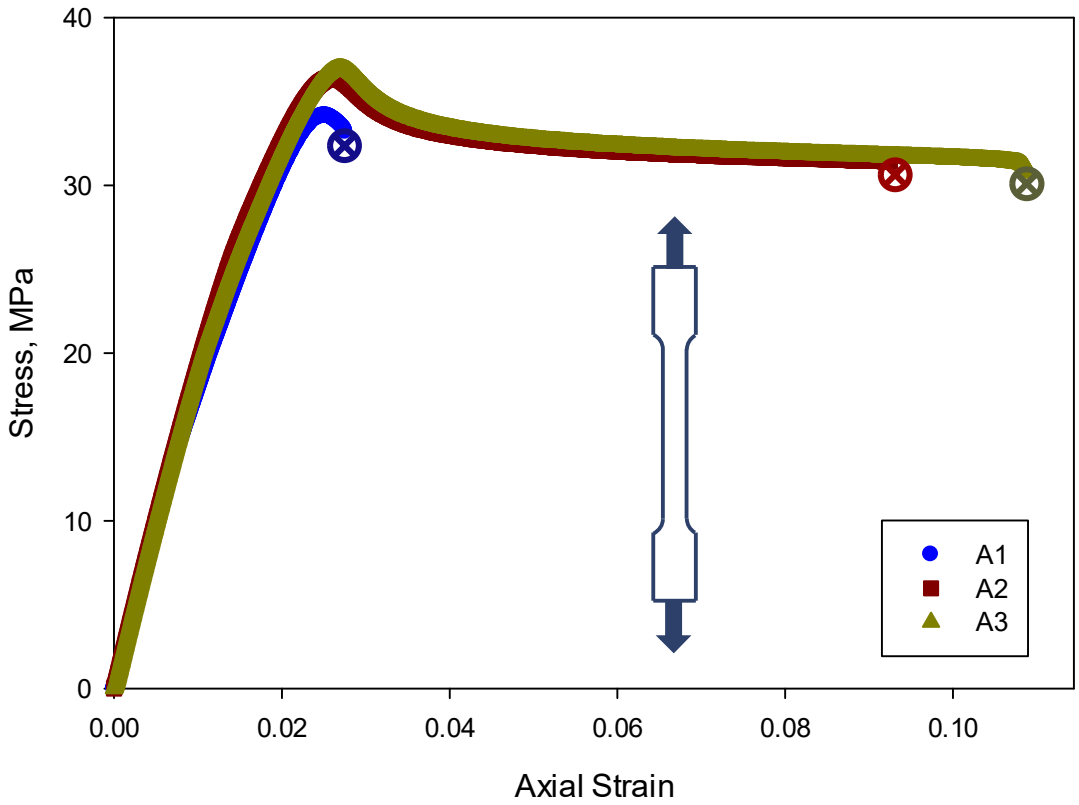

Figure 3.7: Tensile stress-strain responses of dog-bone specimens of different print architectures. (The cross marks indicate specimen failure)

Graphs for each specimen type initially showed a linear response, up to approx. 1.5% engineering strain and *overlap on each other. This suggests that despite the differences in print architectures of* A1, A2 *and* A3*, they are all elastically identical.* The elastic modulus was measured in each case using linear regression of data up to 0.1% strain. The spray-painted random speckles on one of the surfaces were recorded to measure longitudinal and lateral strains in the

gage section of the specimen using DIC to enable evaluation of the elastic constants E and v for each architecture. A pair of representative strain fields from a uniaxial test on A1 architecture is shown in Figure 3.8. The strains from DIC were relatively uniform in the gage section (Figure 3.8(a)). The figure also shows stress vs. axial and transverse strain plots (Figure 3.8(b)) in the linear range for this architecture. These tension tests were repeatable for all three architectures. Two test results are shown for each of the architectures in Figure 3.9 and good repeatability is self-evident.

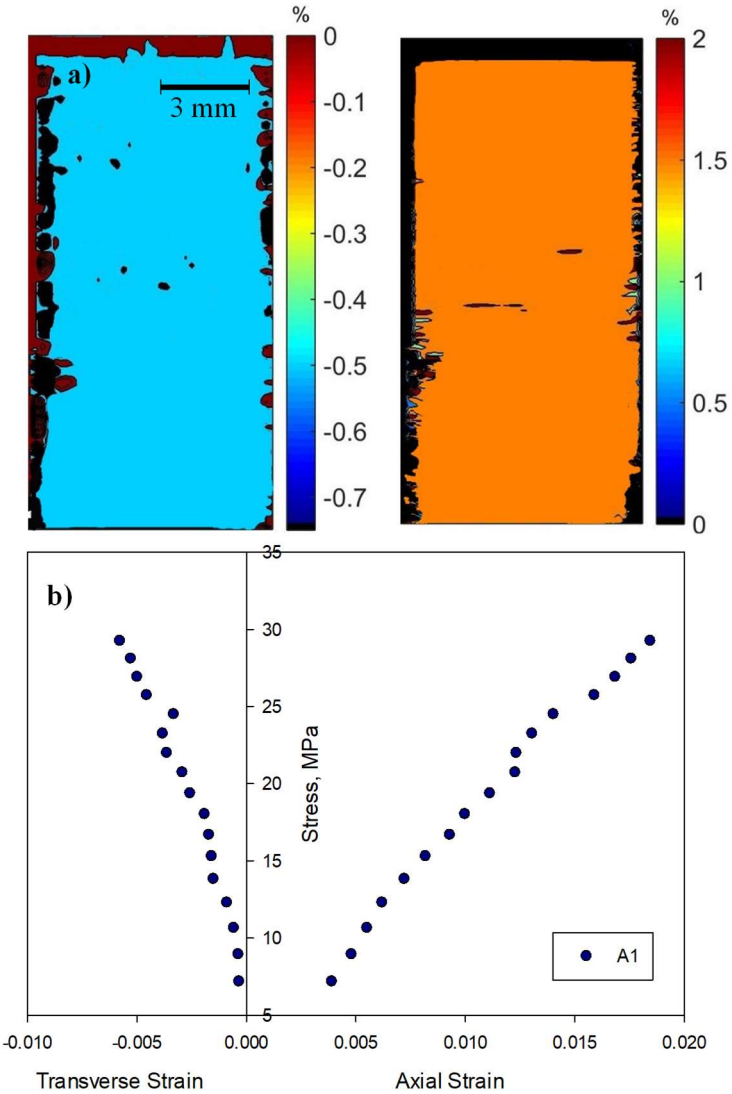

Figure 3.8: Uniaxial tension test results from DIC: (a) ε_{xx} and ε_{yy} strain fields of A1 architecture (b) Stress vs. axial and transverse strain plots of A1 architecture used to calculate elastic modulus and Poisson's ratio.

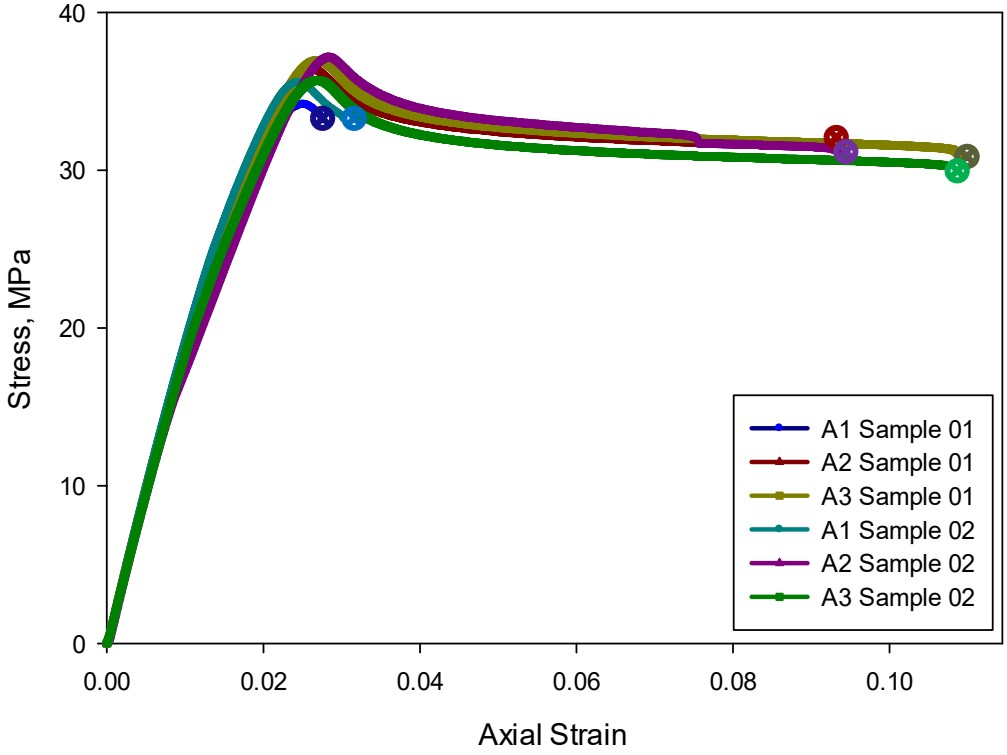

Figure 3.9: Repeatability for tensile stress-strain responses for all three architectures.

The elastic modulus (E) and the Poisson's ratio (ν) were found to be nearly same for all the three architectures and the differences in E was less than 4%. In addition to the elastic constants, Table 3.3 lists other parameters from the uniaxial tension experiments. Each of the architectures showed a peak stress followed by a softening response, either with or without a distinct plateau region before an abrupt failure. The A1 architecture was found to have the lowest failure stress, peak/ultimate stress and strain at failure. The A2 architecture had a marginally higher (~7%) peak stress relative to A1 (0º/90º case) whereas there was a substantial increase in the failure strain, by over 230%. The A3 architecture had a response similar to that of A2 [45/-45º case] in terms of its peak stress. The failure strain, however, was even higher (by ~17%) relative to the A2 architecture (or, by 290% relative to A1). The increase in the strain at failure signifies higher ductility observed

in the A2 and A3 architectures relative to A1. *More interestingly, the higher ductility of* A3 *relative to* A2 *was unexpected.*

Table 3.3 – Material properties obtained from tensile tests.

Material Property	**A1**	**A2**	**A3**
Elastic modulus (GPa)	2.07	2.14	2.14
Poisson's ratio	0.34	0.34	0.34
Failure stress (MPa)	34.1	36.3	36.8
Failure strain %	2.8	9.3	10.9

To understand these differences in stress-strain responses due to print architectures, particularly in the inelastic regime, images of failed cross-sections from tension tests were recorded using a Keyance VHX 6000 digital microscope and are shown in Figure 3.10. In the A1 architecture, thinning of individual print layers normal to the loading direction was visible along with evidence of disbonded layers. The A2 architecture shows relatively denser fracture surface with large regions of failure in shear, seen as swaths of featureless zones connected by shear steps, consistent with the higher ductility relative to A1. The A3 architecture shows features in between those of A1 and A2 with partial alignment of the disbonded layers and shear steps with smaller featureless zones. These differences in features are attributed to higher ductility and toughness of A2 and A3 architectures.

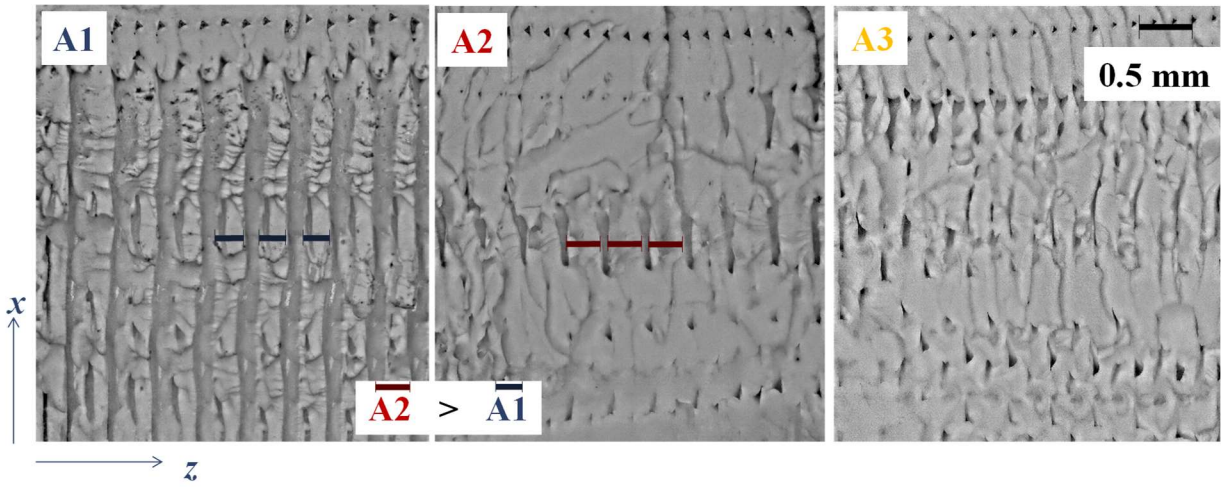

Figure 3.10: Optical micrographs of fractured cross-section of tensile specimens. (Blue and Red bars highlight the relative thinning of individual print lines in A1 relative to A2)

3.3.2 Tension and shear tests on reference architectures

The stress-strain responses for the reference architectures are shown in Figure 3.11 and the calculated tensile parameters are listed in Table 3.4. Figure 3.11(a) and (b) shows the tensile stress-strain responses. The results (peak stress ~35 MPa for 0° print and ~40 MPa for the 90° print, strain-at-failure ~2.4% in both cases) are nearly same as the one for the A1 (Figure 3.7) architecture. The pure shear tests (Figure 3.11(c)) based on Iosipescu geometry, on the other hand, show that the ultimate shear stress is ~35 MPa, close to the tensile strength of the unidirectional coupons. However, the shear strain at failure is ~23%, *ten times higher than the tensile failure strain of the 0° or 90° prints* (and the A1 architecture).

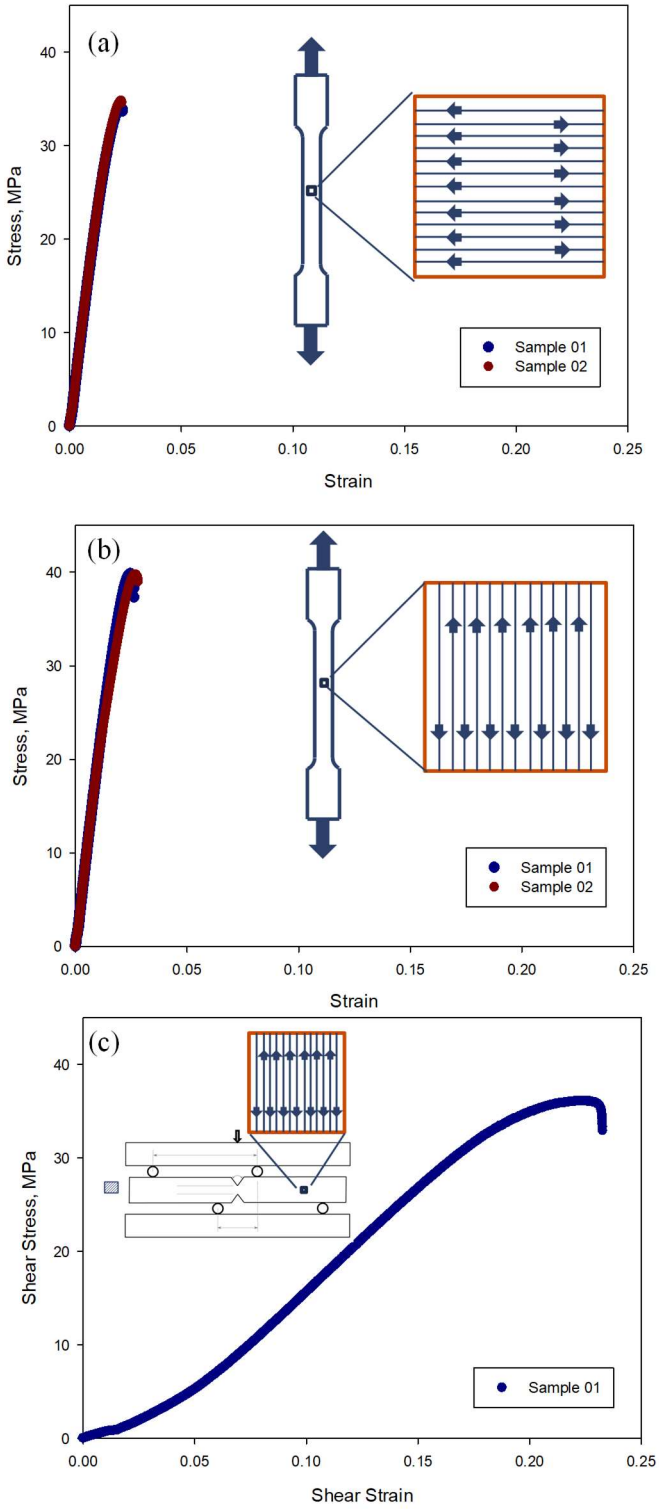

Figure 3.11: Tensile and shear responses of unidirectionally printed reference coupons. (a) Stress-strain plots for unidirectional $[0°]_n$ tensile samples with print architecture. (b) Stress-strain plots for unidirectional $[90°]_n$ tensile samples with print architecture. (c) Shear stress-shear strain plots for $[0°]_n$ Iosipescu tests with specimen geometry, loading and print architecture.

Table 3.4 – Material properties of reference architectures.

Material Property	$[0°]_n$	$[90°]_n$	Iosipescu Shear
Elastic/Shear modulus (GPa)	2.10	2.15	0.8
Poisson's ratio	0.34	0.34	0.34
Failure stress (MPa)	34.8	39.8	36.1
Failure strain %	2.2	2.4	22.2

3.3.3 Fracture tests

The load vs. load-point displacement plots for edge-cracked 3-point bend specimens for all three architectures are shown in Fig. 10(a).

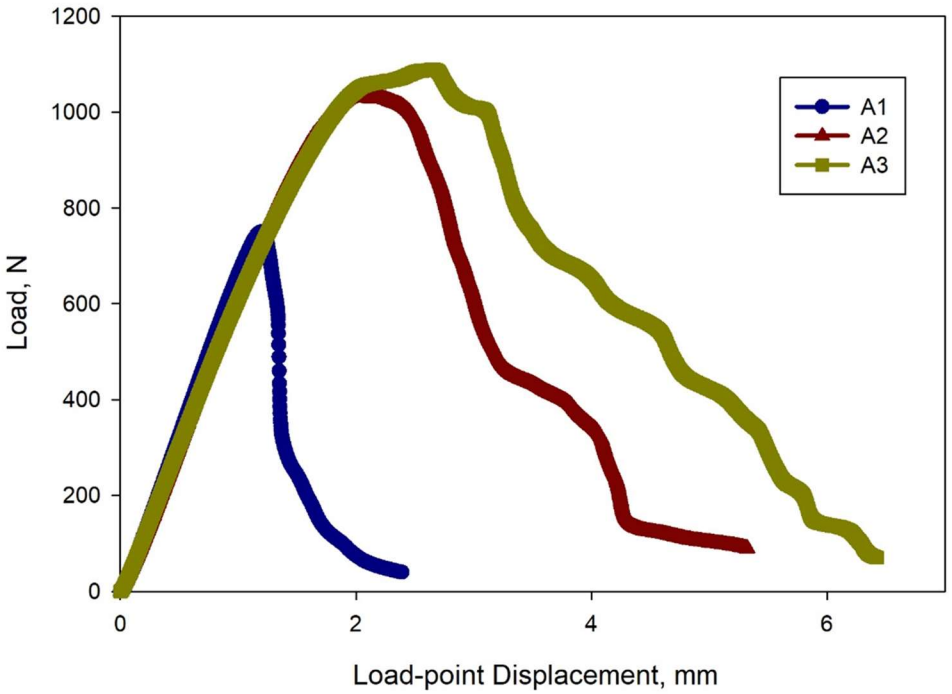

Figure 3.12: Effect of print architecture on load vs load-point deflection for quasi-static three-point bend specimens.

The response for the A1 architecture shows a relatively brittle response when compared to A2 and A3 counterparts. Following a linear increase up to crack initiation occurring at a peak load, a precipitous drop in load until complete fracture occurred in A1. In the A2 and the A3 architectures, on the other hand, the response was linear up to crack initiation and was significantly higher (~40%) relative to the A1 architecture. More importantly, a relatively gradual (as opposed to an abrupt) drop in load occurred during crack growth in A2 and A3 architectures. Furthermore, the A3 architecture showed visibly wavy load-deflection response during crack growth relative to A2. To quantify these observations, histograms of energy absorbed (area under the curve) by the three architectures before and after crack initiation were obtained and are shown in Figure 3.13. The energy absorbed before crack initiation was approx. 130% higher for the A2 and A3 architectures relative to A1, whereas the energy absorbed during crack propagation was ~800% higher for the A2 and 1400% higher for the A3 architecture relative to A1. These values are consistent with the higher ductility of A2 and A3 architectures observed relative to A1.

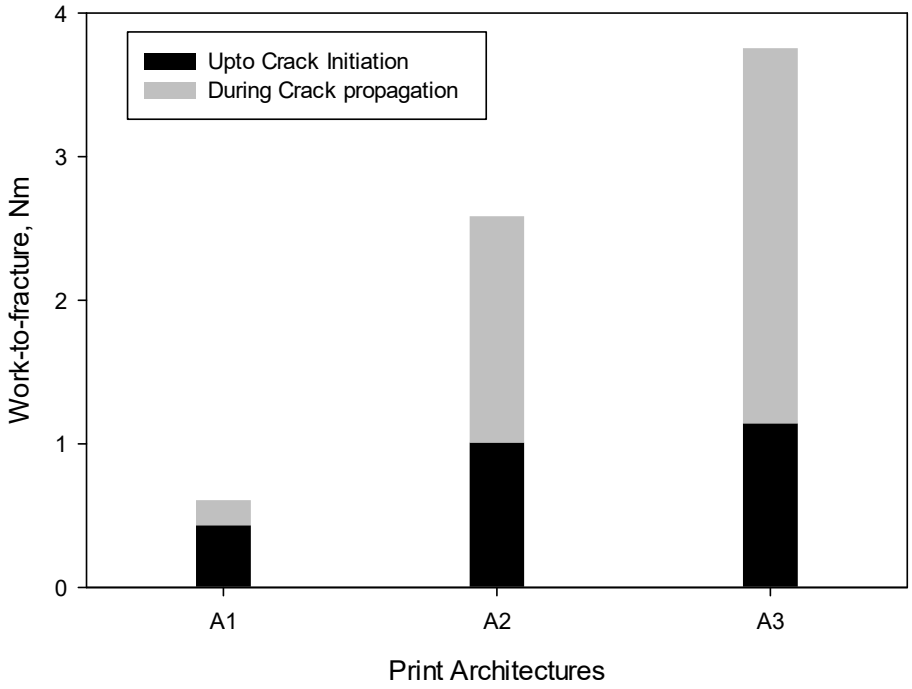

Figure 3.13: Work done on each print architecture before and after crack initiation in quasi-static experiments up to load drop to 200 N.

Figure 3.14 shows photographs of the reassembled fractured specimens to illustrate crack propagation in all three architectures under quasi-static loading conditions. In the A1 architecture, the crack propagated self-similarly or along the direction of the pre-crack. On the other hand, the crack propagated in a staircase pattern, in one of the two 45º directions, in A2 whereas in A3, the crack growth was locally and incrementally along ±45º as well as 0º directions with a substantial meandering and frequent jumps in between different layers along the crack path. *The latter is consistent with the wavy load-deflection response seen in Figure 3.12*. As a result, the overall macroscopic crack growth direction is noticeably different from the ±45º directions observed in A2. Evidence of crazing (or whitening), though not readily evident from the photographs due to the white color of ABS material used, was also observed at the crack tip and along the crack flanks indicating significantly higher crack growth resistance in the A2 and A3 architectures relative to

A1. The manifestation of shear deformations along the crack path is clearly visible from the noticeable kink in crack surface striations in A3.

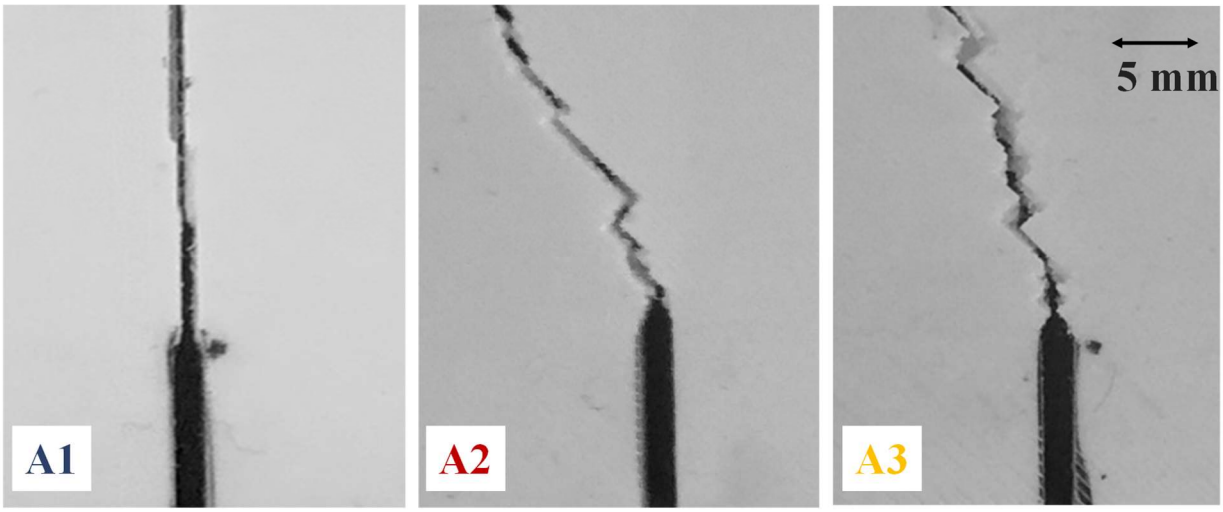

Figure 3.14: Photographs of observed crack paths in fractured 3-point bend specimens. (The specimen A3 is flipped by 180^{o} for consistency with A2).

The gray scale photographs of surface speckles (Figure 3.15(a), Figure 3.16(a), and Figure 3.17(a)) recorded by the camera in the deformed state were correlated with the reference images recorded before the application of load to obtain the displacement component fields in two orthogonal directions, along (x) and perpendicular (y) to the initial crack orientation. An image analysis software, ARAMIS®, was used to perform gray scale correlation by segmenting images into 25×25 pixel sub-images with 5 pixels step size. The scale/magnification factor was ~30 µm/pixel for these images. Figure 3.15, Figure 3.16, and Figure 3.17 shows representative contours of two select orthogonal displacement components namely, u- and v-fields in the x- and y-directions, respectively, for the three architectures. (It should be noted that the *displacement data are available as rectangular arrays over the ROI and at the center of each sub-image although they are displayed as contours* in these figures after post processing.) In each figure, one pair of displacement contours along with the respective speckle images, in the 'before' and 'after' crack

initiation phases is presented. Away from the crack tip region, the deformations are consistent with the ones for flexural loading. As expected, the displacement fields near the crack tip vicinity are symmetric (mode-I) in the A1 architecture before and after crack initiation whereas they show noticeable asymmetry and mixed-mode (mode-I and -II) characteristics once the crack initiates in the A2 and A3 architectures. The crack tip was identified using crack opening displacement contours and the respective speckle images. Then, as discussed earlier, the experimentally measured displacement field data from DIC for every image was imported into the respective FE mesh as two orthogonal boundary conditions at the corresponding nodes to compute the strain and stress fields. Subsequently, the fracture parameters namely the *J*-integral, K_I and K_{II} were all outputted by ABAQUS.

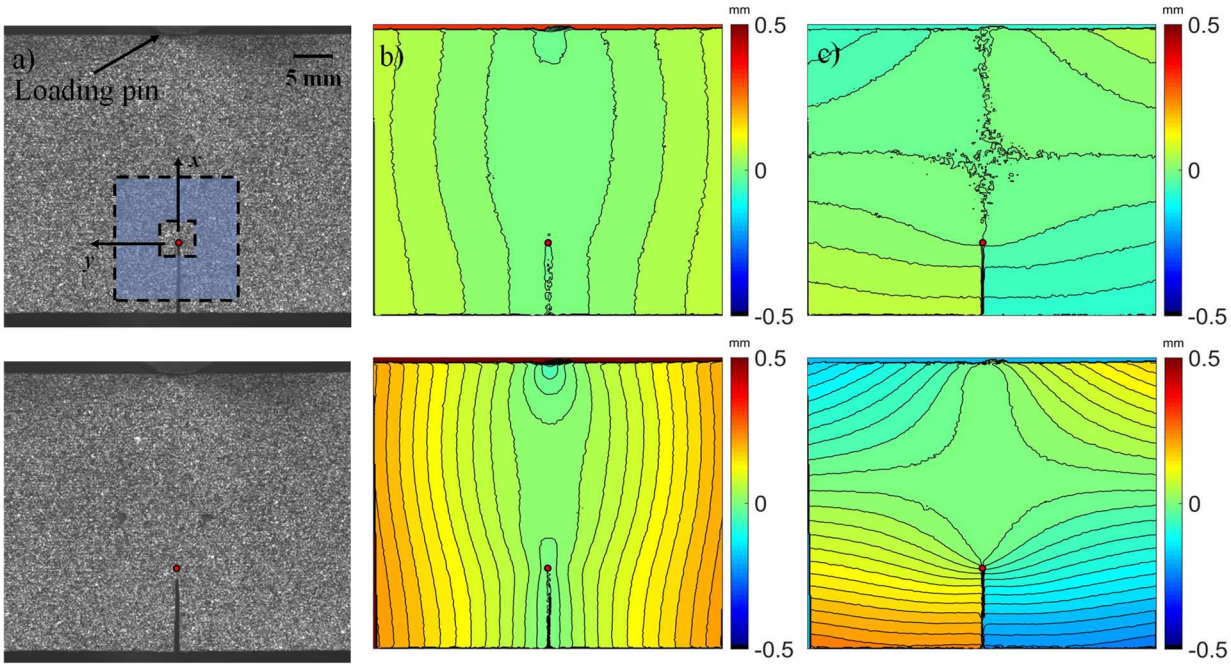

Figure 3.15: Displacement contours of A1, with a contour interval of 20 µm, obtained through DIC (a) Speckle images at a load step and its corresponding (b) *x*- or *u*-field, (c) *y*-or *v*-field. Red solid dots indicate the crack tip location at this time/load step. The top row corresponds to pre-crack initiation (Load = 500 N) and bottom row corresponds to post-crack initiation (Load step = 620 N) stages. (The shaded zone in the speckle image corresponds to the region where the *J*-integral is computed.)

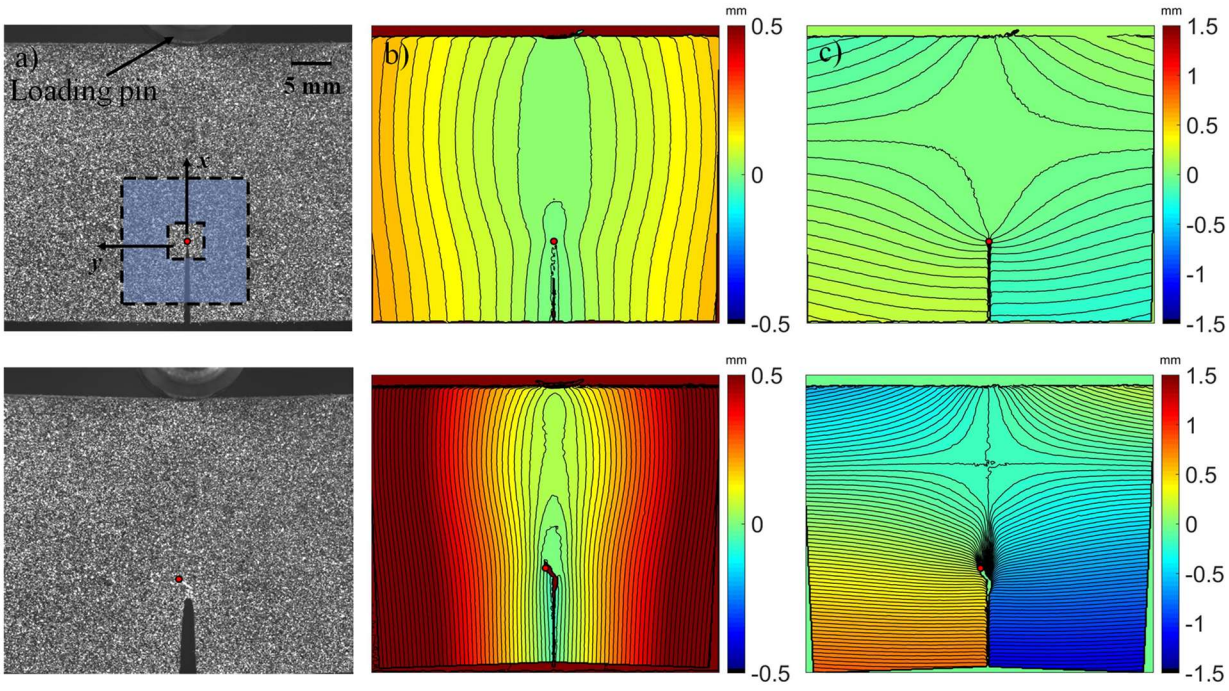

Figure 3.16: Displacement contours of A2, with contour interval of 20 μm, obtained through DIC (a) Speckle images at a load step and its corresponding (b) *x*- or *u*-field, (c) *y*-or *v*-field. Red solid dots indicate the crack tip at this time step. The top row corresponds to pre-crack initiation (Load = 530 N) and bottom row corresponds to post-crack initiation (Load = 890 N) stages.

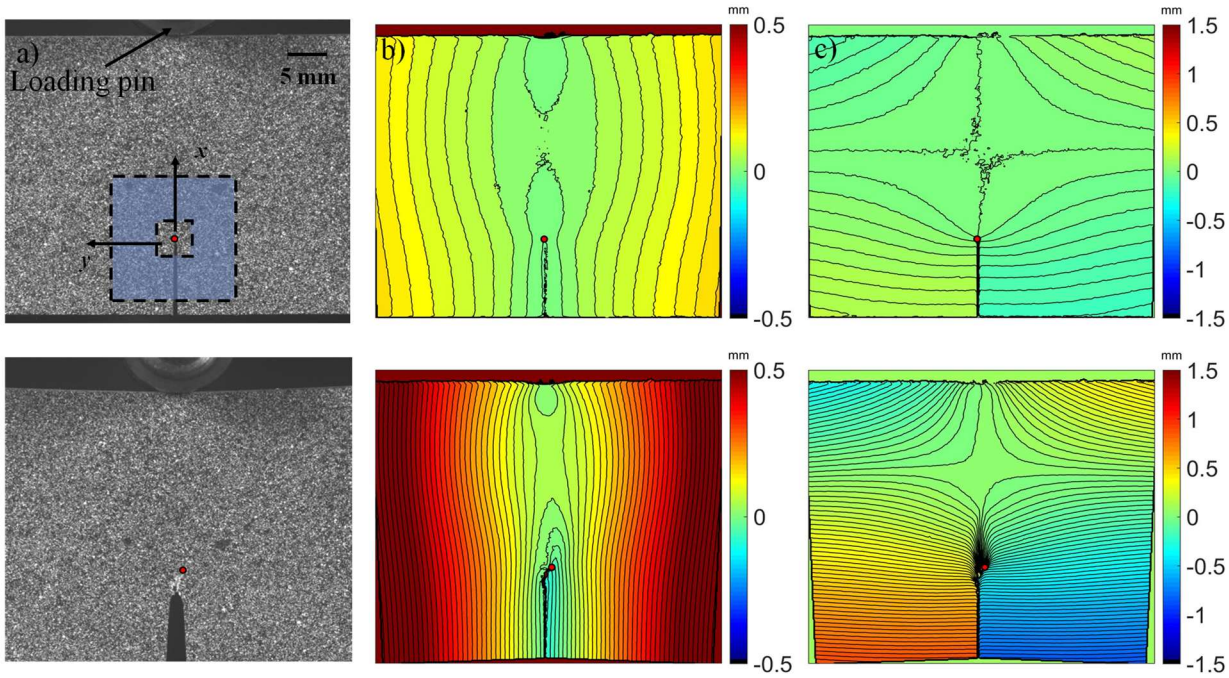

Figure 3.17: Displacement contours of A3, with contour interval of 20 µm, obtained through DIC. (a) Speckle images at a load step and its corresponding (b) *x*- or *u*-field, (c) *y*-or *v*-field. Red solid dots indicate the current crack tip at each time/load step. The top row corresponds to pre-crack initiation (Load = 510 N) and bottom row corresponds to post-crack initiation (Load step = 991 N) stages.

Figure 3.18 shows the crack growth resistance or *J-a* plots for all the three architectures. It can be observed from the graphs that the resistance to crack initiation, as expected, was the lowest for the A1 architecture (1850 N/m) and the same was approx. 55% higher for A2 (2900 N/m) and 35% higher for A3 (2500 N/m) architectures. After crack initiation, the crack growth resistance for the A1 architecture remained approx. constant or $dJ/da \sim 0$ whereas the A2 architecture showed an abrupt drop in resistance ($dJ/da < 0$ or unstable growth relative to its value at initiation) after crack initiation before building back resistance and attain $dJ/da > 0$. The A3 architecture, unlike the A2 counterpart, after crack initiation showed a steady increase in values or $dJ/da > 0$ before plateauing at ~4000 N/m, higher than that for A2 over the same amount of crack growth. The

maximum values of the *J*-integral for each of these architectures in the window of observation were approx. 2250, 4000, 4450 N/m for A1, A2, and A3, respectively.

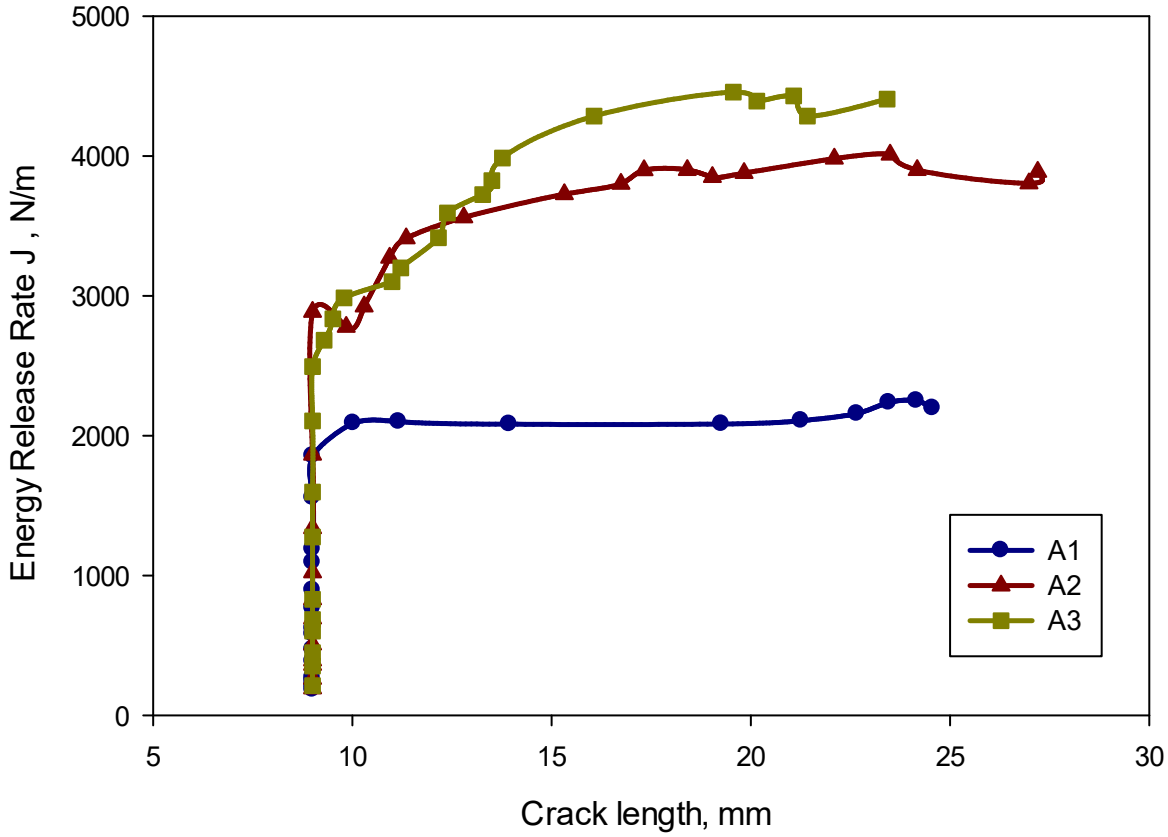

Figure 3.18: Crack growth resistance curves for three-point bend specimens under quasi-static condition.

Figure 3.19 shows the *J*-integral histories from the 3-point bend specimens. To compare the fracture behaviors, *the time axes for each case are shifted such that t = 0 corresponds to crack initiation*. That is, the negative and positive *t* values correspond to pre- and post-initiation regimes, respectively. The repeatability of *J* vs. *t* was also ensured across multiple samples and architectures. Two such examples are shown in Figure 3.20. Observations and characteristics similar to the ones made for the resistance behaviors (Figure 3.18) can be made again. The

architecture A1 had a brittle response whereas A2 and A3 were relatively tougher. Again, the A2 architecture showed a noticeable drop in the *J*-integral immediately after crack initiation whereas A3 had a steady increase with respect to time. As noted earlier, the *J*-integral computed from the proposed hybrid method was partitioned into mode-I and -II SIF histories under small scale yielding assumptions. The assumption was first verified by evaluating the SIFs using the load vs. load-point plots (Figure 3.12) in the closed form solution for 3-point bend specimen configuration,

$$K_I = \frac{F \cdot S}{B \cdot W^{3/2}} \frac{3\alpha^{1/2}[1.99 - \alpha(1-\alpha)\{2.15 - 3.93\alpha + 2.7\alpha^2\}]}{2(1+2\alpha)(1-\alpha)^{3/2}}, \qquad \alpha = \frac{a}{W} \tag{3.1}$$

where *F*, *S*, *W*, *B* and *a* denote applied load, beam span, height, thickness and crack length, respectively. This is shown for A1, A2 and A3 architectures in Figure 3.19 where the solid symbols are the ones obtained from the DIC-FE analyses and the open symbols are from Eq. 4. Good agreement between the two is evident in each case (error percentages for A1, A2 and A3 at crack initiation are ~3.1%, ~6.2% and ~7.3% respectively).

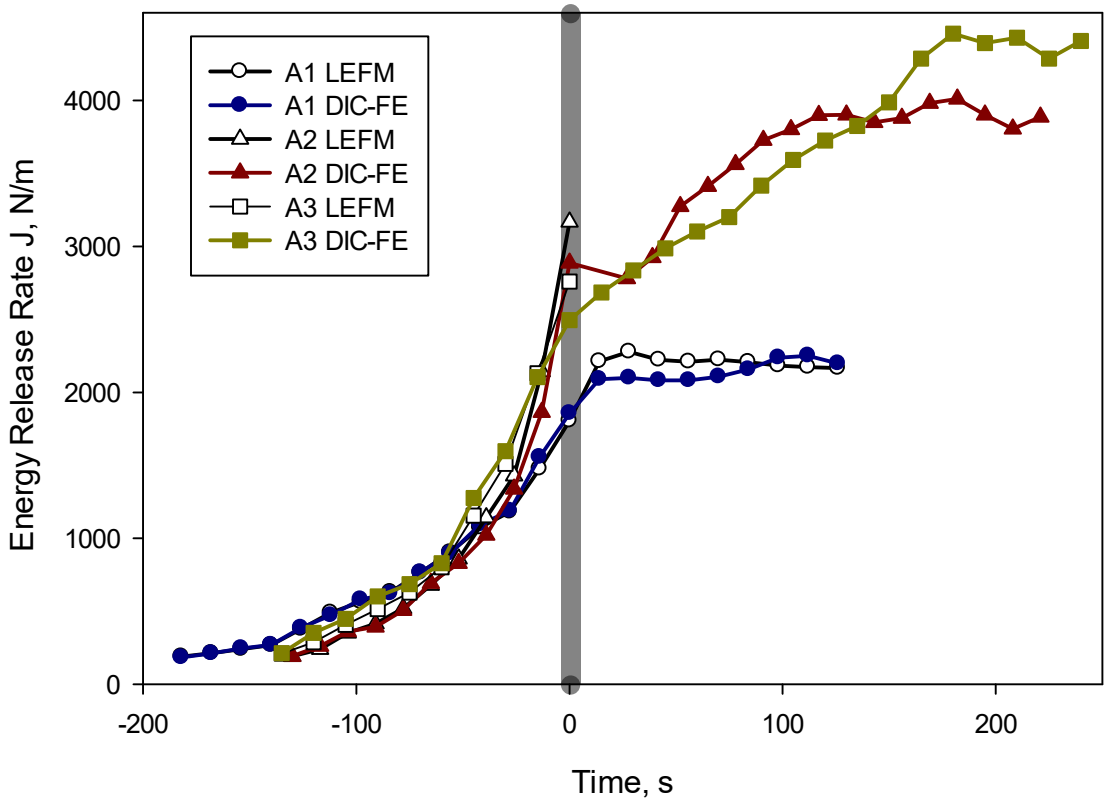

Figure 3.19: The *J*-Integral histories for 3-point bend specimens under static conditions. Comparison between the hybrid DIC-FE approach and closed form solution based on small scale yielding for A1, A2 and A3 architectures. (Negative and positive times correspond to pre- and post-crack initiation regimes.)

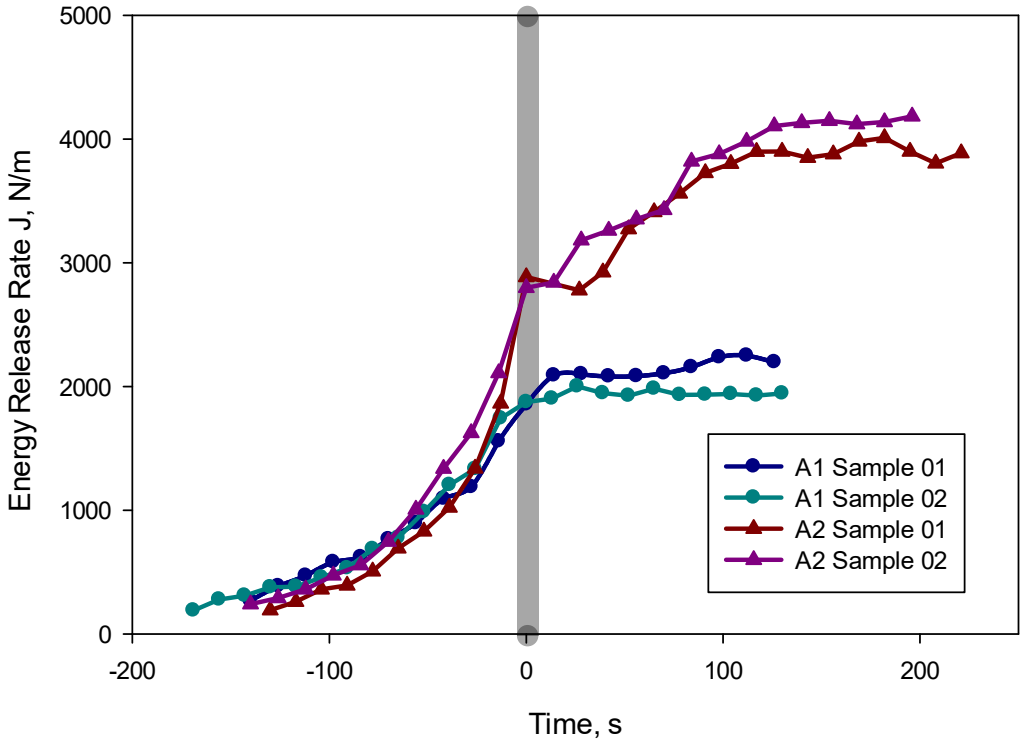

Figure 3.20: Repeatability for *J* vs. Time plots for the A1 and A2 architectures.

The comparison for A2 and A3 is limited up to crack initiation since the closed form solution is invalid after crack initiation when it kinks away from its initial path whereas it is valid for the self-similar crack growth case of A1. This agreement can be further confirmed by the dominant strain, ε_{yy}, field for the three architectures (Figure 3.21). Given the strain component corresponding to the peak stress for these materials is ~2%, strains of that magnitude are highly localized to the crack tip region < 2.5 mm radius beyond which the values drop-off rapidly and facilitate a successful adaptation of small scale yielding when computing individual SIF values.

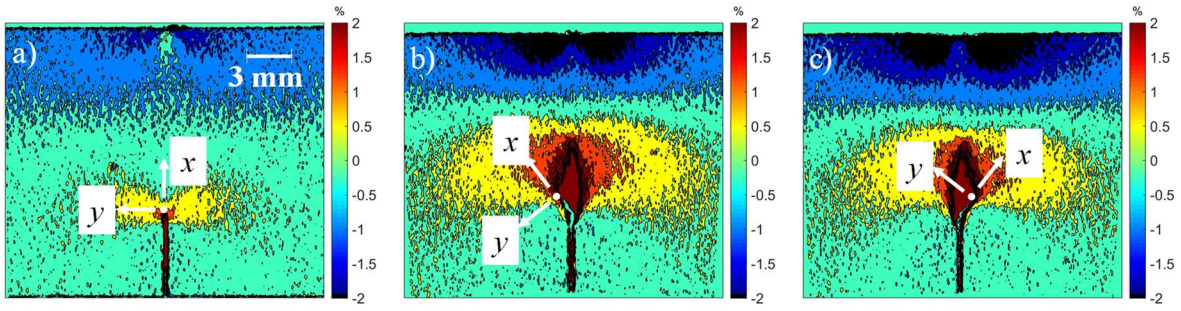

Figure 3.21: Dominant ε_{yy} strain fields for (a) A1 (Load = 661 N), (b) A2 (Load = 710 N) and (c) A3 (Load = 740 N) architectures *during crack propagation*. Solid dots indicate the crack tip location at this time/load step.

Figure 3.22 shows individual SIF histories for all the three architectures under quasi-static loading conditions. Again, the negative and positive *t* values correspond to pre- and post-initiation regimes, respectively. As in the load vs load-point displacements plots (Figure 3.12), A2 and A3 architectures had higher crack initiation SIF (or crack initiation toughness) relative to the A1 counterpart. All the three architectures had a monotonic increase in the effective SIF ($=\sqrt{K_I^2 + K_{II}^2}$) until crack initiation (not shown here for brevity). In terms of the mode-I SIF, K_I, the A2 architecture had the highest crack initiation toughness of ~2.4 MPa√m followed by ~2.2 MPa√m for the A3 and ~1.9 MPa√m for the A1 architecture. In case of A1, after crack initiation, K_I values remained constant. The A2 architecture, on the other hand, showed a rapid and significant drop in the K_I values after crack initiation followed by somewhat steady state values, well below that for A1, in the observation window. The mode-II SIF, K_{II}, on the other hand, after crack initiation showed a rapid rise followed by a steady state where the values reached the one at crack initiation. In the A3 architecture, after crack initiation, a gradual drop in K_I was observed followed by a steady state region, below that for A1 but significantly higher than that for A2, for the rest of the window of observation. The K_{II} values again had a rapid increase after crack initiation which eventually reached a steady state more gradually when compared to that for A2. These suggest that

a relatively desirable failure of the A3 architecture relative to the other two although the crack initiation occurred at a slightly lower mode-I SIF when compared to the A2 counterpart.

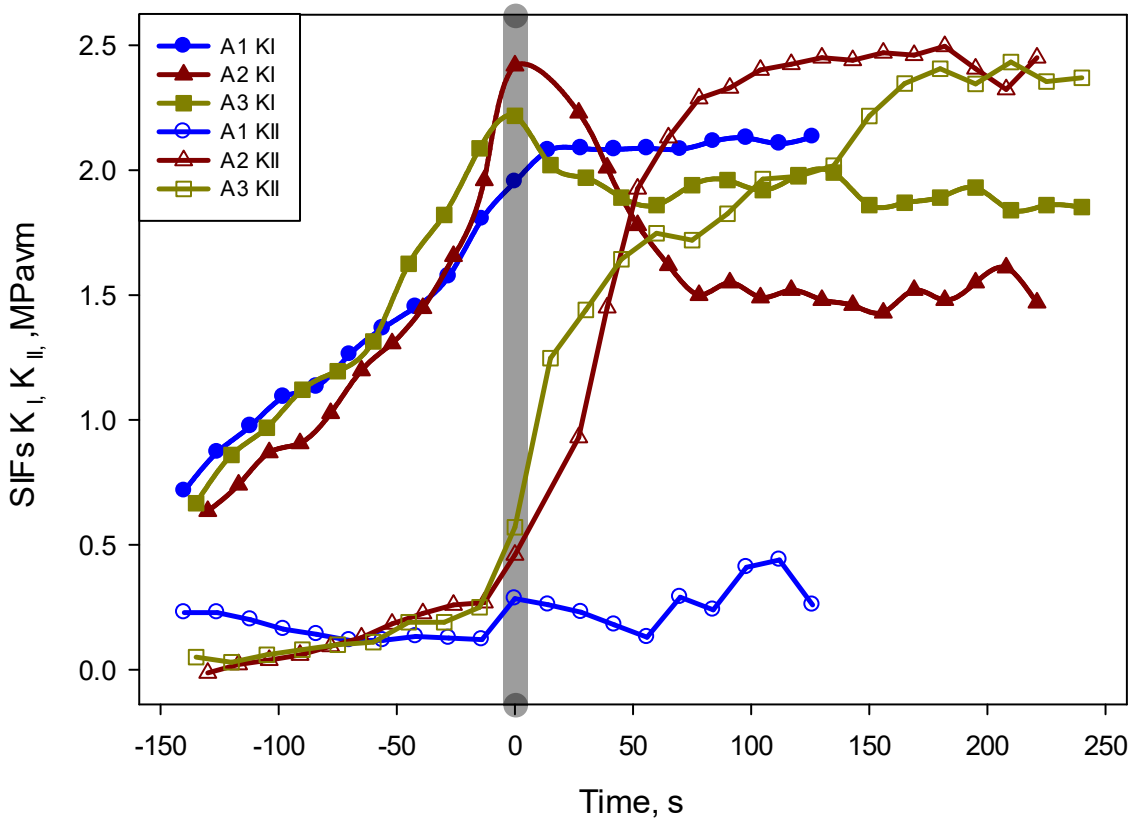

Figure 3.22: SIF histories for 3-point bend specimens of A1, A2 and A3 architectures under quasi-static loading conditions. (Negative and positive times correspond to pre- and post-crack initiation regimes.)

3.4 Discussion

As evident from the above description of results for the three print architectures A1, A2, and A3, the tension tests and fracture tests show a few unexpected behaviors. The elastic properties of all three print architectures measured using quasi-static tension tests on dog-bone specimens or using ultrasonic measurements, showed nominally identical values suggesting elastic isotropy at the macroscale. As to be expected, the ultrasonic measurements yielded higher elastic moduli (2.6-

2.7 GPa) when compared to the quasi-static counterparts (2.05-2.15 GPa). The tension tests revealed that the print architectures affect the ultimate stress only marginally; the A1 architecture was found to be the weakest relative to the other two. Print architecture, however, influenced ductility the most. The strain at failure measurements showed substantial differences; ~2.5% for A1, ~9% for A2 and unexpectedly higher value of ~11% for A3.

The quasi-static crack initiation toughness (or the critical SIF) values for A1 and A2 were the lowest (~2.0 MPa√m) and the highest (~2.5 MPa√m), respectively, with an intermediate value for A3 (~2.3 MPa√m). In the quasi-static case, although A2 showed the highest critical SIF, A3 produced a graceful or a gradual failure behavior ($dJ/da > 0$) with higher resistance to crack growth in terms of the measured *J*-integral.

Some insight into unexpectedly higher ductility of A3 relative to A2 and A1 could be gained from uniaxial tension tests on different unidirectional reference architectures. The results are shown in Figure 3.11. Figure 3.11(a) and (b) shows the tensile stress-strain responses. The results (peak stress ~35 MPa for 0^o print and ~40 MPa for the 90^o print, strain-at-failure ~2.4% in both cases) are nearly same as the one for the A1 (Figure 3.12) architecture. The pure shear tests (Figure 3.11(c)), on the other hand, show that the ultimate shear stress is ~35 MPa, close to the tensile strength of the unidirectional coupons. However, the shear strain at failure is ~23%, ten times higher than the tensile failure strain of the 0^o or 90^o print (and the A1 architecture). This suggests that ductility of a printed architecture can be influenced favorably by forcing the failure to occur in shear instead of tension.

Despite these results, the fact that ductility of A3 is greater than that for A2 suggests additional mechanisms at play. The synergistic constraint effects of different print directions are likely contributors in this regard. For example, Jhaver and Tippur [68] observed an increased

plateau stress during compression of a hybrid co-continuous (interpenetrating) foam material made of closed-cell polymer foam infiltrated into an aluminum open-cell foam scaffold. Their hybrid foam showed ~50% higher plateau stress and 35% higher energy absorption per unit mass relative to the syntactic foam and it was attributed to synergistic constraint effects. The $[0/45/90/-45^{o}]_{n}$ layering in A3 architecture is expected to perform a similar function. That is, the 90° print layer mitigates the tensile stress on the 45° and -45° layers accommodating higher shear deformations to occur.

The tensile tests can also shed light on the observed fracture characteristics of the three architectures. The low crack initiation toughness followed by growth at a stable *J*-integral value for A1 is consistent with the low ductility observed in $[0^{o}]_{n}$ and $[90^{o}]_{n}$ coupons (Figure 3.11). Relatively high crack initiation toughness followed by unstable crack growth along one of the two 45° directions in A2 is also consistent with the higher shear strain at failure in the Iosipescu sample as the crack kinks into a 45° plane and endures combined tensile and shear deformations. The back and forth switching between +45° and -45° planes also suggests the possibility of a jagged, instead of a straight, crack front and hence smeared deformations relative to A1. These failure mechanisms are further amplified in the A3 architecture with the crack front having opportunities for ±45° as well as 0° growth along the weaker planes between the individual printed beads/strings and a macroscale growth in a direction not necessarily along ±45°.

Chapter 4. High Strain Rate Fracture

In this chapter, details pertaining to experiments carried out to evaluate the mechanical and fracture properties under high strain rate loading are provided. Ultrasonic tests and fracture tests were performed on the three architectures to evaluate the elastic constants and energy release rate under high strain rate loading, respectively. The experimental details are provided first, followed by their results and a discussion of results. Fractographic information on different print architectures is also included.

4.1 Specimen Preparation

Specimens in all three architectures were printed as per the procedure outlined in section 3.1. The same printer with identical print parameters were used to craft the specimens so that it aids us in our pursuit of evaluating the strain rate sensitivity of AM ABS. Specimen geometry for each of the experiments are specified in the corresponding sections below.

4.2 Experimental details

4.2.1 Ultrasonic measurements

Ultrasonic measurements were performed on 12.7 mm ABS cubes printed in A1, A2 and A3 architectures. An ultrasonic tester, Olympus Epoch 600, was used for launching elastic waves into the specimen in all three (x, y, z) directions and for all three print architectures. The elastic wave speeds for both longitudinal (C_L) and shear (C_S) waves were recorded along all the three axes. A schematic of the setup used in these measurements is shown in Figure 4.1. Longitudinal (2.25 MHz) and shear (5 MHz) wave transducers were employed separately to measure the time-of-flight using which the respective wave speeds were determined. These values along with

separately measured mass density (ρ) used in conjunction with the below equation resulted in *dynamic* elastic constants, E and v, for each print architecture. A photograph of the Olympus Epoch 600 used in recording the elastic waves is shown in Figure 4.2 along with the transducers and the cube specimen used for measurements. The time-of-flight was recorded using the through transmission mode, where two transducers were used. One transducer acted as a transmitter sending the elastic waves into the specimen and the other transducer acted as a receiver on the other end of the cube specimen.

$$C_L = \sqrt{\frac{E(1-v)}{\rho(1+v)(1-2v)}}, C_S = \sqrt{\frac{E}{2\rho(1+v)}} \tag{4.1}$$

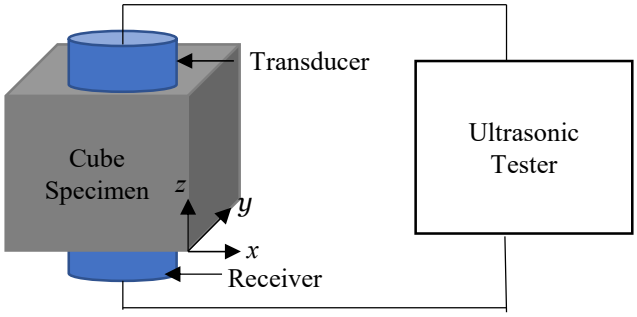

Figure 4.1: Ultrasonic test setup

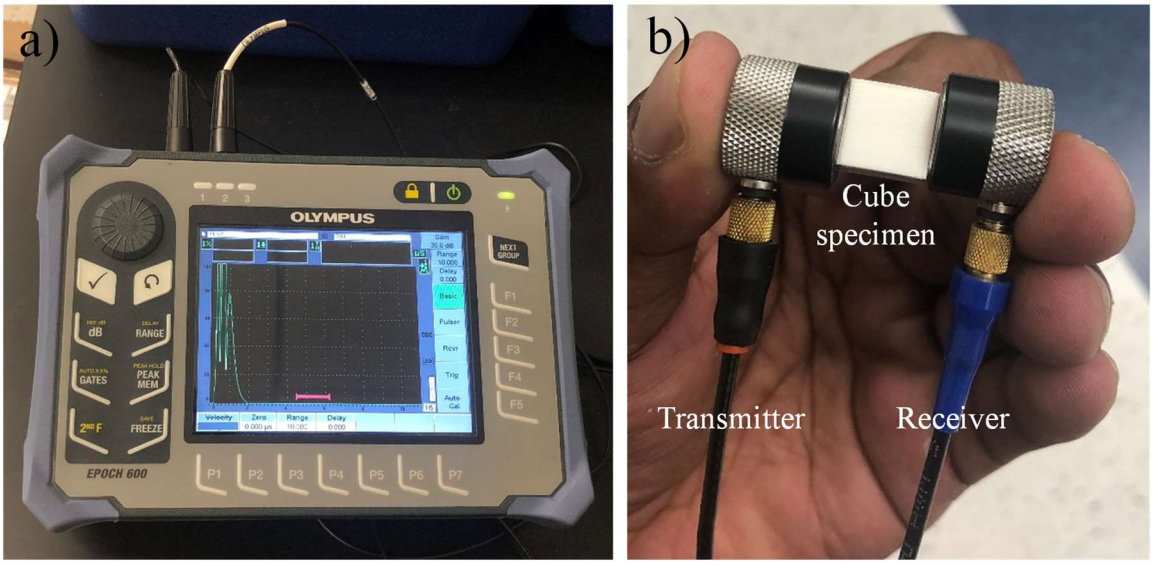

Figure 4.2: Ultrasonic test setup. (a) Olympus Epoch 600 and (b) transducers being employed in the through transmission mode.

4.2.2 Fracture tests

Impact induced fracture behavior of all the three print architectures was studied next. A modified Hopkinson pressure bar (or a long bar) apparatus was used for loading the specimens using stress waves [69, 70]. An ultrahigh-speed camera was used to perform time-resolved 2D-DIC measurements around dynamically loaded cracks. Figure 4.3 shows a schematic of the loading apparatus along with the arrangement for optical recording of speckles during the event. The long bar made of aluminum 7075-T6 was approx. 1.8 m long (72 inches) and 25.4 mm (1 inch) in diameter and was held in place by a couple of pillow blocks. An aluminum striker rod of length 317.5 mm (12.5 inches) and diameter 25.4 mm (1 inch) was propelled from the barrel of a gas-gun to impact the long-bar and generate stress waves. The other end of the long-bar had a wedge-shaped profile and was in contact with the specimen having a 40^{o} V-notch matching the loading tip of the long-bar. That is, the V-notch flanks of the specimen were pressed against the long-bar prior to the start of stress wave loading event. Figure 4.4 shows the dimensions of the

specimen along with the ROI captured by the camera during the fracture event. The specimen had a 3 mm long straight notch inserted into the specimen at the apex of the V-notch using a 300 μm thick circular saw and the notch-tip was sharpened using a razor blade as in the quasistatic fracture experiments. The specimen was placed over a 100 mm long strip of soft putty of ~3 mm thickness on a translation stage with another identical strip pressed on to the top edge for achieving symmetry in terms of acoustic impedance relative to the loading axis. A Kirana-05M ultrahigh-speed camera (924×768 pixels fitted with 70-300 mm focal length lens) was used to record dynamic deformations at a rate of 200,000 fps. In these experiments, a striker velocity of ~20 m/s was used for impact loading the specimens. A catcher box padded with thick sheets of foam was used to trap the failed specimens after impact. The pillow blocks holding the long bar assisted in arresting the motion of the bar after impact. Figure 4.5 shows a picture of part of the high strain rate test setup used in this work.

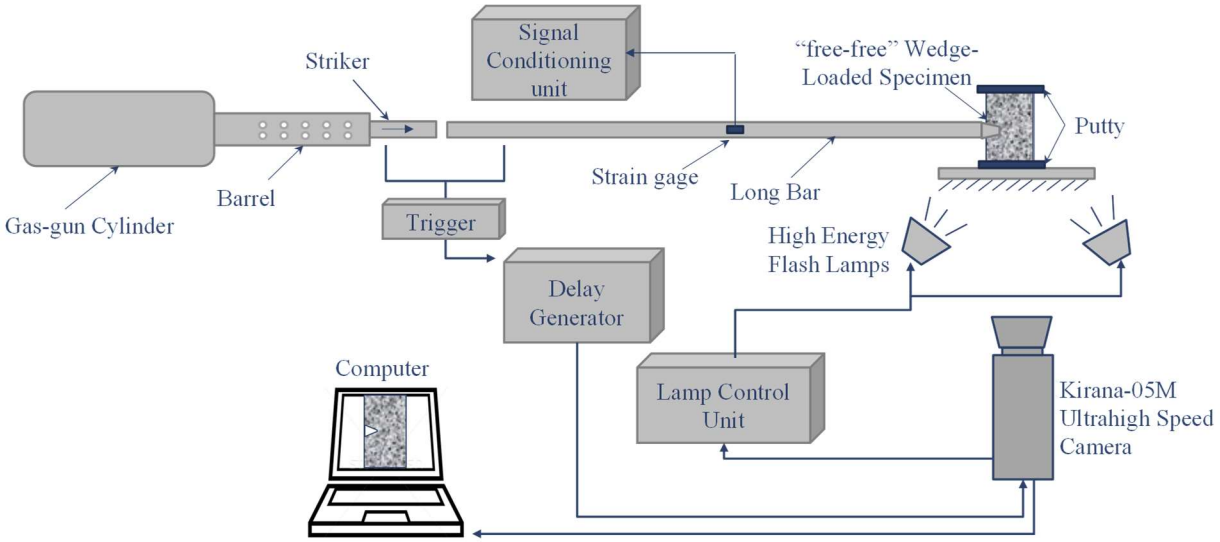

Figure 4.3: Schematic of experimental setup used for high strain fracture experiments.

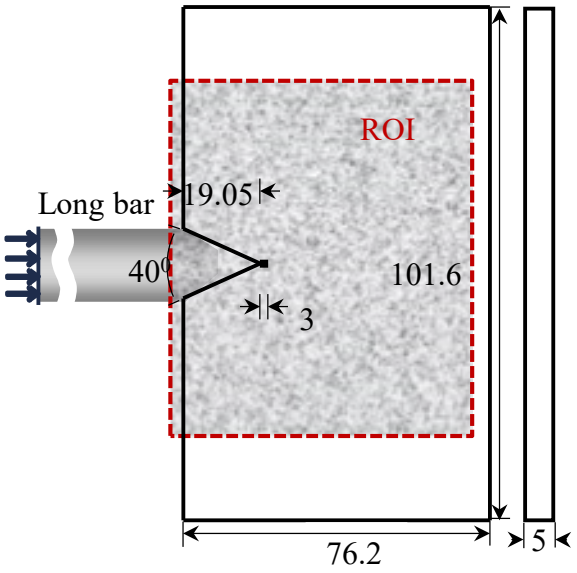

Figure 4.4: Dynamic fracture specimen loading and geometry. (All dimensions are in mm).

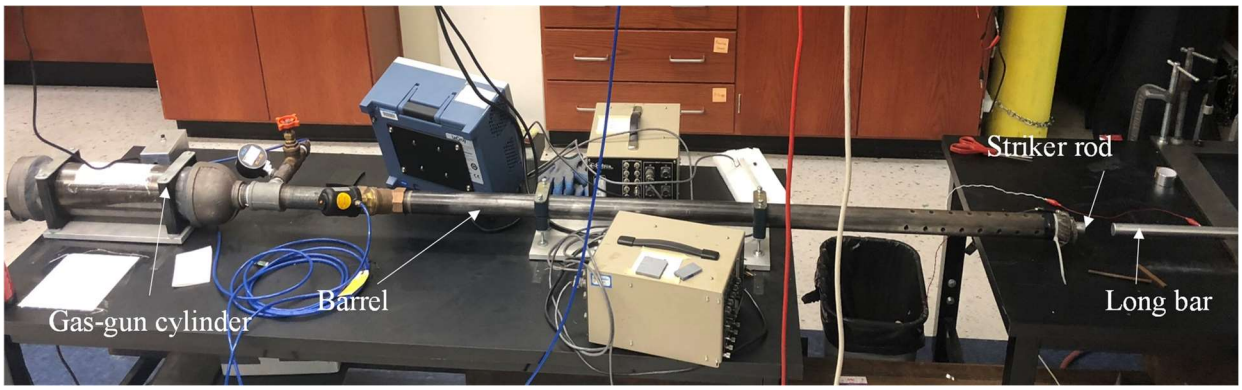

Figure 4.5: Modified Hopkinson pressure bar setup.

4.3 Results

4.3.1 Ultrasonic tests

The results obtained from the ultrasonic measurements are listed in Table 4.1. Evidently, the values of E are expectedly higher than the ones from uniaxial quasi-static tests due to the higher strain rates (MHz frequency) imposed by the ultrasonic transducer. More importantly, the values of these dynamic elastic constants were the same in all the three directions and for all three

architectures. Thus, the 3D printed architectures were *macroscopically isotropic* despite the differences in the underlying print architectures.

Table 4.1 –Ultrasonically measured wave speeds, density, and elastic constants for the three different print architectures in three orthogonal directions. (Density of bulk ABS based on manufacturer supplied wire stock was ~1035 Kg/m^3 and hence porosity based on weight difference was ~1.18%).

Print Architecture	Axis of Measurement	Longitudinal Wave speed C_L (m/s)	Shear Wave speed C_S (m/s)	Density ρ (Kg/m^3)	Poisson's Ratio ν	Elastic Modulus E (GPa)
A1	*x*	2045	987	1022	0.348	2.66
	y	2041	986		0.348	2.65
	z	2035	983		0.348	2.63
A2	*x*	2041	984	1022	0.349	2.67
	y	2038	986		0.347	2.67
	z	2061	988		0.351	2.69
A3	*x*	2060	988	1022	0.348	2.67
	y	2058	987		0.347	2.68
	z	2061	985		0.349	2.68

4.3.2 Fracture tests

As described previously, the V-notched specimens were dynamically loaded by impacting the long-bar and the resulting transient fracture event in the specimen was imaged using an ultrahigh-speed camera. To accomplish the optical mapping of deformations in the ROI, the specimens were spray painted with black/white random speckles and were photographed during the stress wave loading event using a Kirana 05M (924×768 pixels) single sensor camera at a framing rate of 200,000 fps (or inter frame rate/sampling of 5 μs). The images in the deformed

state were correlated with the one in the reference/undeformed state recorded before the start of the impact event. As in the quasi-static counterparts, the speckle image correlation was performed using ARAMIS® software. During the analysis, as in quasistatic counterparts, each image was segmented into sub-images of size 25×25 and an overlap of 5 pixels. The scale factor was ~60 μm/pixel for all dynamic fracture experiments. Thus, obtained orthogonal displacement fields were then used in conjunction with the analysis approach described earlier to extract the *J*-integral.

Figure 4.6, Figure 4.7, and Figure 4.8 show select displacement contours and speckle images for all the three print architectures A1, A2 and A3, respectively. The speckle images and displacement components u and v in the x- and y-directions in the pre- and post-initiation states are shown in Figure 4.6 for A1. The u-fields are symmetric relative to the crack and the (horizontal) loading axis. The v-contours, on the other hand, are symmetric in shape and antisymmetric in magnitude relative to the crack. This is consistent with the mode-I deformations in the pre- and post-initiation regimes in the A1 architecture. The region, from which the *J*-Integral values are averaged, are highlighted in one of the speckle images in Figure 4.6(a).

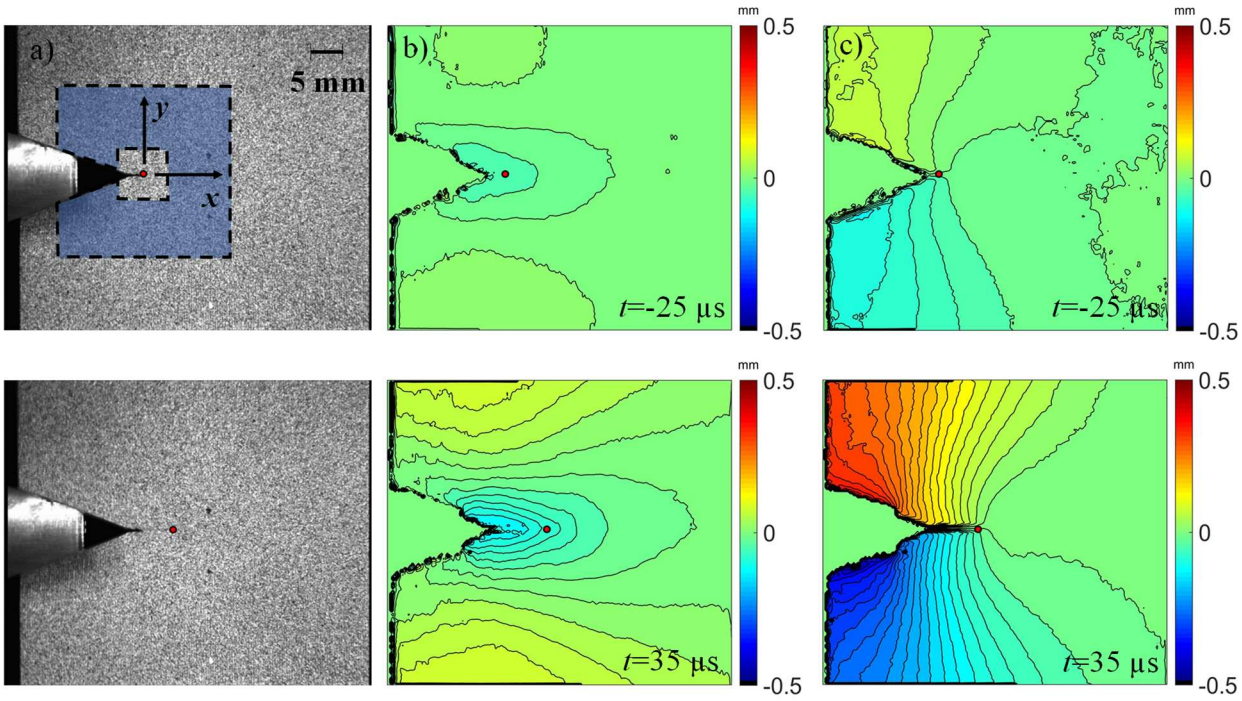

Figure 4.6: Measured displacement contours for A1 at two time instants before and after crack initiation. Contour interval = 10 µm. (a) Speckle images at a particular time step and their corresponding (b) *x*- or *u*-field, and (c) *y*-or *v*-field. Red solid dots indicate the crack tip at this time step.

The *u*- and *v*-fields along with the speckle images for the A2 architecture are shown in Figure 4.7 in both the pre- and post-initiation phases. As in the A1 architecture, the *u*-contours are again symmetric whereas the *v*-contours are symmetric only in shape and antisymmetric in values relative to the initial crack orientation before initiation suggesting a dominant mode-I deformation. Once the crack initiates, however, the propagation occurs in one of the two print directions, along -45º in this case. As a result, the local *u*- and *v*-deformation contours are asymmetric relative to the initial and current crack orientations and hence occurrence of mixed-mode (mode-I and -II) fracture.

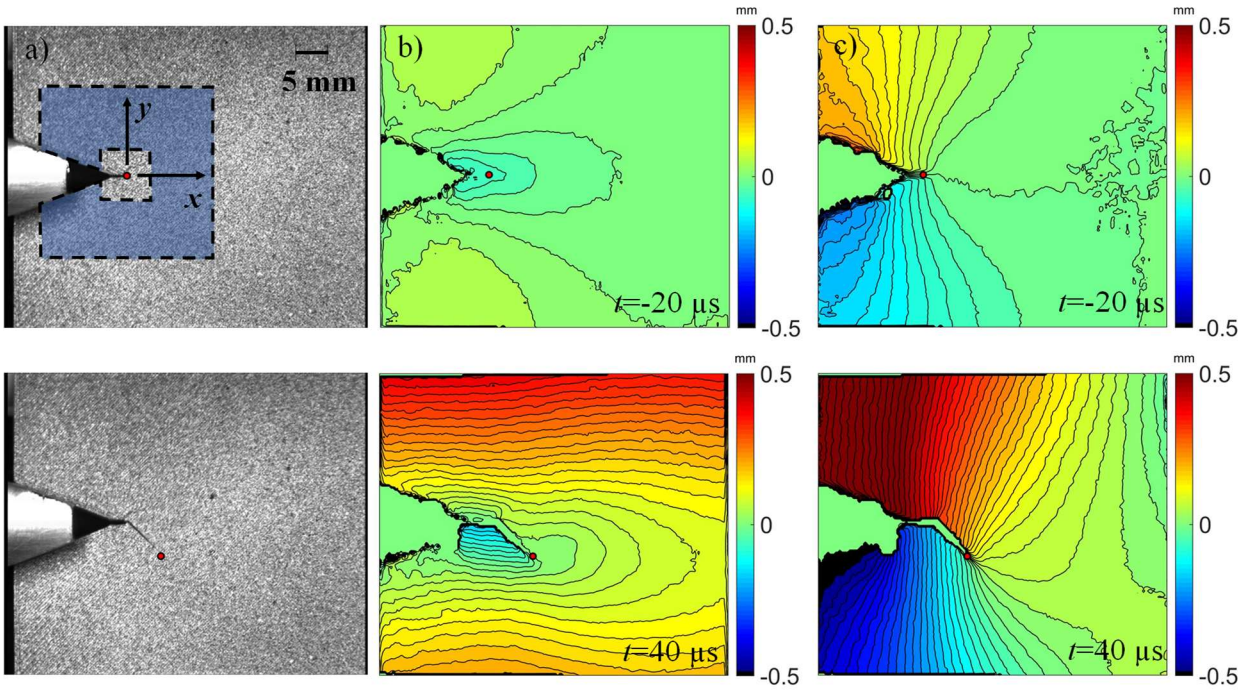

Figure 4.7: Measured displacement contours for A2 at two time instants before and after crack initiation. Contour interval = 10 μm. (a) Speckle images at a particular time step and their corresponding (b) *x*- or *u*-field, and (c) *y*-or *v*-field. Red solid dots indicate the crack tip at this time step.

The *u*- and *v*-contours and the speckle images for A3 are shown in Figure 4.8. As in the A2 architecture, the displacement contours are symmetric in shape prior to crack initiation, consistent with mode-I deformations. Upon crack initiation, however, growth occurred in this architecture along ±45º as shown. That is, as in the quasi-static counterparts, the crack growth occurred in a mixed-mode fashion with locally asymmetric deformations.

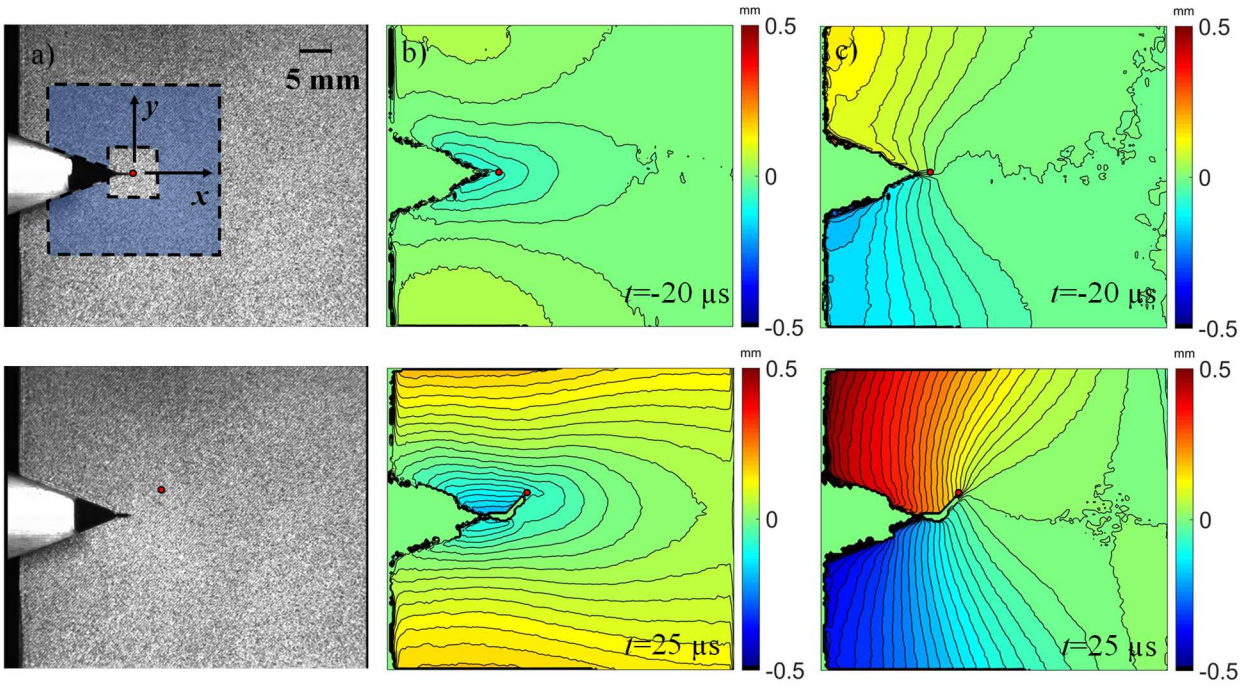

Figure 4.8: Measured displacement contours for A3 at two time instants before and after crack initiation. Contour interval = 10 µm. (a) Speckle images at a particular time step and their corresponding (b) *x*- or *u*-field, and (c) *y*-or *v*-field. Red solid dots indicate the crack tip at this time step.

However, unlike the quasi-static counterpart in which a zig-zag growth of different lengths in 0º or ±45º resulted in a macroscale growth angle different from the 45º, the crack growth here occurred in a distinct 45º direction. In this architecture with an equal opportunity for the crack to propagate in the 0º or ±45º direction, the growth consistently occurred in one of the two possible 45º directions. Figure 4.9 shows photographs of fractured specimens of all three architectures under dynamic conditions.

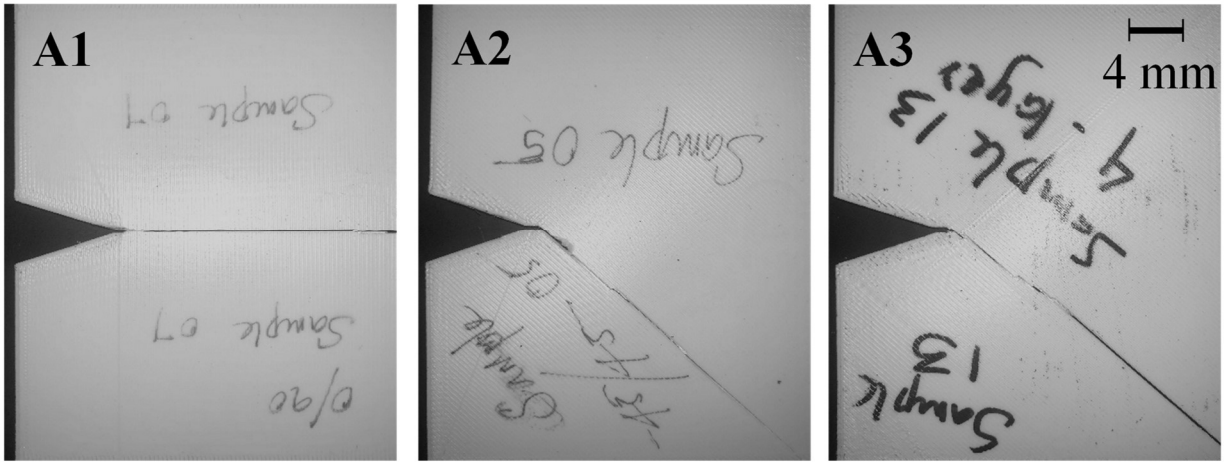

Figure 4.9: Dynamic crack paths observed in V-notched specimens.

The crack length histories, obtained by inspecting the speckle images and the location where displacement contours from DIC converge, are plotted in Figure 4.10. The crack growth was monotonic in all three print architectures. Also, the rates of crack growth were found to be low in all architectures. That is, they were in the range of 30-60 m/s during the observation window. These speeds are quite low (~5%) relative to the shear wave speeds (~980 m/s) (see, Table 4.1). *Hence, it is reasonable to adopt the J-integral evaluation procedures as discussed earlier even though strictly they are not applicable to stress wave dominant conditions.* For example, if the crack were propagating, say, at 30-40% of the shear wave speed of the material as it often does in brittle epoxies, acrylics and polyesters subjected to dynamic loading this approach would not be appropriate.

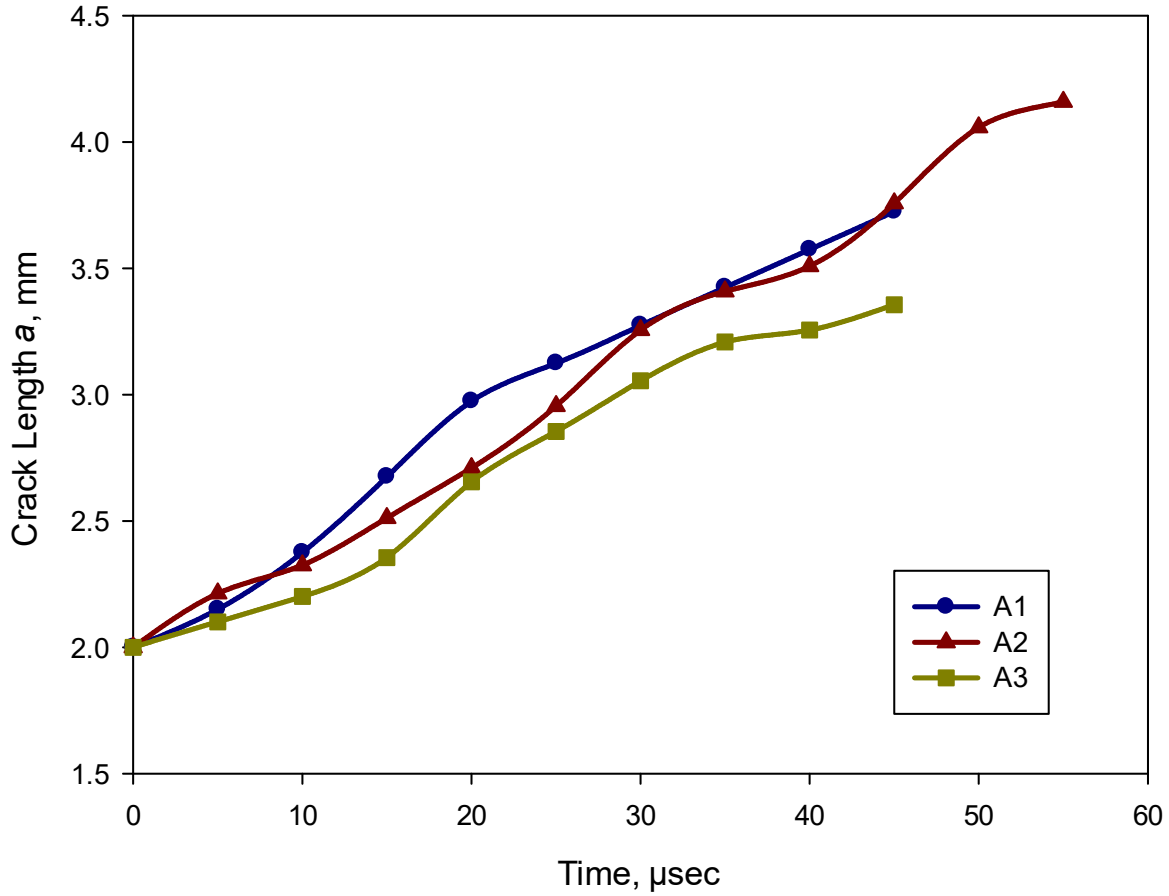

Figure 4.10: Crack length histories for V-notched specimens subjected to dynamic loading. The crack velocities are low and in the 30-60 m/sec range; shear wave speed in this material is ~980 m/sec

Figure 4.11 shows the crack growth resistance curves for the three print architectures under dynamic loading conditions. Under dynamic conditions *J*-integral vs. velocity plot is more appropriate. However, due to very low crack speeds observed, the crack growth resistance as *J*-integral vs. crack length is reasonable and inertia effects are accounted for. The crack growth resistance in terms of the *J*-integral after crack initiation, at approx. 2300 N/m, shows an unstable crack growth event relative to the value at crack initiation for A1 as $dJ/da < 0$. This is unlike in quasi-static counterpart (Figure 3.18). In case of A2, the values of the *J*-integral drop noticeably right after crack initiation at ~4000 N/m before building back to a steady state value of 3800 N/m.

Unstable crack growth event at crack initiation is observed for this architecture. In case of A3, however, the crack growth resistance in terms of the *J*-integral initially shows $dJ/da > 0$ after initiation at ~3600 N/m followed by increase to a nearly constant value of 4000 N/m later in the observation window. Given these differences among the three architectures, A3 again stands out in terms of a graceful crack growth behavior relative to the other two even though A2 had a slightly higher value at crack initiation.

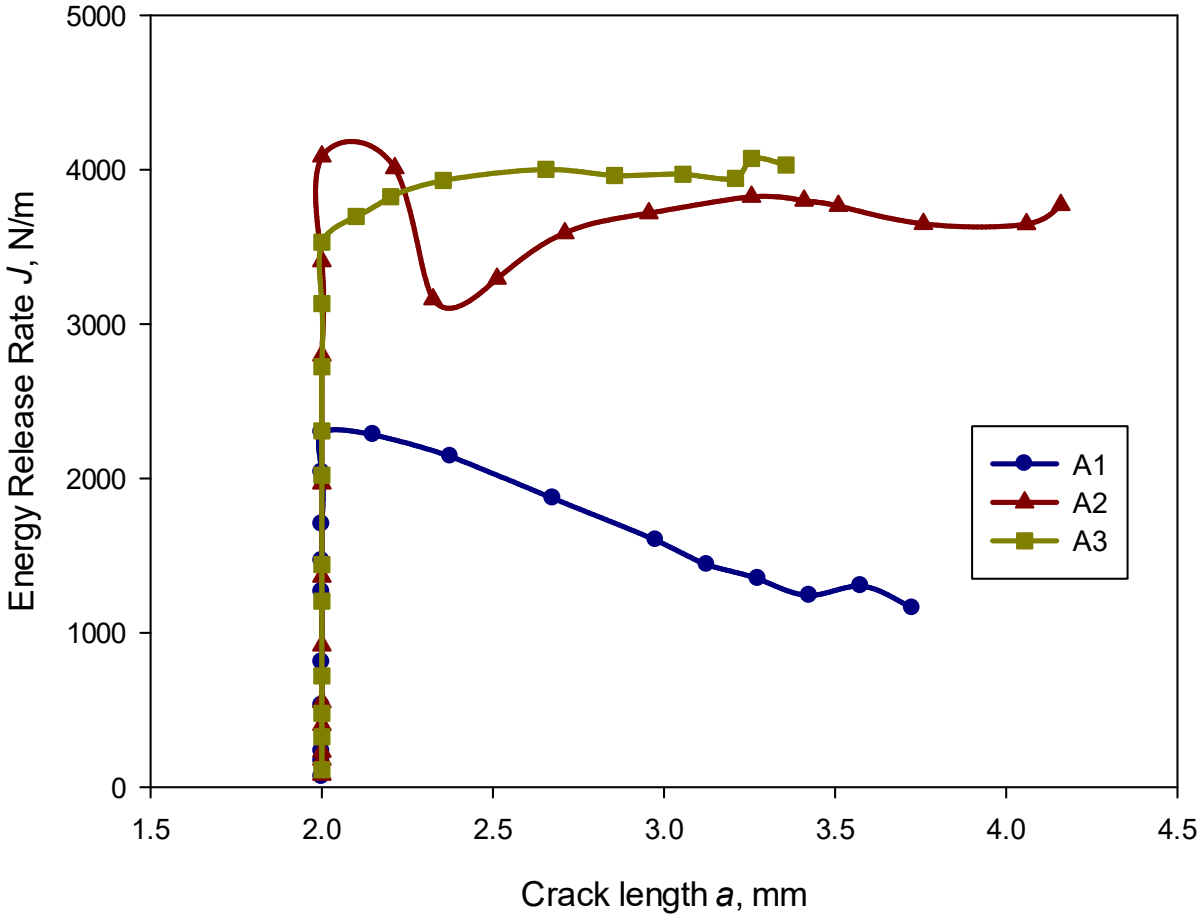

Figure 4.11: Crack growth resistance curves for V-notched specimens under dynamic conditions

Figure 4.12 shows the histories of the *J*-integral for all three cases under dynamic loading conditions. For the purpose of comparing the fracture behaviors, the time axes for each case are

shifted such that $t = 0$ corresponds to crack initiation. That is, the negative and positive t values correspond to pre- and post-initiation regimes, respectively. The resistance to crack growth continuously dropped after crack initiation (at $t = 0$) in the print architecture A1 whereas it attained higher stable values in the A2 and A3 architectures. Other aspects of crack growth behavior align well with the description provided for Figure 4.11.

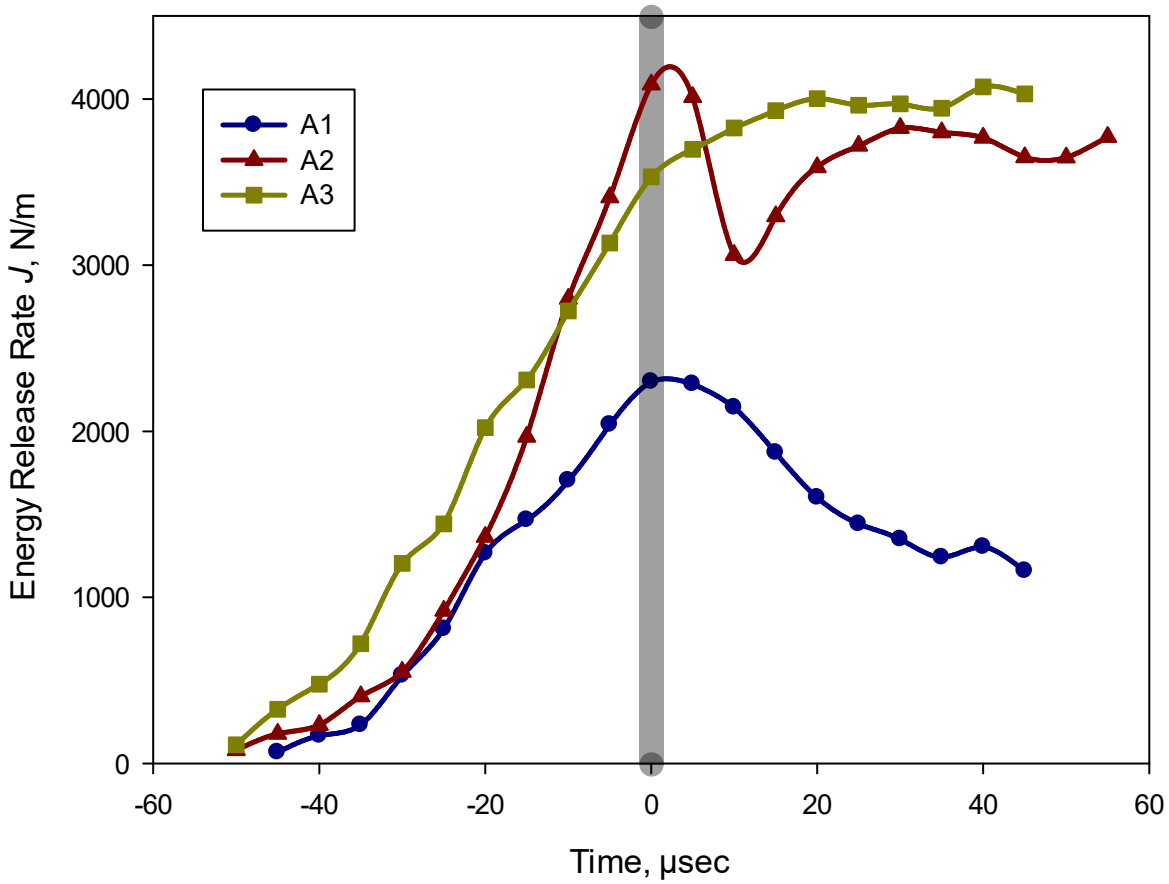

Figure 4.12: The *J*-Integral histories for edge-notched specimens under dynamic loading condition. Negative and positive times correspond to pre- and post-crack initiation regimes.

Figure 4.13 shows plots of mode partitioned SIF histories for the three architectures. A monotonic increase in the K_I values was observed until crack initiation for each of the three architectures. Similar to the quasi-static results, the A2 architecture had the highest crack initiation

toughness of approx. 2.9 MPa√m followed by 2.7 MPa√m for A3 and then 2.2 MPa√m for A1 architectures. In case of A1, the K_I values dropped significantly after crack initiation while the K_{II} values remained nearly zero as mode-I failure ensued in this architecture. The A2 architecture showed a similar drop in the K_I values after crack initiation whereas K_{II} value increased rapidly as the crack kinked into one of the 45^o paths before attaining a steady state. In the A3 case also, after crack initiation, the K_I values dropped while the K_{II} values increased. Furthermore, the mode-II SIF histories of A2 and A3 architectures exhibited similar tracks as the crack growth occurred in the latter along a dominant 45^o path. Within the measurement errors, the mode-I SIF histories of each of the architectures follow a similar path in the post-initiation regime although the architecture A3 is consistently higher than the A2 counterpart.

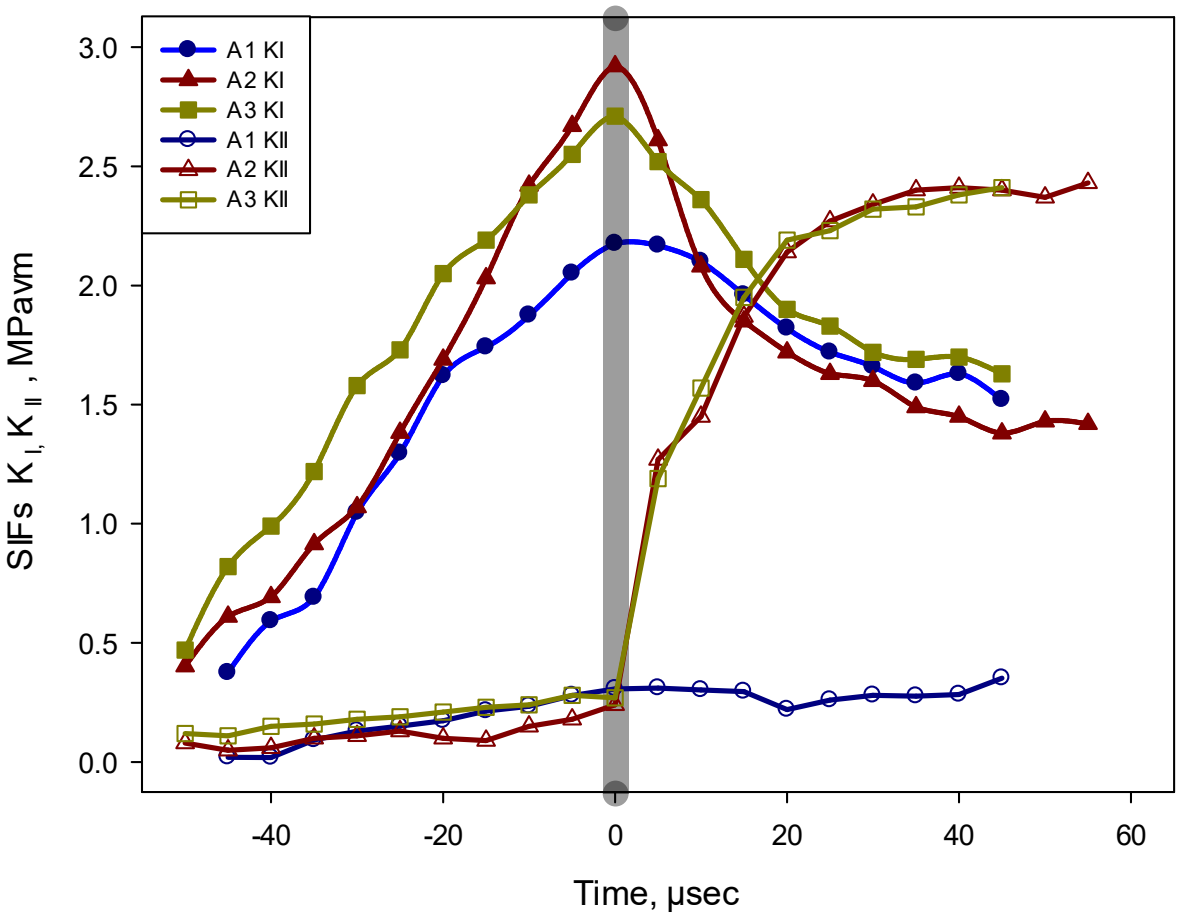

Figure 4.13: SIF histories of edge-notched specimens under dynamic conditions. (Negative and positive times correspond to pre- and post-crack initiation regimes.)

4.4 Discussion

The elastic properties of all three print architectures under high strain rate testing conditions did not show notable differences suggesting elastic isotropy at the macroscale. As expected, the ultrasonic measurements yielded higher elastic moduli (2.6-2.7 GPa) when compared to the quasi-static counterparts (2.05-2.15 GPa) due to the strain-rate sensitivity of the ABS.

Table 4.2 – The *J*-integral values at crack initiation under static and dynamic conditions.

Critical Energy Release Rate J_{cr}, N/m	**A1**	**A2**	**A3**
Quasi-Static	1850	2900	2500
Dynamic	2300	4000	3600

From Table 4.2, A2 had the highest crack initiation toughness under both static and dynamic conditions whereas A1 was the lowest among the three architectures. In the quasi-static case, although A2 showed the highest toughness at initiation, A3 had a rather gradual/graceful failure behavior with increasing resistance to crack growth ($dJ/da > 0$). Furthermore, the measured energy release rate was the highest for A3. In the dynamic case, both A2 and A3 architectures showed a kinked crack growth along one of the 45° planes after crack initiation with A2 presenting a higher crack initiation toughness relative to A3 whereas A3 showed a stable crack growth leading to higher values of the *J*-integral relative to A2.

Under dynamic loading conditions, the failure mechanisms observed in quasi-static fracture tests did not manifest fully due to temporal constraints. For example, both A2 and A3 architectures produce fracture along a dominant 45° path with a somewhat higher degree of meandering of the crack in the latter relative to the former (Figure 4.9). Additionally, an unstable crack growth behavior in terms of the rate of change of the *J*-integral was rather pronounced in both A1 and A2 architectures. Furthermore, given equal opportunities for the crack to grow in the 0° or 45° directions, the crack growth in a 45° path confirms lower failure strain in the normal direction relative to failure strain in shear.

Chapter 5. Mixed-Mode (I/II) Fracture

In this chapter, mixed-mode fracture behavior of AM ABS under quasi-static loading conditions is described. An Arcan loading fixture is designed to facilitate mixed-mode loading of specimens. The DIC methodology was concurrently employed to directly evaluate the SIFs for the three architectures under different loading configurations ranging from mode-I to dominant mode-II condition with the help of hybrid DIC-FE approach. The experimental details are provided first, followed by results and discussion of the outcome. Fractographic information on different print architectures is also included to explain the underlying mechanics.

5.1 Specimen preparation

Specimens in all three architectures A1, A2 and A3 were printed as per the procedure outlined in section 3.1. The same 3D printer with identical print parameters were used to manufacture the specimens so that the quasi-static fracture results from mode-I three-point bend experiments and mixed-mode (I/II) Arcan experiments remain comparable. Details of the specimen geometry used with the Arcan loading fixture are provided in the experimental details section.

5.2 Mixed-mode (I/II) loading fixtures

Over the years, different loading configurations and fixtures have been used for performing mixed-mode fracture experiments. Some of the common methods include eccentric three-point bending [71-74], asymmetric four-point bending [75-77], semi-circular beam bending [78-82], tensile loading on a slant edge cracked specimen [83, 84], Brazilian disk compression test [85, 86], Arcan loading fixture [38-40, 87-89], etc. Achieving pure mode-II crack tip loading and the feasibility to optically measure displacements around its vicinity on the specimen surface being the requirements of most testing protocols, test fixtures such as eccentric three-point bending and

asymmetric four-point bending are not often practical. For example, to achieve dominant mode-II loading in eccentric three-point bending and asymmetric four-point bending, the initial crack location will have to be very close to the support pins causing severe interaction between the crack tip stresses and stress concentration due to the pin. In the case of tensile specimens with slant edge cracks, achieving dominant mode-II condition requires that the angle of the crack be very large relative to the loading direction. This in turn requires the crack tip very close to the free edges of the specimen. In such cases the crack tip displacements will be affected by the free edges, making extraction of fracture parameters rather difficult. Also, with the rastering of layers in other three print architectures, for example the semi-circular beam bending geometry, require reorientation of rastering relative to the crack orientation, adding to the complexity of the problem on hand. Despite these difficulties, asymmetric four-point bending and semi-circular beam bending were attempted during this work to achieve mixed-mode and dominant mode-II loading of the crack. However, because of significant plastic deformation at the supports during loading, the specimens invariably slipped away from the supports before the crack could initiate. Thus, experiments failed to fracture the AM ABS specimen under dominant shear/mode-II loading condition. Subsequently, tensile loading of a specimen with an inclined edge cracked specimen was attempted and fracture was achieved under significant mode-II conditions. However, as noted above, the crack had to be almost parallel to the edge of the specimen to achieve large mode-II contribution. Hence, considering that AM ABS specimens were able to fracture under tensile configuration, an Arcan fixture was preferred to load specimens over a wide range of mode-mixities ranging from mode-I to mode-II.

5.3 Experimental details

In this section, details on the development of Arcan loading fixture along with the specimen geometry and the experimental specifics are provided.

5.3.1 Fracture tests

Mixed-mode fracture tests were performed on an Instron 4465 mechanical tester equipped with a 5 kN load cell and an in-house Arcan loading fixture developed for the task. All fracture tests were carried out at a crosshead speed of 0.05 mm/s until fracture. Load, crosshead displacement, and time were all recorded at a rate of 0.1 Hz. The Arcan fixture was originally developed to create a uniform state of plane stress in solid specimens and the setup was primarily suited for mixed-mode testing (axial tension or compression + in-plane shear) of materials. To achieve this, semi-circular Arcan plates that can be attached to the loading frame and the load-cell (fixed to the crosshead) of the mechanical tester were designed. The geometry of the Arcan plates developed for the work and the intermediate connector to attach the plates to the load cell are shown in Figure 5.1(a) and Figure 5.1(b), respectively. The 12.7 mm diameter holes in the plates were spaced at 15° intervals with respect to the center of the semicircle and the 5 mm diameter holes were spaced at a vertical distance of 12.7 mm. The semi-circular Arcan plates were manufactured through waterjet machining from a rectangular plate. A specimen geometry to be tested with these plates that allows a relatively large region of interest (ROI) to be photographed to employ DIC was conceived. The dimensions of the Arcan specimen geometry used in this study are shown in Figure 5.2. The specimens had a crack length to specimen width $(a\ /\ W)$ ratio of 0.5. A fine coat of speckle pattern was applied on one of the specimen surfaces and the speckle pattern on the specimen surface was captured by a PointGrey camera at 2 fps during tests. The ROI for performing DIC is highlighted in Figure 5.2. It is worth noting that there are multiple reports on

Arcan fixtures that provide experimental SIFs estimated from the failure loads combined with correction factors obtained via complementary finite element analyses are available in the literature [87, 90-93]. However, none of them allow for photographing the specimen, especially the region around the crack as the Arcan plates generally obstruct the region around the crack tip on the specimen required for performing detailed optical measurements. The objective in this study was to make optical measurements on the specimen surface and extract fracture properties to understand the details of the mixed-mode fracture behavior. Hence, a new Arcan design which allows recording the specimen surface and the region around the crack tip was favored.

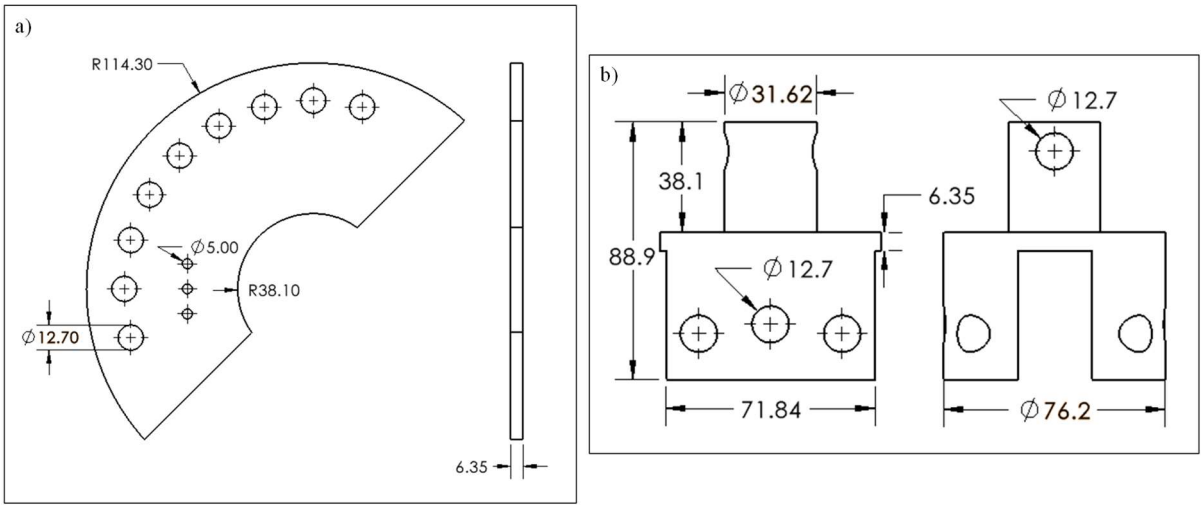

Figure 5.1: Dimensions of the (a) semi-circular Arcan plates and (b) the grips to connect them to the load cell. (*All dimensions are in mm*)

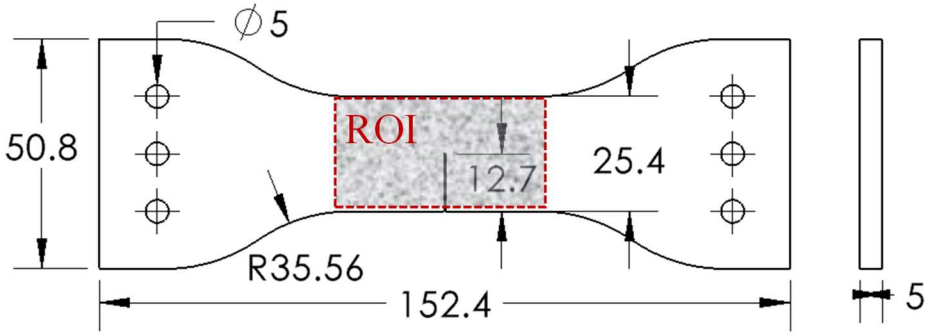

Figure 5.2: Arcan specimen geometry. (All dimensions are in mm)

To further explain the loading setup, the schematic of the Arcan fixture with the semi-circular plates and the specimen at a loading angle (α) of 45° is shown in Figure 5.3. The two pairs of Arcan plates, two loading grips and dowel pins were made of 17-4 PH stainless steel, 6061 aluminum, and polished 4140 alloy steel, respectively. The specimen was sandwiched between a pair of Arcan plates on each end and they were kept in contact with the specimen. Dowel pins were used to connect the loading grip to the Arcan plates as well. The top loading grip was connected to the load-cell while the bottom grip was connected to the load frame of the mechanical tester. The Arcan plate can be fixed to the loading grip at seven different angles, and this provides a range of mode-mixities at the crack tip. To further show this schematically, the orientation of the specimen at each of the loading angles is shown in Figure 5.4. The loading angle (α) was defined as the angle between the loading axis and normal to the crack tip or the length of the specimen. Seven different angles (α = 0°, 15°, 30°, 45°, 60°, 75°, and 90°) provide a full range of mode-mixities starting from pure mode-I (α = 0°) to pure mode-II (α = 90°) loading.

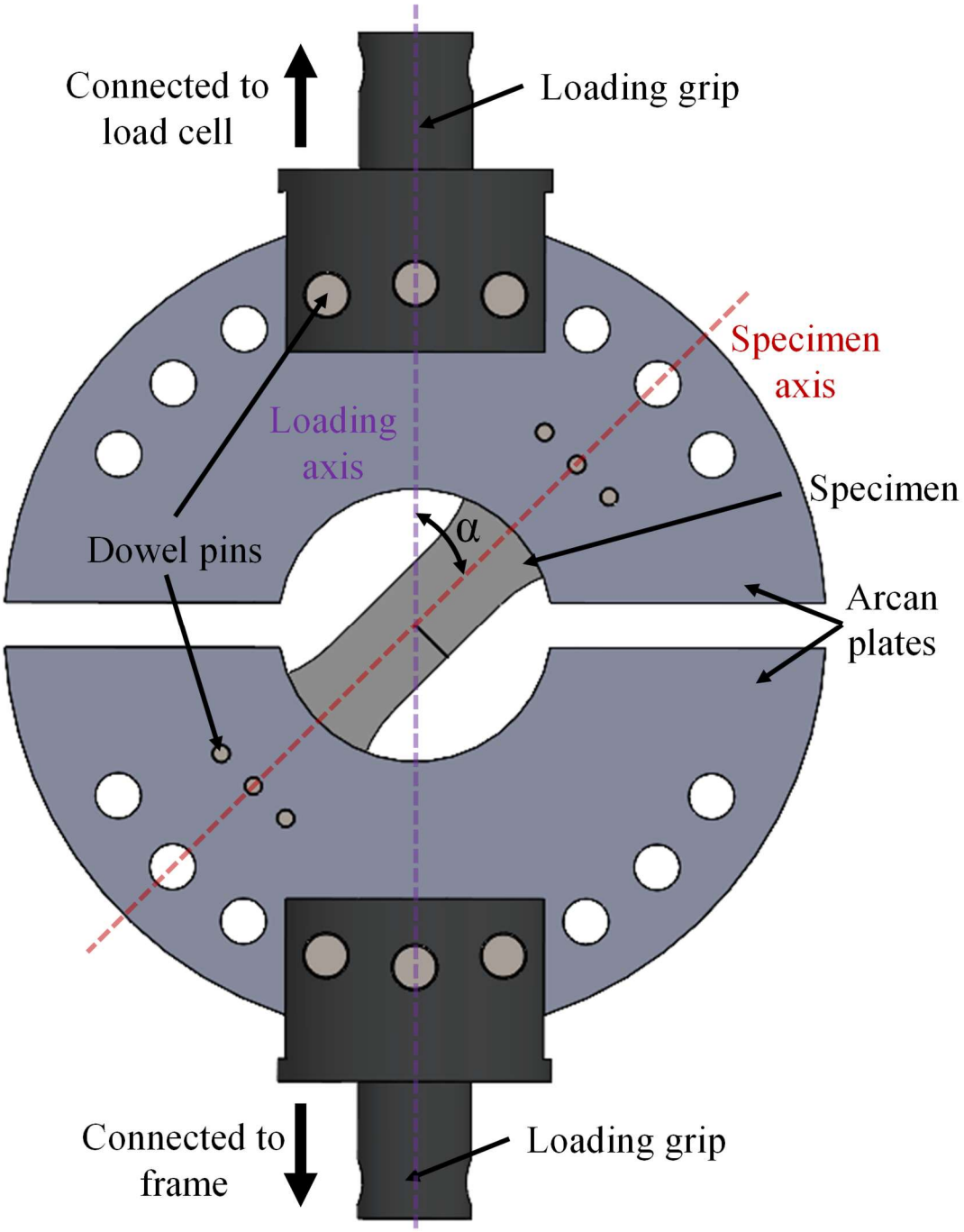

Figure 5.3: Schematic of the Arcan loading fixture (loading angle (α) = 45°). (All dimensions are in mm)

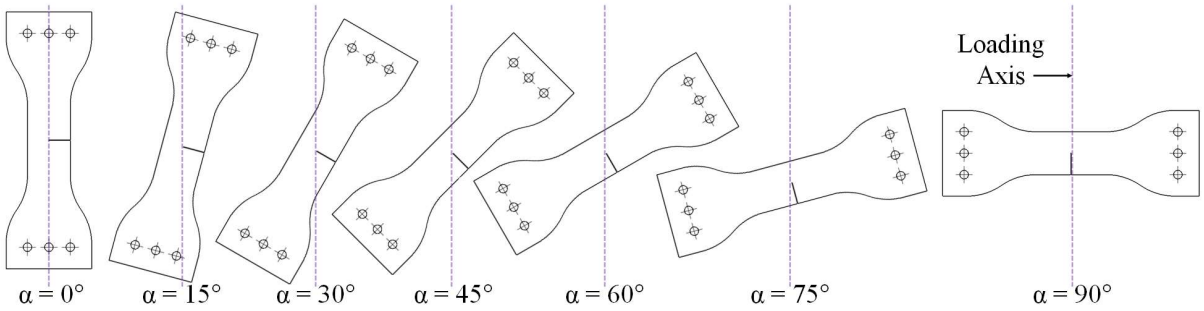

Figure 5.4: Orientation of Arcan specimen at seven different loading angles (α).

Pictures of the Arcan loading fixture at loading angles (α) of 0°, 15°, 30°, 45°, 60°, 75°, and 90° are shown in Figure 5.5. It can be noticed that the orientation of the specimen's connection to the Arcan plates do not change in different loading angles, it is only the Arcan plate's connection to the loading grip that determines the mixture of normal and shear force imposed at the crack tip of the specimen. The entire loading Arcan setup is shown in Figure 5.6.

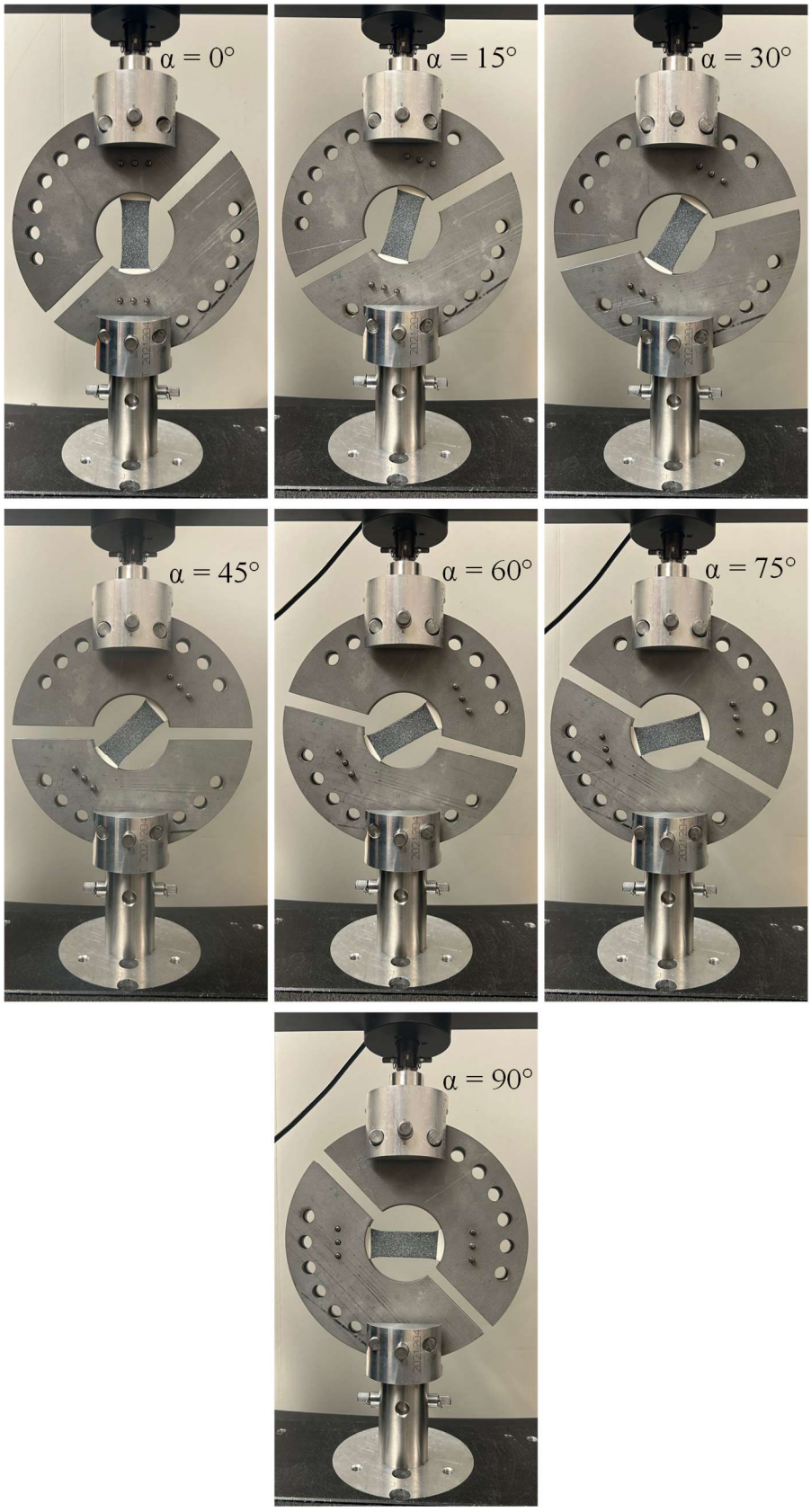

Figure 5.5: Arcan loading fixture at loading angles (α) of 0°, 15°, 30°, 45°, 60°, 75°, and 90°.

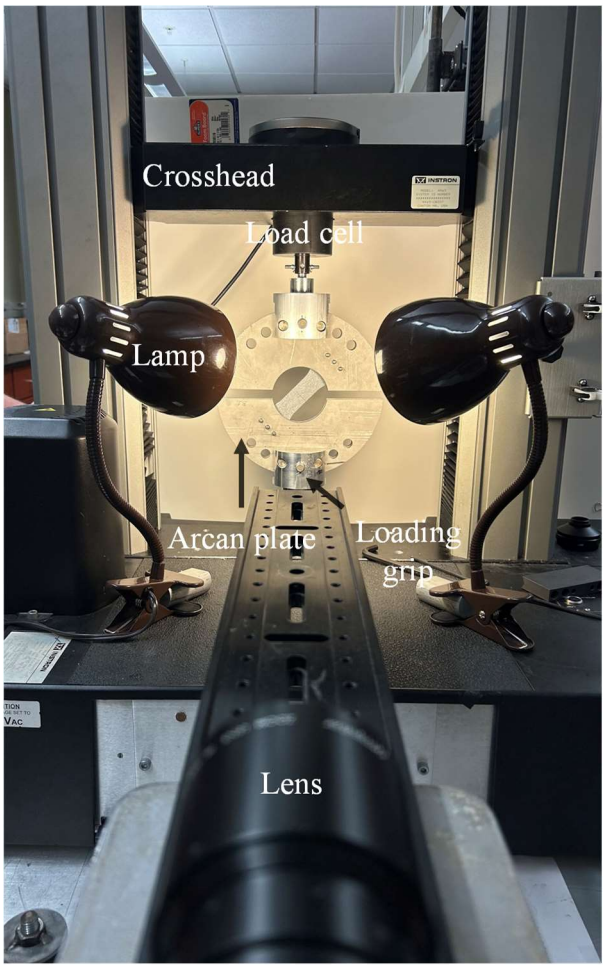

Figure 5.6: Arcan loading setup during optical measurements with a specimen at loading angle (α) of 45°.

5.3.2 Fractography

A Keyance VHX 6000 digital microscope was used to capture microscopic images of the fractured cross-sections of the Arcan specimens. Images of the crack path in all three print architectures under all the seven different mode-mixities were recorded using a digital camera to find the crack initiation angles and to further address the observed fracture responses.

5.4 Results

The load vs. load-point displacement curves for the Arcan specimen for the A1 architecture is shown in Figure 5.7. The loads at which the crack initiated in each case has been highlighted with an arrow. The A1 architecture had a linear response until crack initiation at the peak load when loading angles (α) were 0°and 15°. After crack initiation, a brittle failure, as evident by the sudden drop in load, was observed in both the cases. At α of 30°, an initial linear response was followed by a nonlinear response prior to the attainment of the peak load, again corresponding to crack initiation. Once the crack initiated, an abrupt crack growth was observed. At α of 45°, 60°, 75°, and 90°, significant nonlinearity was observed before the abrupt failure at the peak load. The nonlinearity followed an initial linear response of load was seen in all the cases. Considering the peak loads at different loading angles, the peak load increased when α increased from 0° to 30°. However, the peak loads dropped as α increased from 30° to 75°. The peak load remained almost the same at α = 75° and 90° with the response for 90° having a higher load-point displacement at failure. The load-point displacement at failure increased consistently as α increased from 0° to 90°. Also, as α changed from 0° to 90° (as the nature of loading changed from mode-I to mode-II), a drop in the stiffness (initial slope of load vs. deflection response) of the fracture responses was observed with increase in mode-II loading.

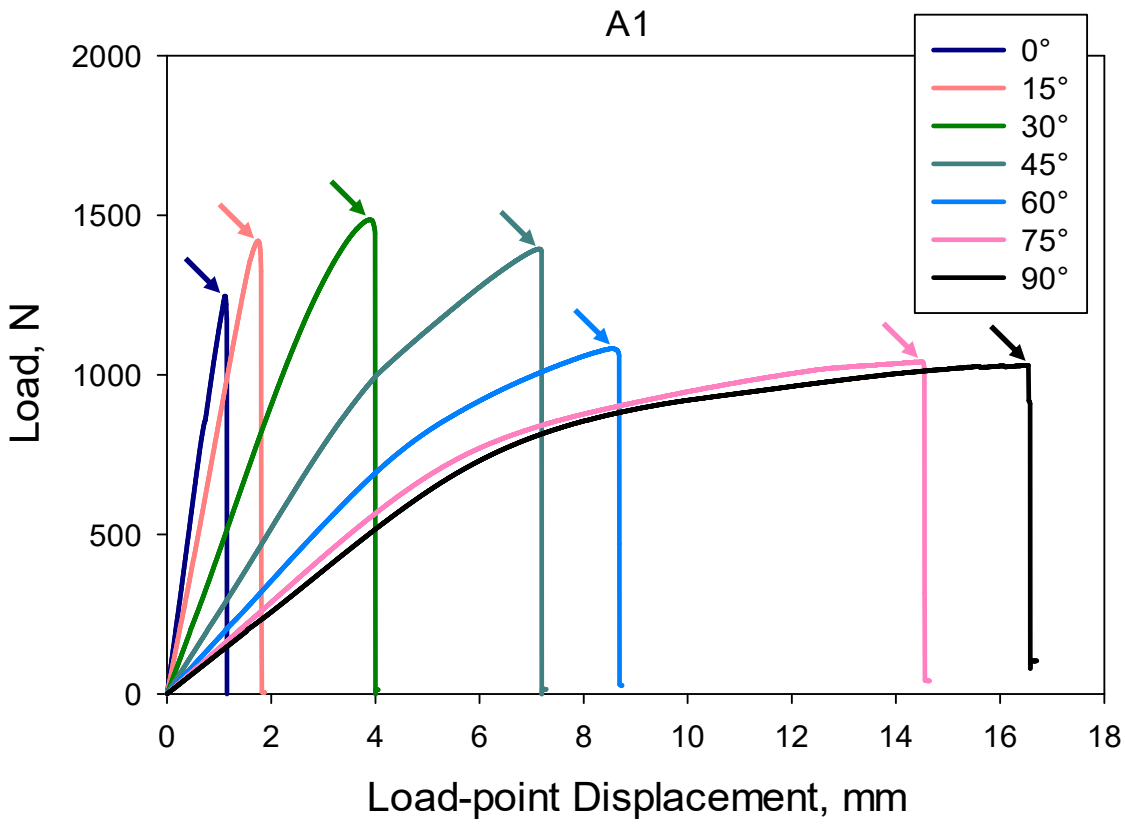

Figure 5.7: Load vs. load-point displacement curves for the A1 architecture tested at seven different loading angles (α). The arrows correspond to the crack initiation loads.

The load vs. load-point displacement curves for the Arcan specimen for the A2 architecture is shown in Figure 5.8. At α= 0°, a linear increase in load with load-point displacement was observed until peak load at which the crack initiated. After crack initiation, a drop in load was observed with a substantial amount of gradual or slow crack growth. However, unstable crack growth occurred after initiation once the $(a\ /\ W)$ ratio reached ~0.75. At α of 15°, the crack initiated at the peak load followed by a very small crack growth regime. The observed crack growth was followed by an abrupt failure seen as a sudden drop in load history. When α was 30°, a linear response was seen until peak load followed by a brittle failure. At α = 45°, 60°, 75°, and 90°, a linear response was observed initially and was followed by nonlinearity until failure at the corresponding peak load. Considering the peak loads for the A2 architecture, the peak load increased when α increased

from 0° to 15°. However, the peak loads began to drop as α increased from 15° to 90°. Both load-point displacement at failure and the nonlinear portion of the response increased as the loading angles increased from 45° to 90°. Also, just like the A1 architecture, the stiffness of the fracture responses decreased for the A2 architecture as the α values changed from 0° to 90°.

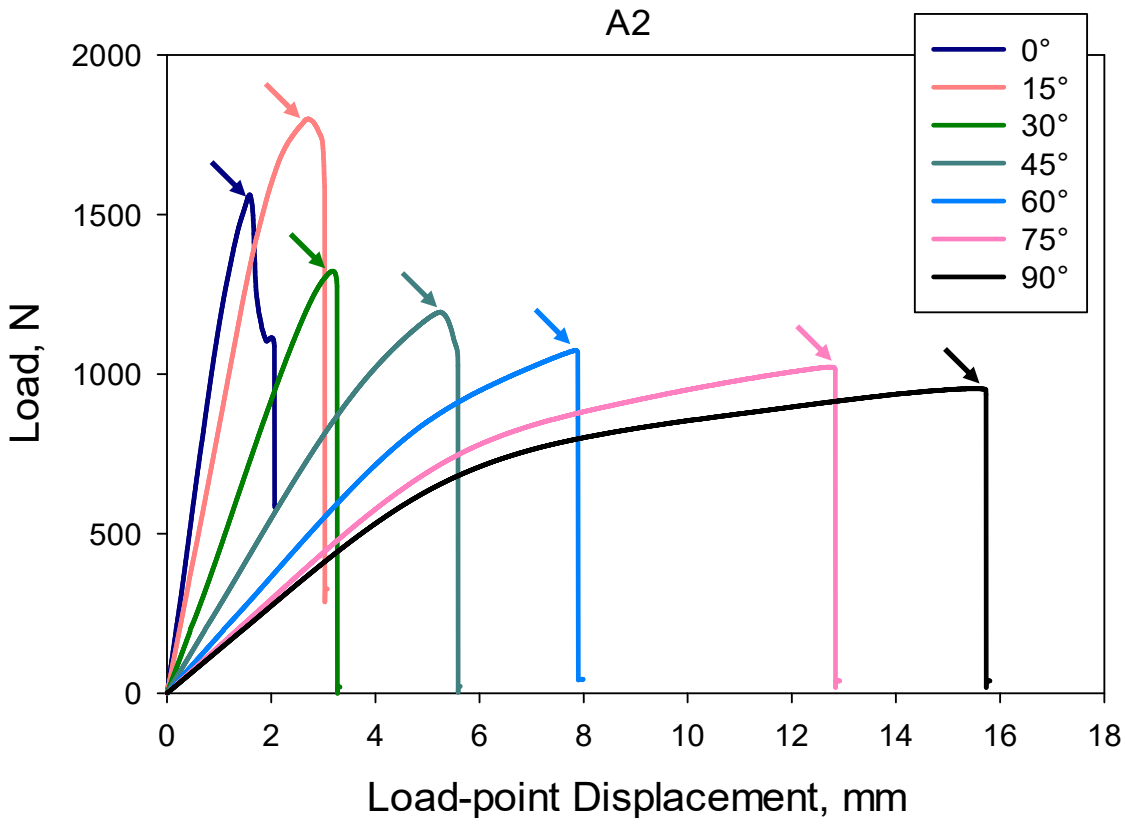

Figure 5.8: Load vs. load-point displacement curves for the A2 architecture tested at seven different loading angles (α). The arrows correspond to the crack initiation loads.

The load vs. load-point displacement curves for specimens with the print architecture A3 are shown in Figure 5.9. At α of 0°, a linear response of load was observed until crack initiation which happened before the peak load. The crack growth was observed with an increase in load and the load began to drop subsequently. Once the $(a\ /\ W)$ reached a ratio of ~0.8, unstable crack growth occurred. At α of 15°, 30°, and 45°, the crack initiated at the peak load and minimal crack propagation regime was seen in each case followed by an abrupt failure. At α of 60°, 75°, and 90°,

a linear response followed by a significant nonlinear regime was observed. An unstable crack growth occurred at or close to the peak load and with an increase in α from 60°, 75°, and 90°, increase in the nonlinear portion and load-point displacement at failure were observed. Also, just like the A1 and A2 architectures, the stiffness (initial slope of load vs. deflection response) of the fracture responses decreased and load-point displacement at failure increased for the A3 architecture as the α increased from 0° to 90°. Considering the peak loads for the A3 architecture, the peak load increased when α changed from 0° to 15°. However, the peak loads dropped as α increased from 15° to 90°.

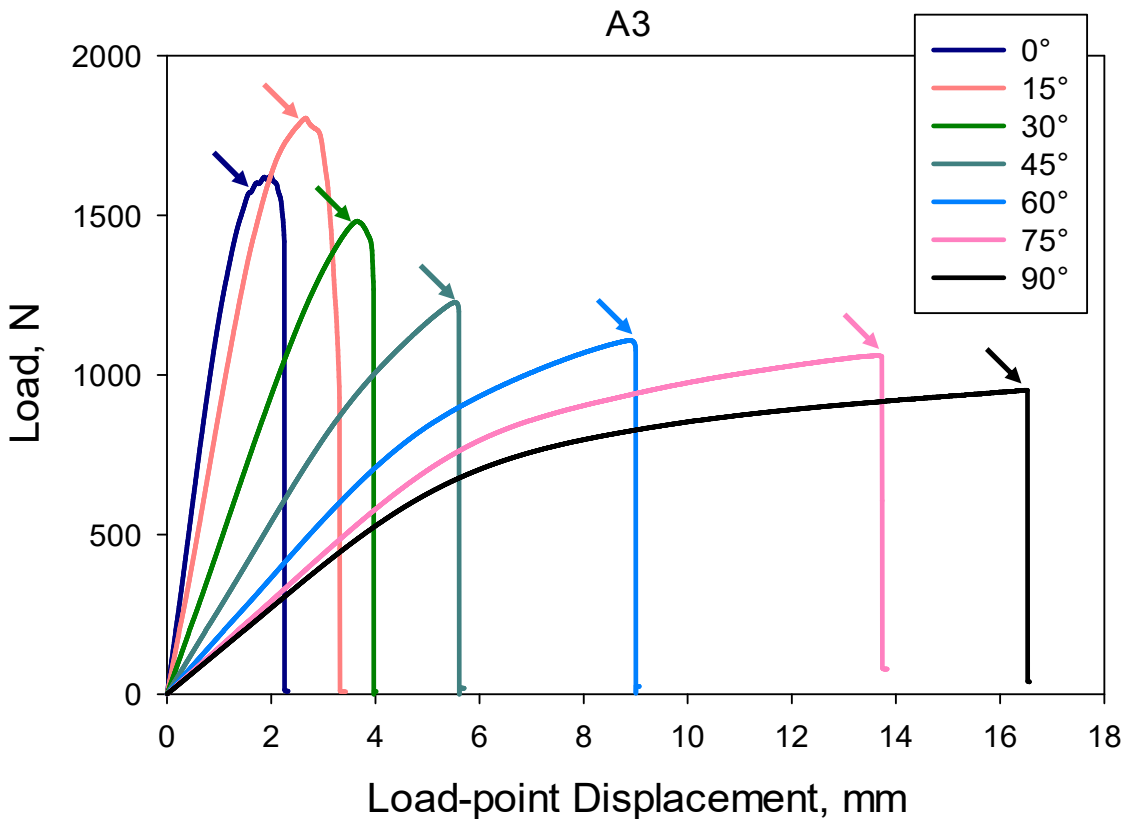

Figure 5.9: Load vs. load-point displacement curves for the A3 architecture tested at seven different loading angles (α). The arrows correspond to the crack initiation loads.

The load vs. load-point displacement curves for all three architectures for each of the loading angles (α) are shown individually in Figure 5.10. For α of 0°, A3 architecture had the best

performance followed by A2 and A1 respectively. An abrupt failure was observed for A1 whereas a slow crack growth was observed in case of A2 and A3 architectures. Regarding crack growth in A2 and A3 architectures, increase in load with crack growth was observed only in A3. At α = 15°, both A2 and A3 architectures had a better load bearing capacity than the A1architecture, with A3 having a marginally better post-initiation response than A2. An abrupt fracture was observed for A1 whereas small crack growth was observed for A2 and A3. At α = 30°, A1 and A3 architectures had a better response than the A2 architecture. Between A1 and A3 tested at α of 30°, A1 had a slightly higher crack initiation load than the A3 architecture. The A1 architecture had a much better failure response than the A2 and A3 architectures at α = 45°, with A2 and A3 having rather similar responses. At the α of 60°, A3 architecture had the highest peak load, closely followed by that for the A1 architecture and A2 had the least favorable response among the three. At higher α of 75° and 90°, A1 architecture had the best fracture response followed by A3 architecture and then the A2 architecture. However, A1 and A3 had similar peak loads with A1 having a higher load-point displacement at failure at α= 70° while A1 had higher peak load than A3 when α= 90° with similar displacement at failure. Abrupt fractures were observed for all three architectures at all α from 45° to 90°. A second set of experiments were performed for all three architectures in seven different loading angles and the resulting load vs. load-point displacement curves are shown in Figure 5.11.

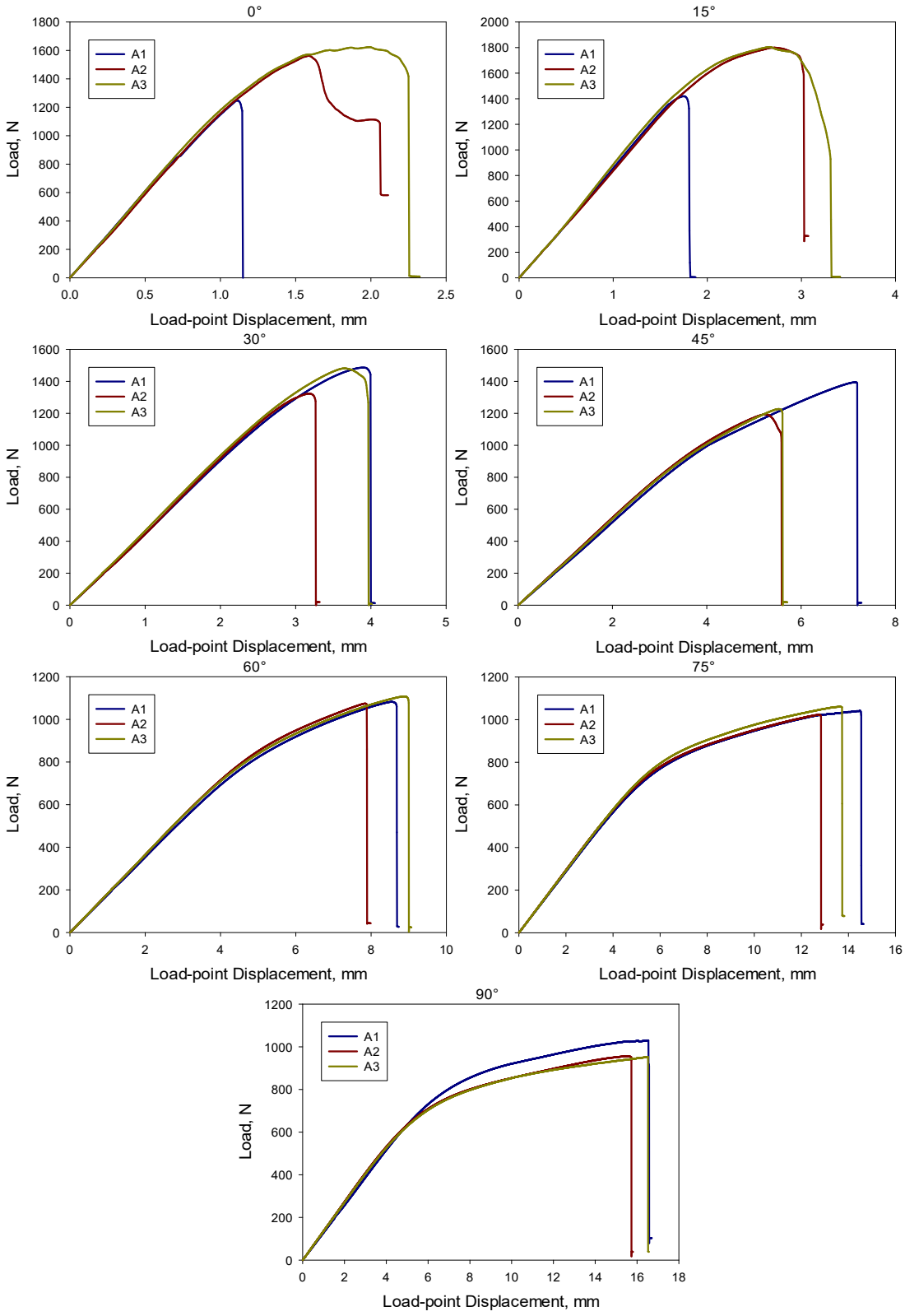

Figure 5.10: Load vs. load-point displacement curves for the three architectures at each of the loading angles (α).

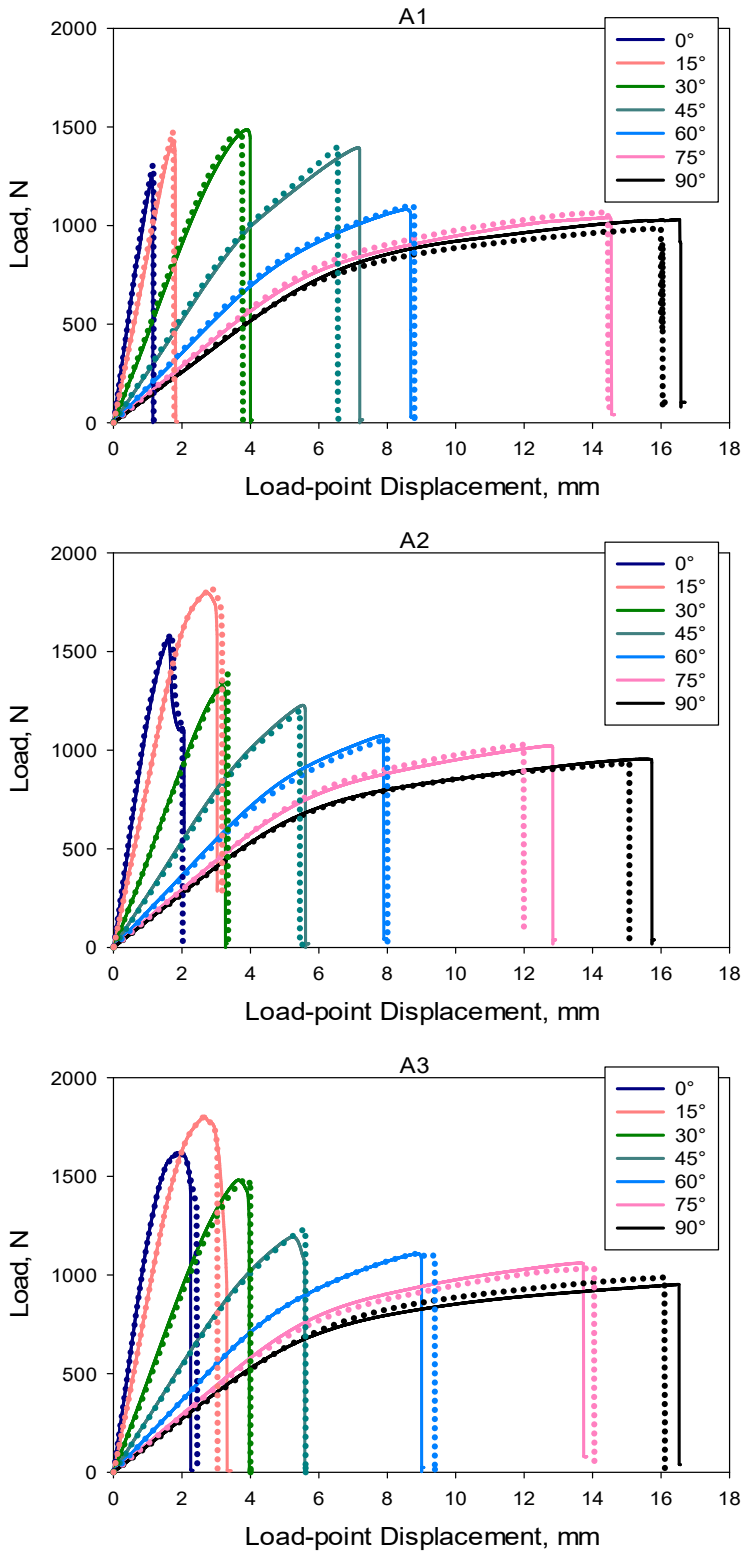

Figure 5.11: Repeatability for load vs. load-point displacement curves for the three architectures tested at seven different loading angles (α).

The crack paths observed in the three architectures subjected to different loading angles (α) are photographed. The reassembled fractured specimens are shown in Figure 5.12. Specimens of A1, A2, and A3 architecture are shown in the first, second, and third columns of Figure 5.12 respectively. A mode-I failure along the 90° layer was noted for the A1 architecture for all seven loading angles. As observed from the fracture responses for specimens with the A1 architecture, brittle failure was evident from crack paths with no apparent crazing (whitening of crack flanks) along the crack edges. The A2 architecture at a α of 0° had a global mode-I failure. However, jagged crack edges along the -45° and +45° layers combined with crazing was noted. The A2 architecture at α = 15° had a ductile response and it is evident from the observed crack path as well. The crack initiated along -45° direction and then like the previous loading angle, had a jagged edge (locally along -45° and +45° layers) and crazing while the crack grew in a curved path approximately at -25°. The A2 architectures tested at α = 30°, 45°, 60°, 75°, and 90°, all fractured along a -45° layer. Noting the abrupt drop in load observed after the peak load from fracture responses when α = 60°, 75°, and 90°, unstable crack growth is evident from the crack paths considering the clean edges along the crack path. The A3 architecture had a mode-I failure along the 90° layer at α = 0°, 15°, 75°, and 90°. The A3 specimens tested at α= 0° and 15° had a hint of jagged crack edges besides crazing along the crack path, whereas specimens tested at α = 75° and 90° had clean edges signifying unstable crack growth observed during their failure. The A3 architecture at α= 30° had crack growth occurrence along approx. -35° whereas architectures at α= 45° and 60° had failure along -45°layer. Also, it was noted that a few (α = 45°, 60°, and 90°) of the A3 architectures shift their crack path during abrupt fracture. The most significant among

them being the α = 90° case, where the A3 specimen initially broke along the 90° layer and then shifted to a -45° layer and alternated back to the 90° layer.

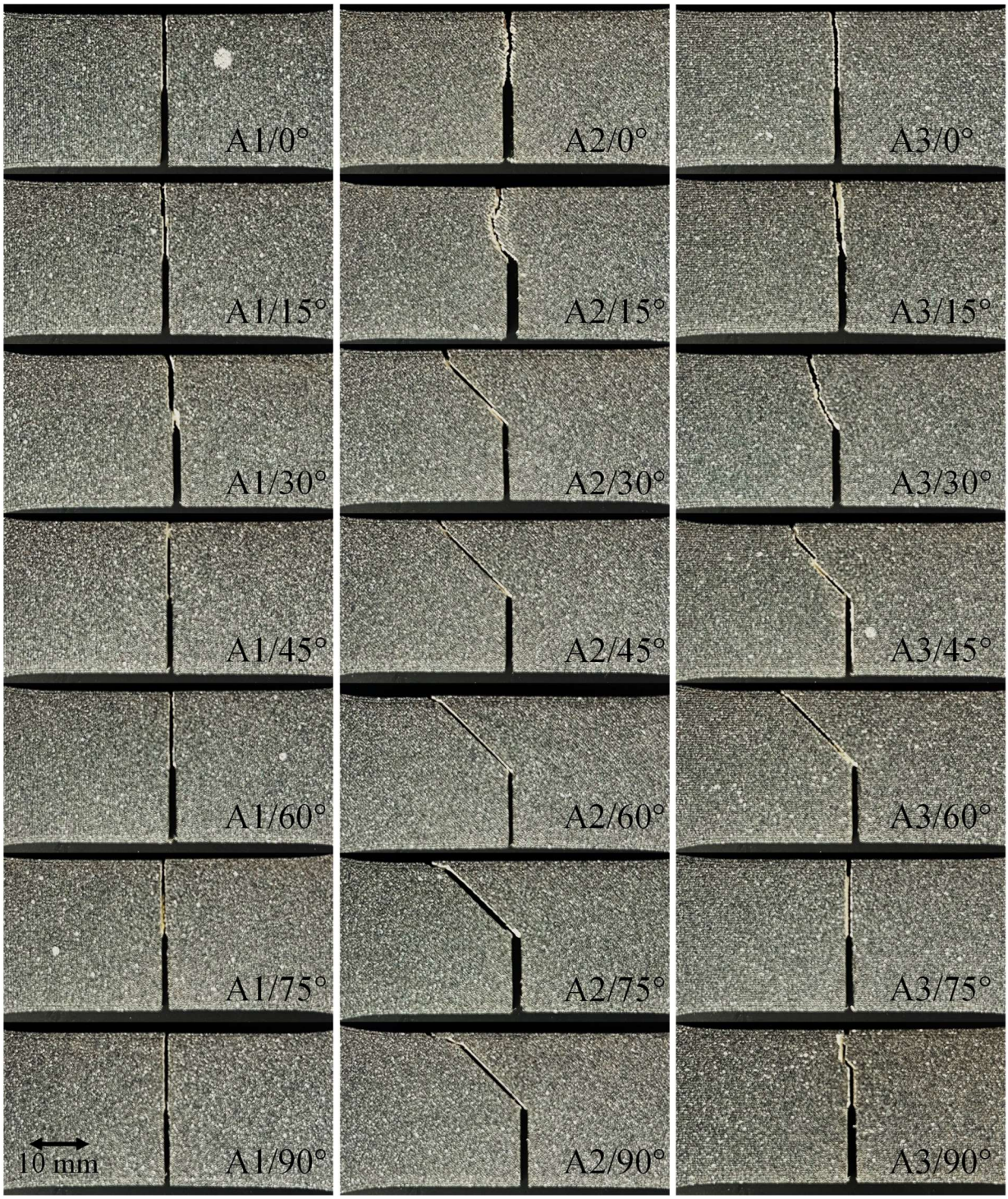

Figure 5.12: Photographs of observed crack path in fractured Arcan specimens. Labels in the picture correspond to print architecture/loading angle.

The gray scale photographs of speckle pattern applied on the specimen surface recorded by the camera in the deformed state were correlated with the reference images recorded before the application of load to obtain full-field displacements in two orthogonal directions, along (x) and perpendicular (y) to the initial crack orientation. The correlation was performed with ARAMIS, an image analysis software. All parameters related to correlation are given in Table 5.1.

Table 5.1 – DIC parameters associated with the mixed-mode fracture experiments.

Hardware Parameters		**Analysis Parameters**	
Camera Manufacturer Model Image Resolution	Point Grey Grasshopper3 GS3-U3-41C6M 2048 x 2048	Software Package Name Manufacturer	Aramis® 6.2.0 GOM
Lens Manufacturer Model Focal Length	Computar Lens 18-108 mm	Image Filtering	None
FOV	80 mm x 80 mm	Sub-image/Subset Size	20 x 20
Image Scale	25 pixel/mm	Step Size	10
Stereo-Angle	N/A	Subset Shape Function	Affine
Stand-Off Distance	0.6 m	Data Processing and Filtering for QOIs	None
Image Acquisition Rate	2 fps	Noise-floor and Bias of QOIs	1 μm
Patterning Technique	Spray painted		
Approx. Feature Size	5 pixels		

Representative displacement contours for all the specimens tested using Arcan fixture at seven different loading angles are shown in Figure 5.13 to Figure 5.19. Speckle images from the A2 architectures and their corresponding displacement fields in two orthogonal directions at a loading

angle α = 0° are shown in Figure 5.13. The displacement contours are as expected for a mode-I crack. That is, the u-field displacement contours are symmetric in shape and magnitude with respect to the crack orientation whereas the v-field displacement contours are symmetric in shape but antisymmetric in magnitude. As α increases from 15° to 75° (Figure 5.14 – Figure 5.18), asymmetry with respect to the crack can be observed to increase in the v-fields. Displacement contours converging to the crack tip and parallel to the initial crack can be observed in the u-fields. Also, as the contribution of mode-II loading increases (or as α increases), the displacements in the u-fields become antisymmetric in magnitude indicating the in-plane shear on the crack. Figure 5.19 shows the displacement contours for both the fields at α = 90°. Symmetric contours in shape and magnitude can be observed for the v-field whereas contours that are symmetric in shape but antisymmetric in magnitude are evident in the u-field.

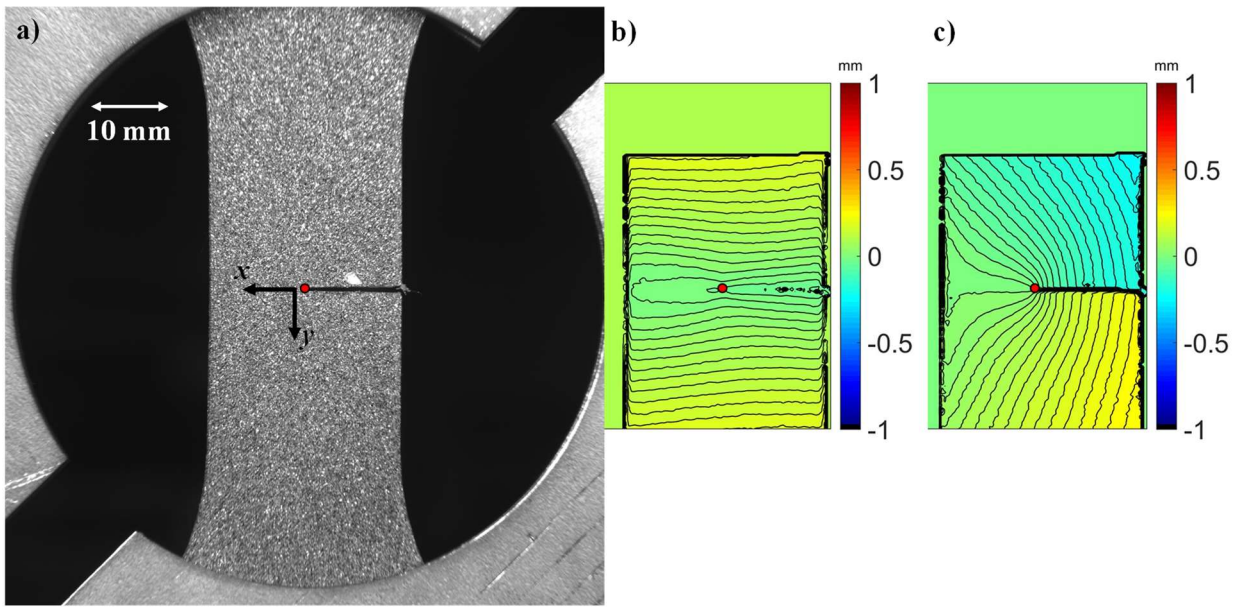

Figure 5.13: Displacement contours of A2 at α = 0°, with a contour interval of 15 μm, obtained through DIC (a) Speckle images at a load step (591 N) and its corresponding (b) *x*- or *u*-field, (c) *y*-or *v*-field. Red solid dots indicate the crack tip location at this load step.

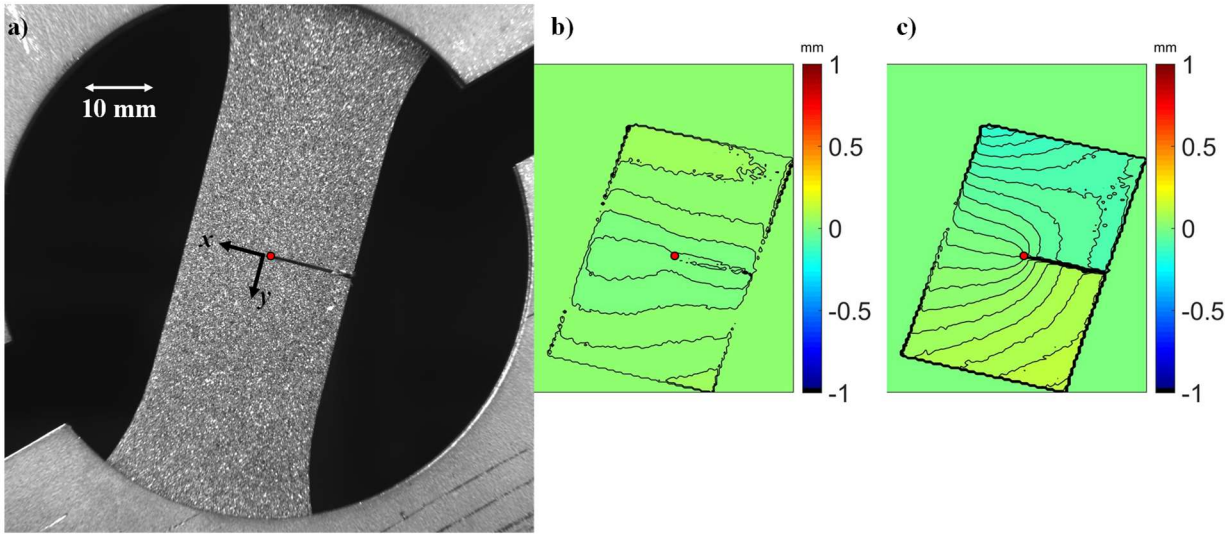

Figure 5.14: Displacement contours of A2 at α = 15°, with a contour interval of 15 μm, obtained through DIC (a) Speckle images at a load step (594 N) and its corresponding (b) *x*- or *u*-field, (c) *y*-or *v*-field. Red solid dots indicate the crack tip location at this load step.

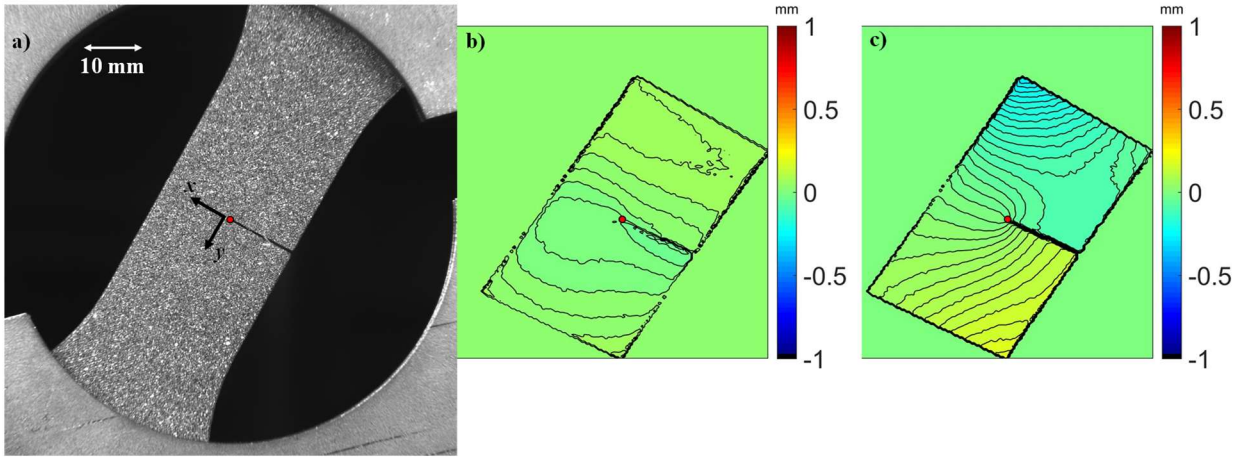

Figure 5.15: Displacement contours of A2 at α = 30°, with a contour interval of 15 μm, obtained through DIC (a) Speckle images at a load step (604 N) and its corresponding (b) *x*- or *u*-field, (c) *y*-or *v*-field. Red solid dots indicate the crack tip location at this load step.

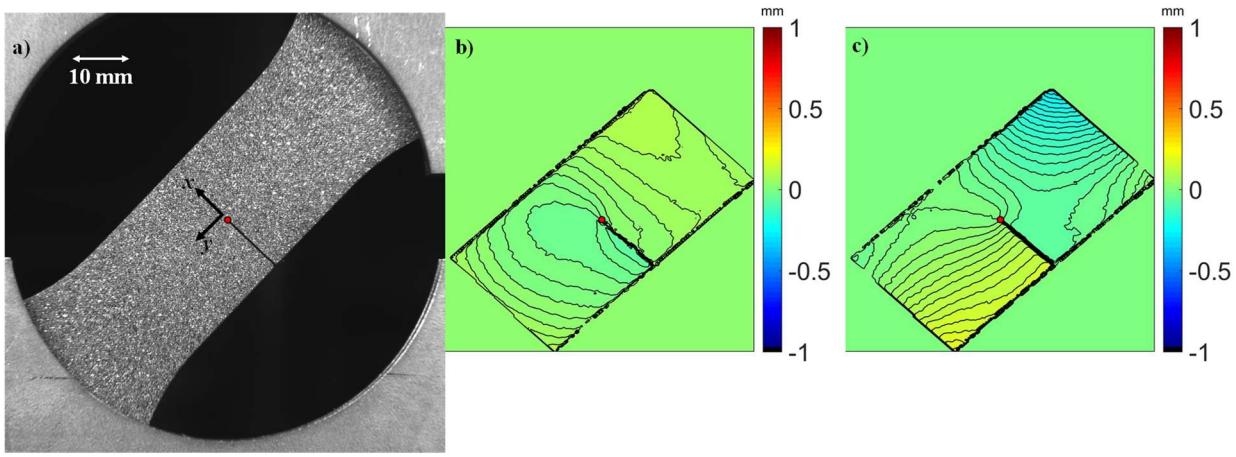

Figure 5.16: Displacement contours of A2 at α = 45°, with a contour interval of 15 µm, obtained through DIC (a) Speckle images at a load step (603 N) and its corresponding (b) *x*- or *u*-field, (c) *y*-or *v*-field. Red solid dots indicate the crack tip location at this load step.

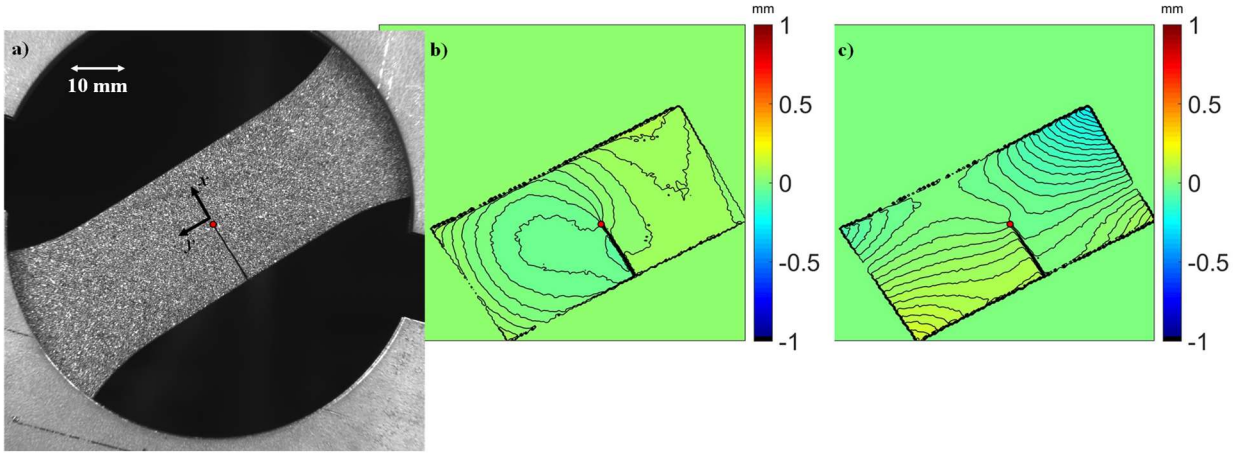

Figure 5.17: Displacement contours of A2 at α = 60°, with a contour interval of 15 µm, obtained through DIC (a) Speckle images at a load step (601 N) and its corresponding (b) *x*- or *u*-field, (c) *y*-or *v*-field. Red solid dots indicate the crack tip location at this load step.

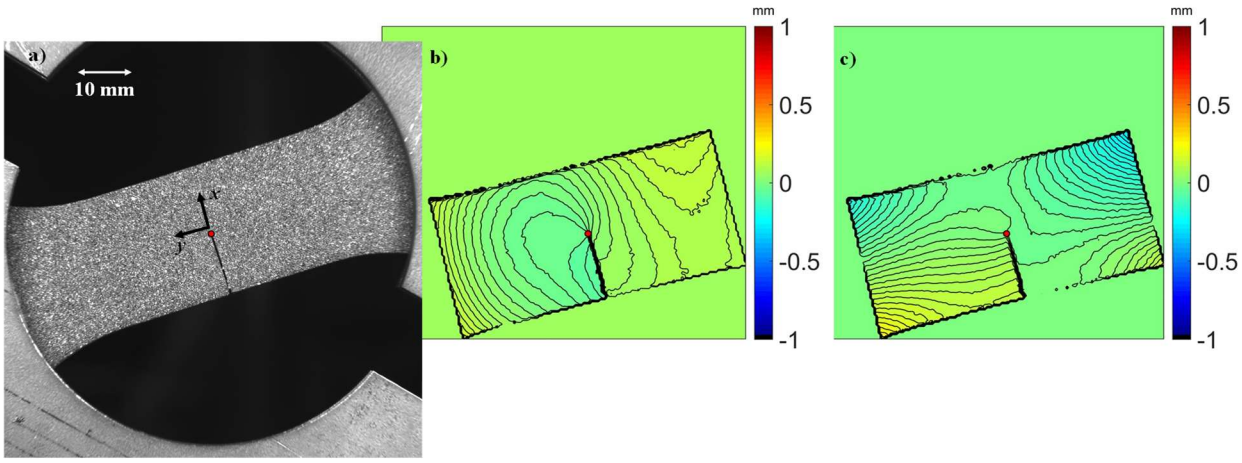

Figure 5.18: Displacement contours of A2 at α = 75°, with a contour interval of 15 µm, obtained through DIC (a) Speckle images at a load step (601 N) and its corresponding (b) *x*- or *u*-field, (c) *y*-or *v*-field. Red solid dots indicate the crack tip location at this load step.

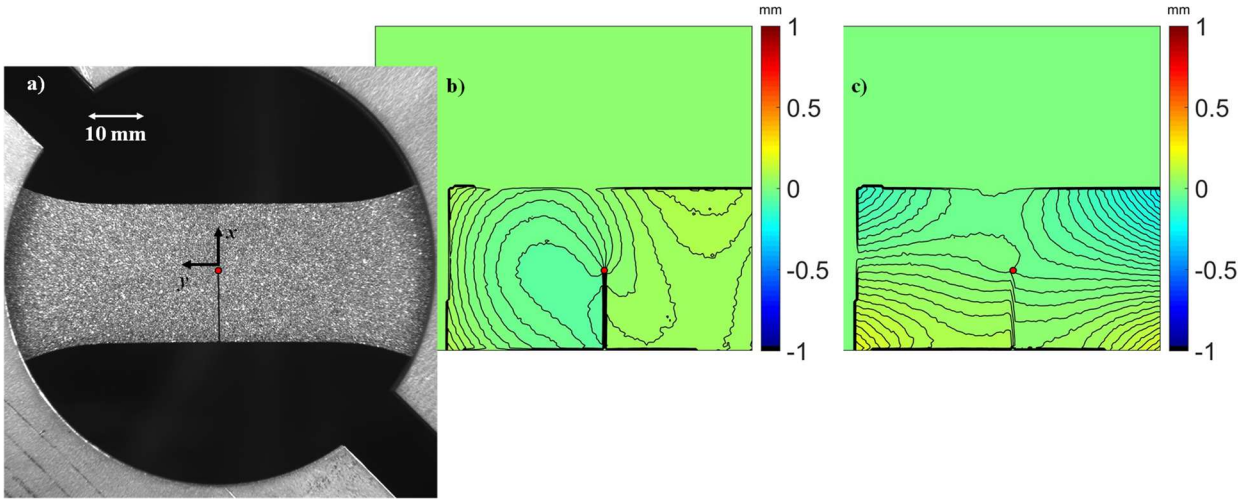

Figure 5.19: Displacement contours of A2 at α = 90°, with a contour interval of 15 µm, obtained through DIC (a) Speckle images at a load step (602 N) and its corresponding (b) *x*- or *u*-field, (c) *y*-or *v*-field. Red solid dots indicate the crack tip location at this load step.

The experimentally obtained displacements were used as surface boundary conditions in identical FE models to extract the energy release rate and individual SIFs as detailed in Chapter 2. The energy release rate and SIFs were extracted from the crack tip region corresponding to *r/B* ratio of ~0.4-2.4. Representative plots depicting the variation of *J* and SIFs for the A1 architecture at crack initiation at three different loading angles (α) is shown in Figure 5.20.

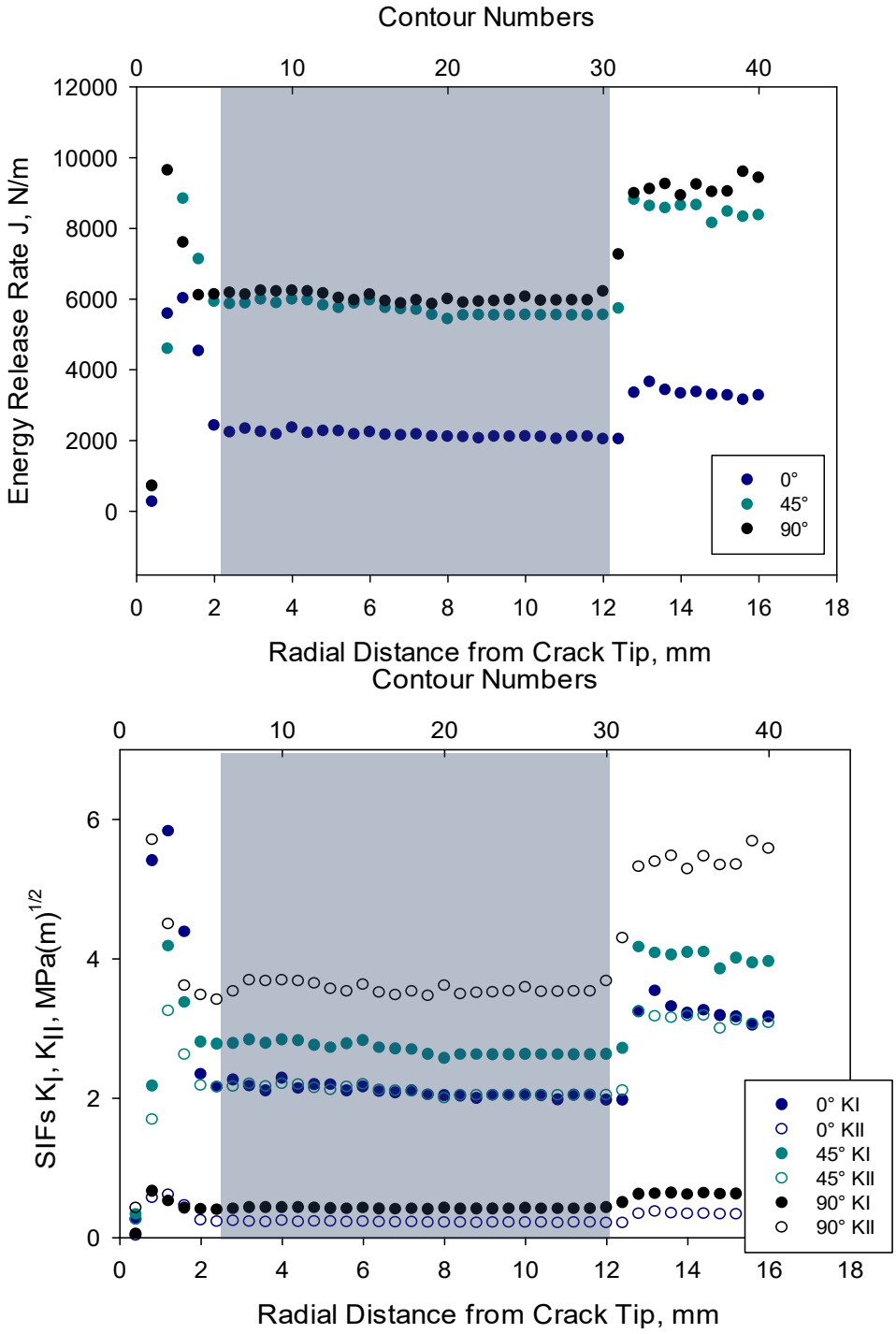

Figure 5.20: Representative plots showing the path dependence for *J*-value and SIFs for the A1 architecture at crack initiation for loading angles 0°, 45°, and 90°. The *J*-value and SIFs varies by < 5% in the shaded region.

Before exploring the fracture behaviors, the variation of mode-mixity (Ψ) at crack initiation against the loading angle (α) is shown in Figure 5.21. Two sets of fracture experiments were performed and the average mode-mixity (Ψ) values at crack initiation are shown with error bars. The crack initiation was identified by inspecting the speckle images and displacement contours. Their respective K_I and K_{II} values were extracted and mode-mixity ($\Psi = \tan^{-1}\frac{K_{II}}{K_I}$) was calculated from the two SIFs at crack initiation. If Ψ < 45°, the loading corresponds to mode-I dominant condition and if Ψ > 45°, the loading is said to correspond to mode-II dominant condition. Hence from the results, it is evident that for α values of 0°, 15°, 30°, and 45°, the loading is mode-I dominant and for α values of 60°, 75°, and 90°, the loading is mode-II dominant. The α = 60° case had a Ψ with equal contributions of mode-I and mode-II. Nearly mode-I and mode-II conditions was evident when α was 0° and 90° respectively.

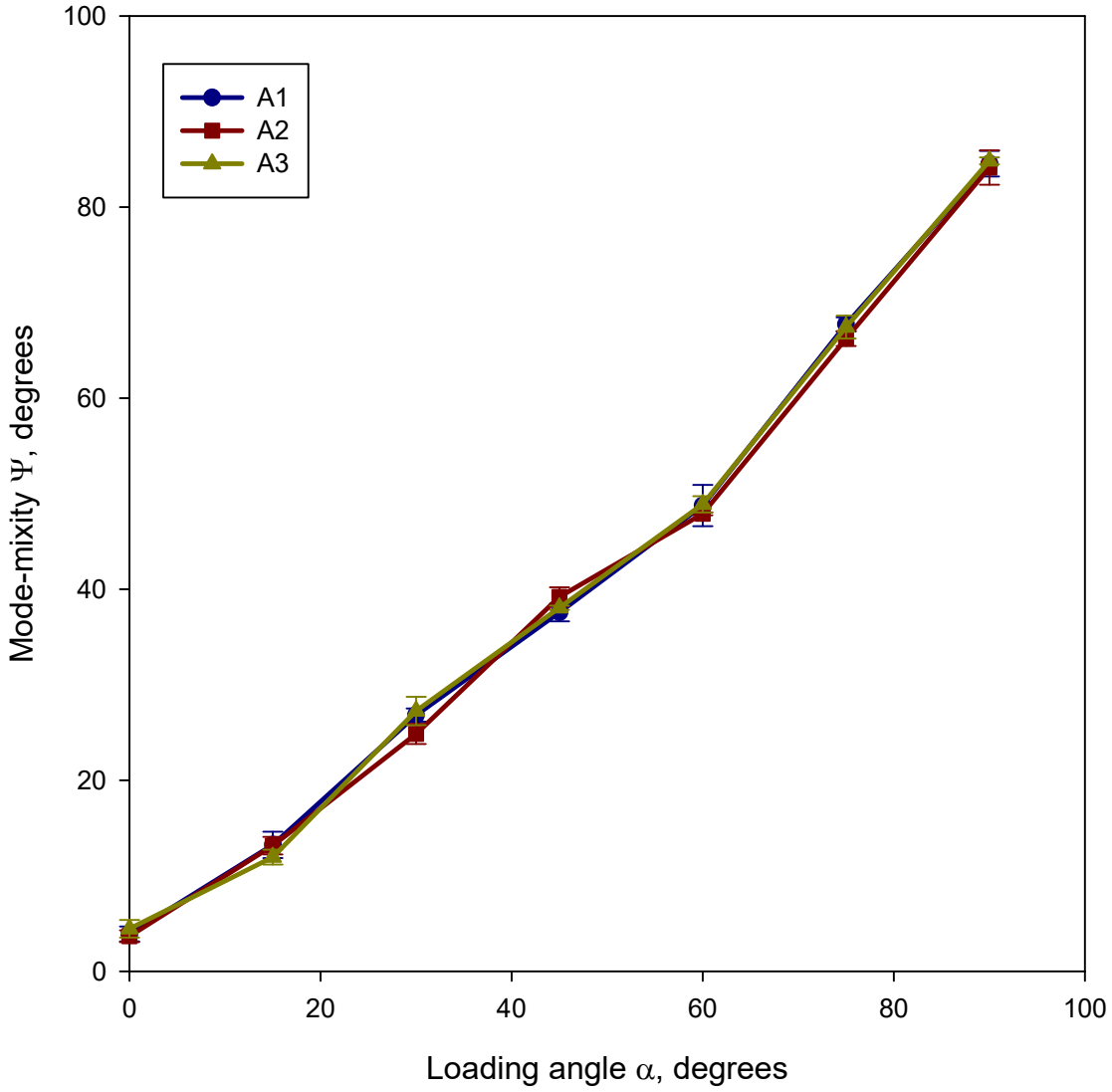

Figure 5.21: Experimental mode-mixity (Ψ) for the three architectures at different loading angles (α).

The mode-mixity obtained in this work was also compared with several other Arcan fixtures reported in the literature and similar trends were observed. The mode-mixity variation from five independent research groups with Arcan fixtures of different geometries is compared with the experimental mode-mixity (Ψ) from this work; the results are shown in Figure 5.22 [90-94]. Similar trends of increase in mode-mixity with the loading angle can be observed. The

difference in Ψ at each loading angle between different works is expected as the specimen geometry and Arcan plate geometry influence the nature of loading applied to the specimen and they are different in each of these works. Also, regarding the disparity seen in the values of Ψ for pure mode-I (α=0°) and mode-II (α=90°) conditions, the SIFs in the compared works were calculated with the help of failure loads and correction factors obtained complementarily from FE analyses. These correction factors are designed to give the theoretical mixity values of 0° and 90° for pure mode-I or mode-II loading respectively. The usage of optical measurements to obtain experimental mode-mixities in this work gives mixity values that are closer to 0° and 90° for pure mode-I or mode-II loading respectively.

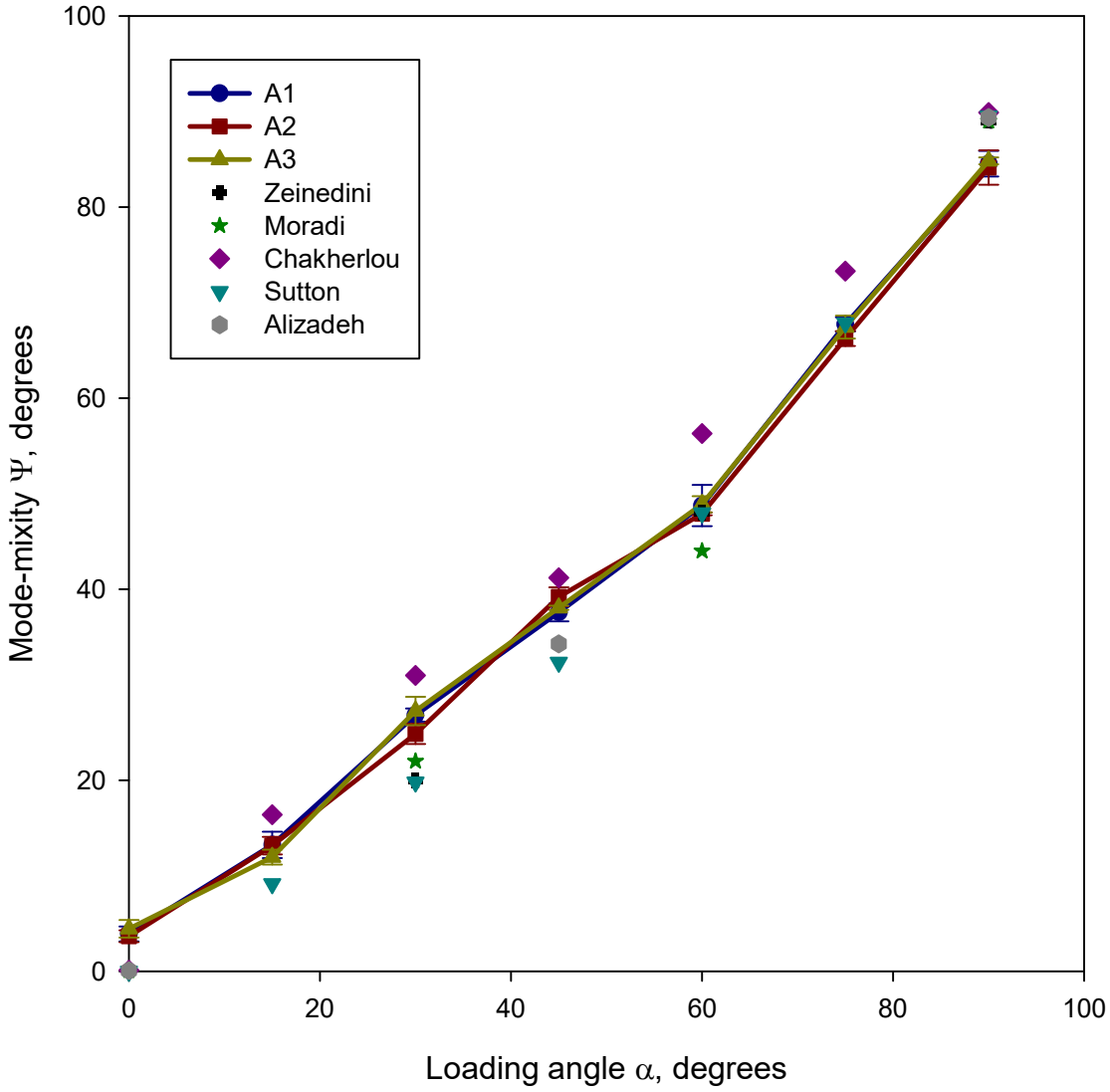

Figure 5.22: Mode-mixity comparison with other Arcan fixtures available in literature [90-94].

The energy release rate or the *J*-integral histories for the A1 architecture tested at all the different loading angles (α) is shown in Figure 5.23. The crack initiation instant was identified as $t = 0$. Hence, the negative and positive timescales correspond to energy release rate values before and after crack initiation, respectively. The energy release rate value at $t = 0$ corresponds to the critical energy release rate. It can be noted that the A1 architecture tested at $\alpha = 0°$ and 15° had a monotonic increase in energy release rate until crack initiation followed by an abrupt fracture. The

specimens tested at α = 30°, 45°, 60°, 75°, and 90° also had a monotonic increase in energy release rate and was followed by a nonlinear response before crack initiation. The nonlinear regime increased as α increased from 30° to 90°. The highest critical energy release rate was observed for α = 30° and the lowest was for α = 0° (mode-I). Considering the crack propagation behavior, the crack growth was captured only at α = 30°, where an unstable/rapid crack growth after initiation was evident. Specimens tested at other loading had abrupt failure or unstable crack growth where the specimens failed completely before images could be captured at low recording rates of a PointGrey camera.

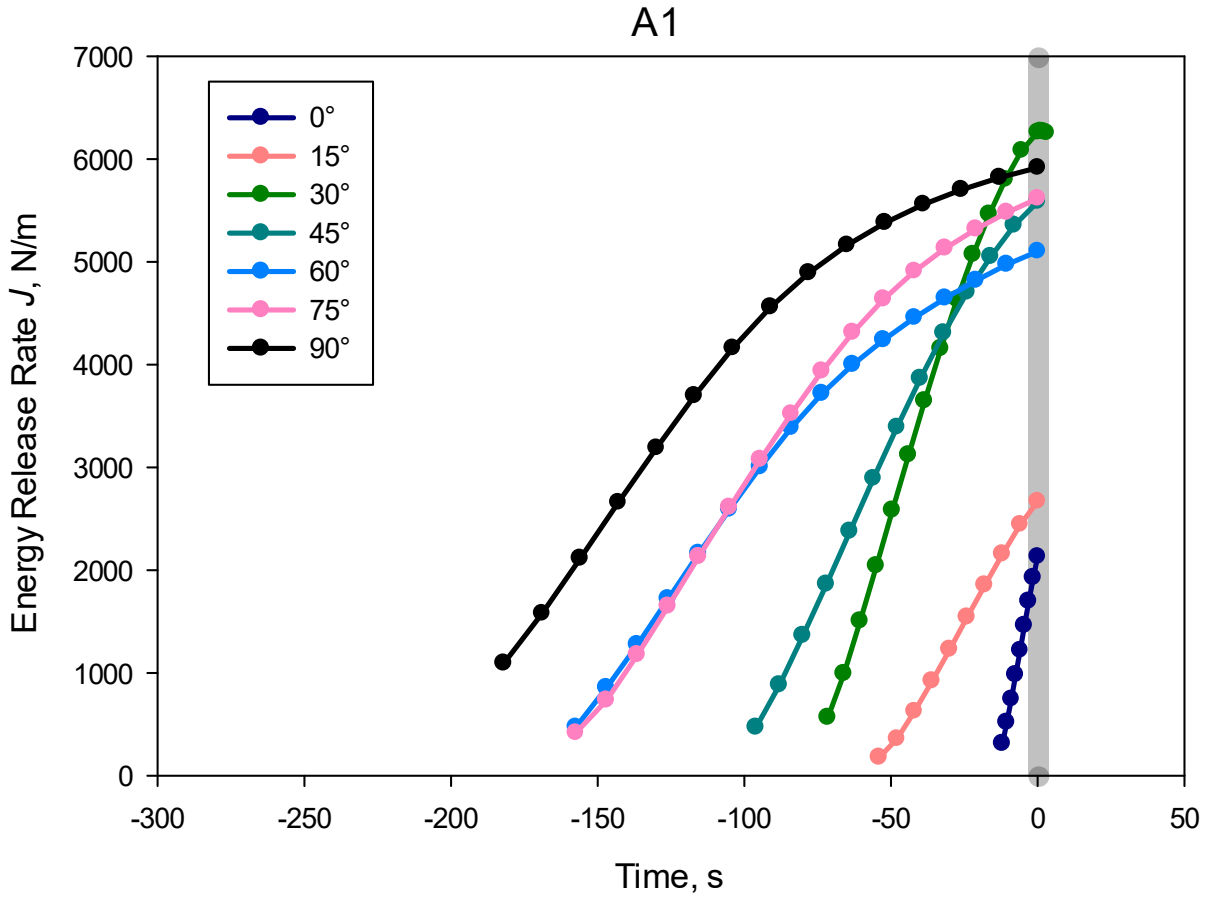

Figure 5.23: *J*-integral histories for the A1 architecture tested at different loading angles (α).

The energy release rate or the *J*-integral histories for the A2 architecture tested at all the different loading angles (α) is shown in Figure 5.24. Again, the crack initiation instant was identified as $t = 0$ and the negative and positive timescales correspond to energy release rate values before and after crack initiation respectively. A monotonic increase in energy release rate was observed until crack initiation for specimens tested at $\alpha = 0°$ and 15°. Specimens tested at other angles had a monotonic increase with a nonlinear response prior to crack initiation. Again, similar to the A1 architecture, nonlinear response region increased as α from 30° to 90°. Regarding the critical energy release rate, A2 architecture had the highest value for $\alpha = 15°$ and the lowest when $\alpha = 0°$. The crack growth was captured for specimens tested at $\alpha = 0°$, 15°, and 45°. A gradual drop in the energy release rate was observed with crack growth for $\alpha = 0°$ whereas an unstable crack growth was observed for 15° and 45°.

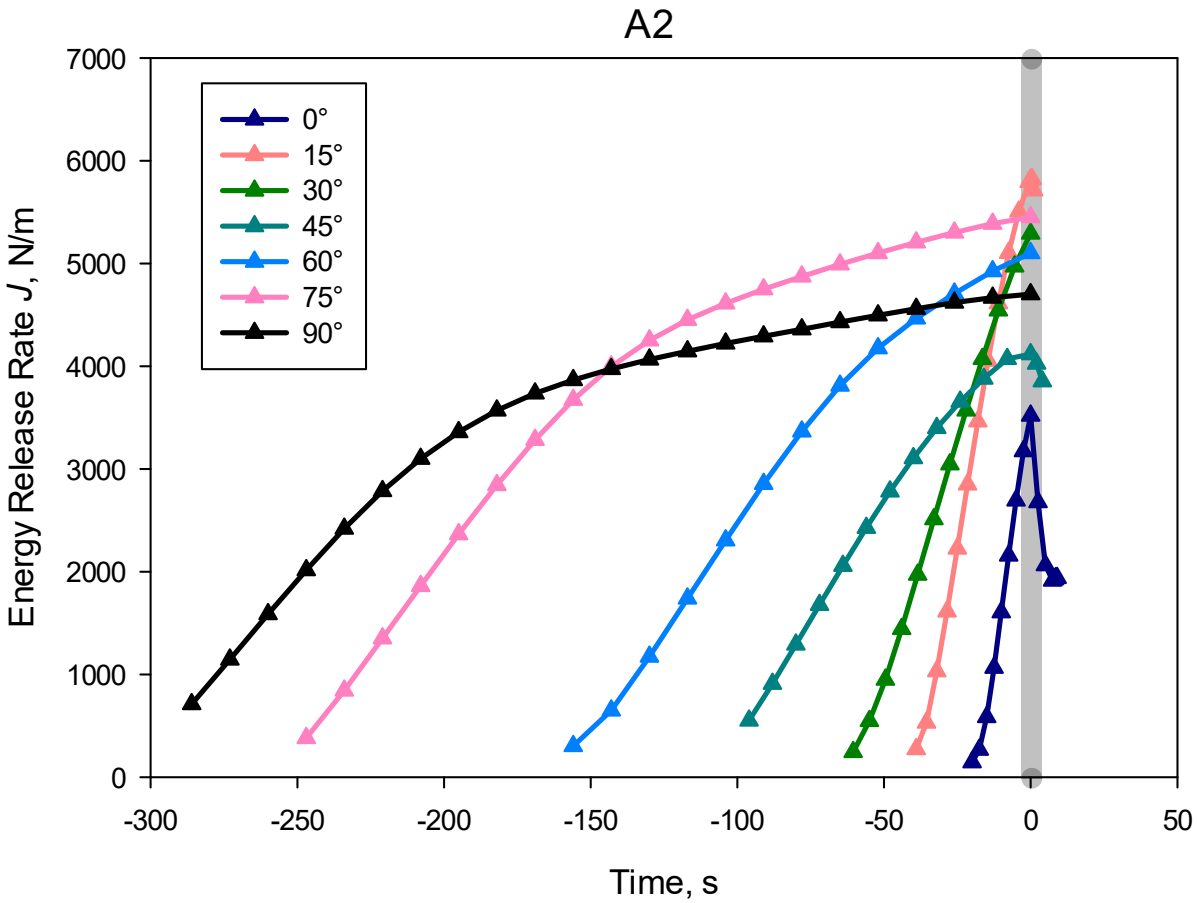

Figure 5.24: The ERR (*J*-integral) histories for the A2 architecture tested at different loading angles (α).

The energy release rate or the *J*-integral histories for the A3 architecture at all the different loading angles (α) is shown in Figure 5.25. Similar trends as the A1 and A2 architectures prior to crack initiation were observed in the A3 architecture as well. A monotonic increase in the energy release rate was observed for α = 0°, 15°, and 30° whereas specimens tested at α = 45°, 60°, 75°, and 90° had a monotonic increase with a nonlinear response prior to crack initiation. The highest critical energy release rate was observed in specimens tested at α = 30° and the lowest critical energy release rate was when α = 0°. Slow crack propagation was captured for α = 0°, 15°, and 30°. For mode-I loading (α = 0°), increase in energy release rate was observed with the initial

crack growth and an eventual gradual drop in values was observed with subsequent crack growth. For α = 15° and 30°, a gradual drop in the energy release rate was observed with crack growth.

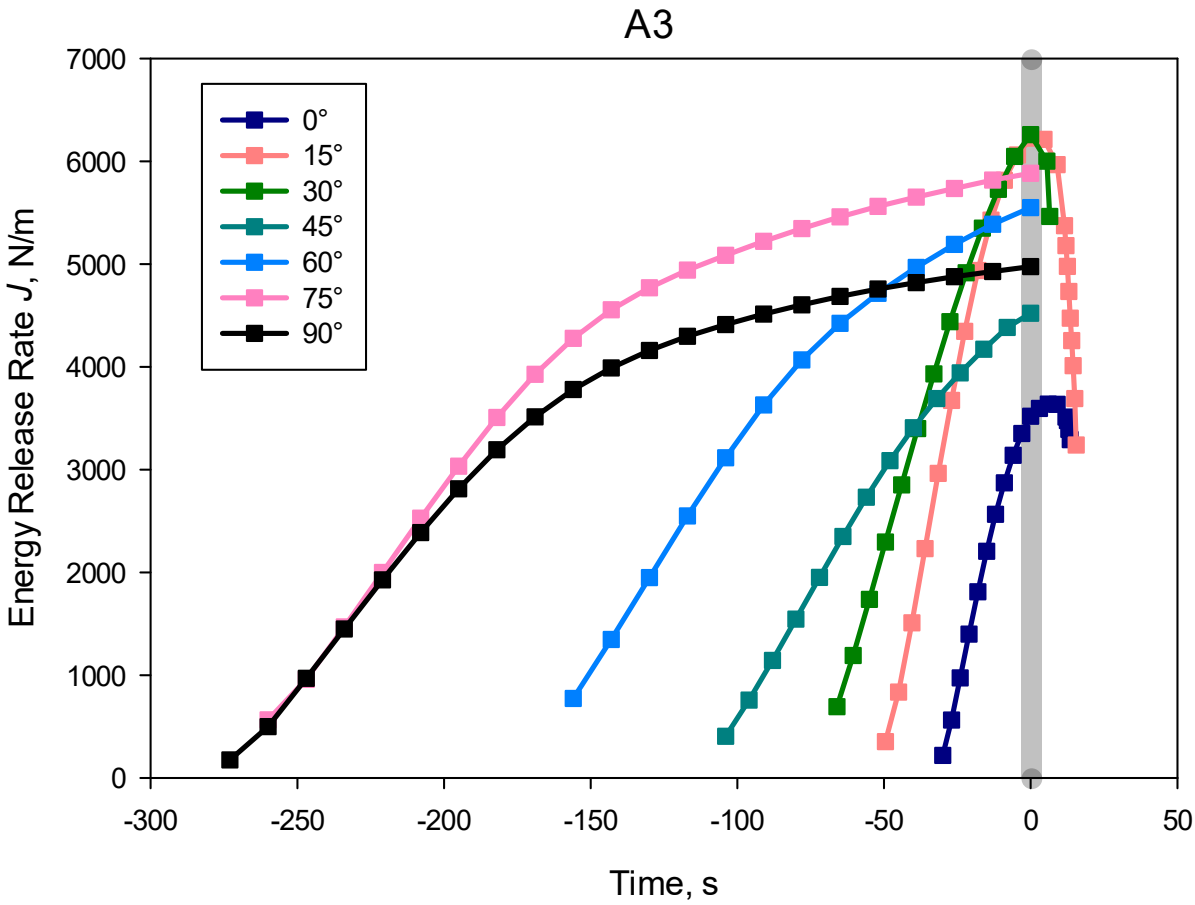

Figure 5.25: The *J*-integral histories for the A3 architecture tested at different loading angles (α).

The effective SIF (K_{eff}) can be calculated from individual SIFs ($K_{eff} = \sqrt{K_I^2 + K_{II}^2}$) which are obtained from the computed *J*-integral using the interaction integral method outlined in Chapter 2.2.3. The effective SIF at crack initiation is called the critical effective SIF. To compare the crack initiation performance across the three architectures for all the different loading angles, the critical effective SIF was plotted against the loading angle for A1, A2, and A3 architectures and is shown in Figure 5.26. Two sets of fracture experiments were performed and the average

values at crack initiation are shown with error bars. To recollect the nature of loading at different α, α = 0° corresponds to pure mode-I and α = 90° corresponds to pure mode-II condition. Angles α = 15°, 30°, and 45° correspond to mixed-mode (I/II) loading conditions with dominant mode-I and α = 60° and 75° corresponds to mixed-mode (I/II) loading with dominant mode-II. Across the three architectures for all loading angles, the lowest initiation values were found for pure mode-I loading case (α = 0°). Among the architectures for pure mode-I loading (α = 0°), A3 had the highest crack initiation toughness values closely followed by A2 and then A1 to have the least toughness. All three architectures had higher toughness values at initiation for pure mode-II loading (α = 90°) when compared to pure mode-I conditions. Among the three architectures for pure mode-II loading (α = 90°), A1 had the highest crack initiation toughness values followed by A3 and then A2. The crack initiation toughness for A1 architecture increased when α increased from 0° to 30° with 30° having the highest initiation toughness among all the loading angles. As α increased from 30° to 90°, initiation toughness values dropped before rising again. The A2 architecture showed an increase in the crack initiation toughness when α increased from 0° to 15°. The values for A2 however dropped when α increased from 15° to 45°. Again, the toughness values increased with α from 45° to 75°. The pure mode-II loading (α = 90°) had a lower crack initiation toughness than at 75° angle. The A2 architecture had its best performance at α = 15°. The A3 print architecture had a very similar trend as the A2 counterpart with the only difference being the best performance of A3 was at α = 30°. Among the loading conditions with a mode-II contribution, α = 45° configuration had a drop in initiation toughness relative to its neighboring angles of 30° and 60°. At α = 0°, 15°, 30°, 60° and 75°, the A3 architecture had the highest crack initiation toughness and at α = 45° and 90°, the A1 counterpart had the highest. Also, it should be

noted that all the loading angles (α = 15° to 90°) which had in-plane shear loading resulted in higher crack initiation toughness when compared to pure tensile loading at α = 0°.

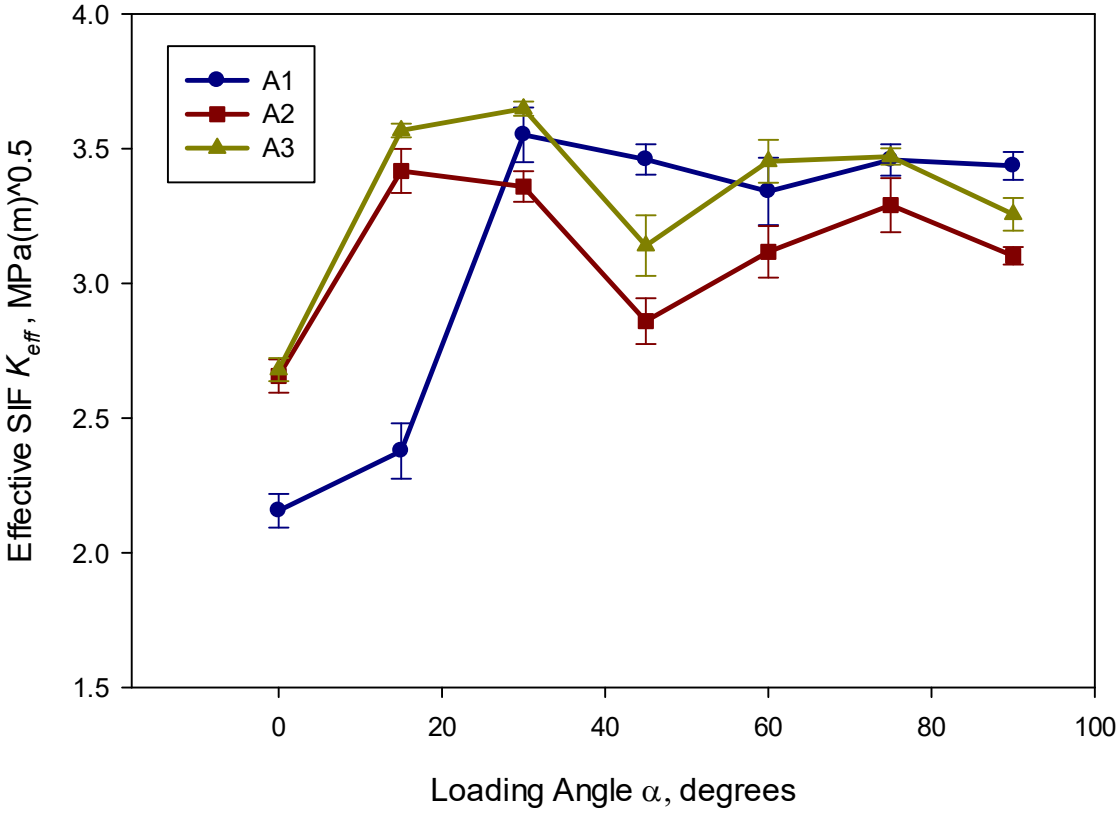

Figure 5.26: Variation in critical effective SIF with loading angle (α) for all three print architectures.

To understand the crack initiation response of all three print architectures, fracture envelopes were generated using critical mode-I and -II SIF values and are shown in Figure 5.27. In pure mode-I (α = 0°) and loading conditions with considerable mode-II contribution (α = 30°, 45°, 60°, 75°, and 90°), the A2 architecture consistently had lower initiation toughness than the A1 and A3 counterparts. The A1 architecture had relatively low values of initiation toughness in mode-I (α = 0°) and dominant mode-I loading conditions (α = 15°). Hence, it is reasonable to conclude that the overall fracture envelope for A3 architecture is better than A1 and A2. Also, from the *J*-integral

histories, it should be noted that the A3 architecture had more loading angles where slow crack growth was observed, and a stable crack growth was observed for the pure mode-I loading condition. Based on the fracture envelope and crack growth behavior, it can be stated that the A3 architecture has better overall fracture behavior than the A1 and A2 architectures.

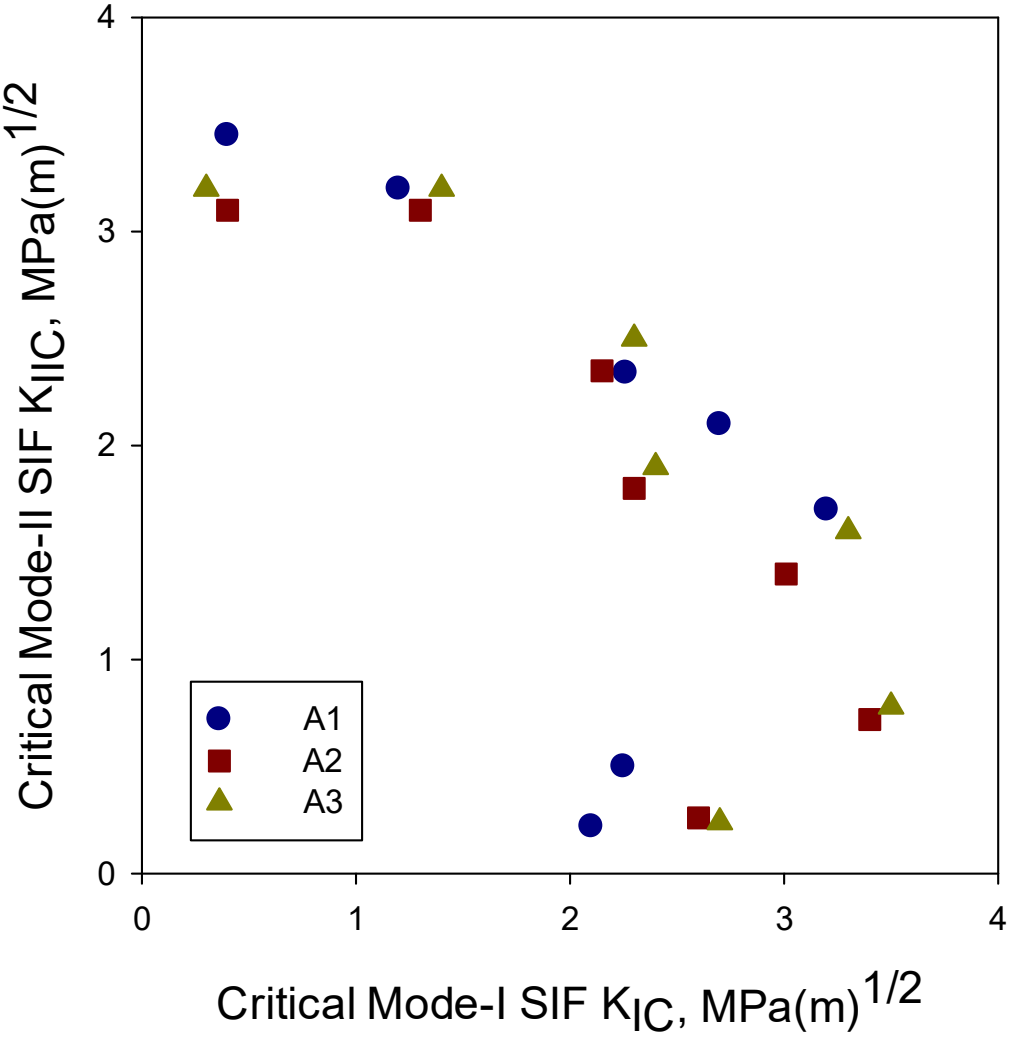

Figure 5.27: Fracture envelope of critical SIFs for the three architectures.

A second set of experiments were performed and the critical SIFs from those experiments are plotted in Figure 5.28 to demonstrate repeatability of results. Evidently, the overall fracture

envelope is similar to the one shown in Figure 5.27 with marginal differences within the experimental error.

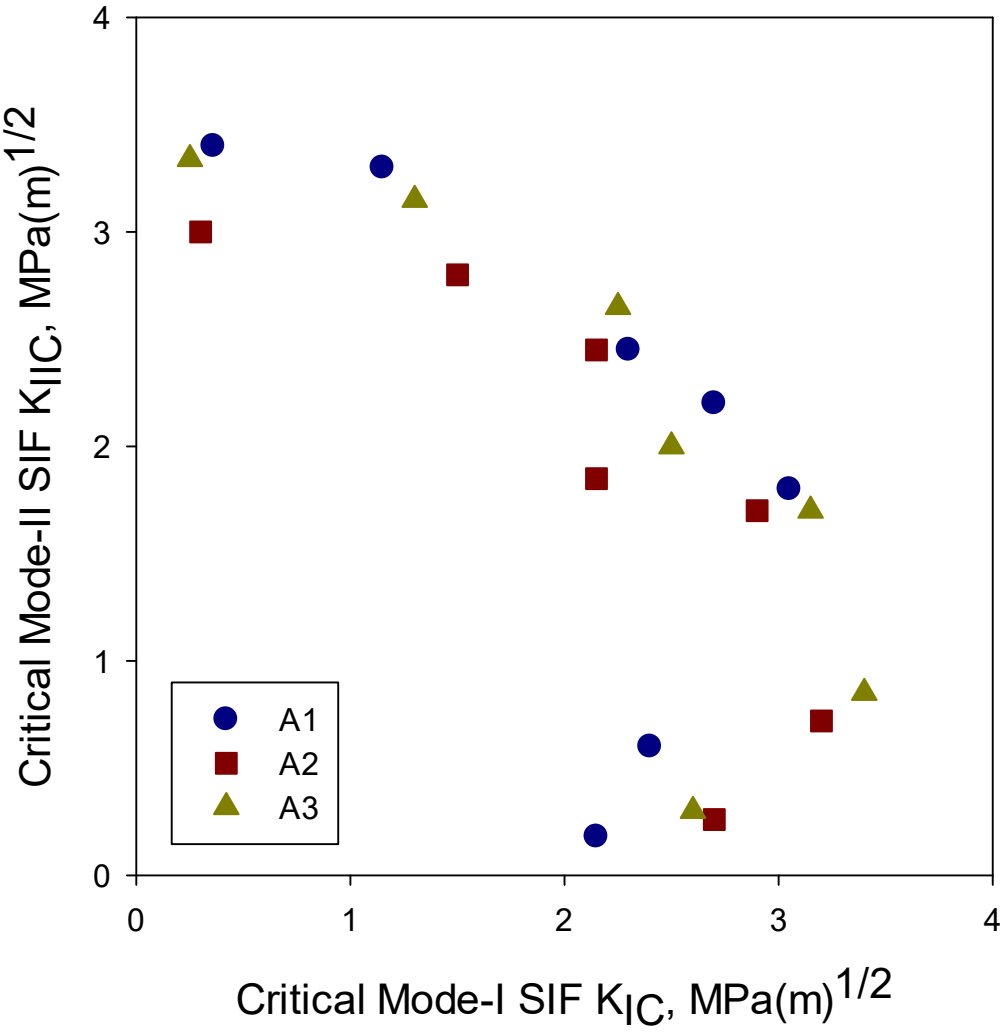

Figure 5.28: Repeatability of the fracture envelope of critical SIFs for the three architectures.

To explore the fracture mechanisms at play, optical images of the fractured specimen cross-sections (*x*-*z* plane) were captured. The fractured cross-sections for the A1 architectures tested at select angles of α = 0°, 45°, and 90° are shown in Figure 5.29. The pre-cut crack/notch is located at the top of each image. All three fractured cross-sections exhibited unstable/abrupt crack growth.

However, prior to crack initiation, a significant nonlinear response in both load and energy release rate histories were observed when α = 45° and 90°. As observed, the plastic deformation at the crack front caused by the material nonlinearity before crack initiation could be visualized through the highlighted regions in Figure 5.29. At the crack front, dense featureless regions could be observed for the 45° (mixed-mode) specimen, whereas clear regions with a distinct disbond between the layers could be observed for the 0° specimen (highlighted by the ellipse). In the 90° specimen (pure mode-II), featureless regions observed were tilted along a 45° direction. Also, thinning of layers was evident in the 0° specimen. This is highlighted by a boxed region in the figure. A clean boundary between the layers could be observed in case of α = 0° specimen. For α = 45° and 90° cases, the boundary was less sharp than the α = 0° counterpart.

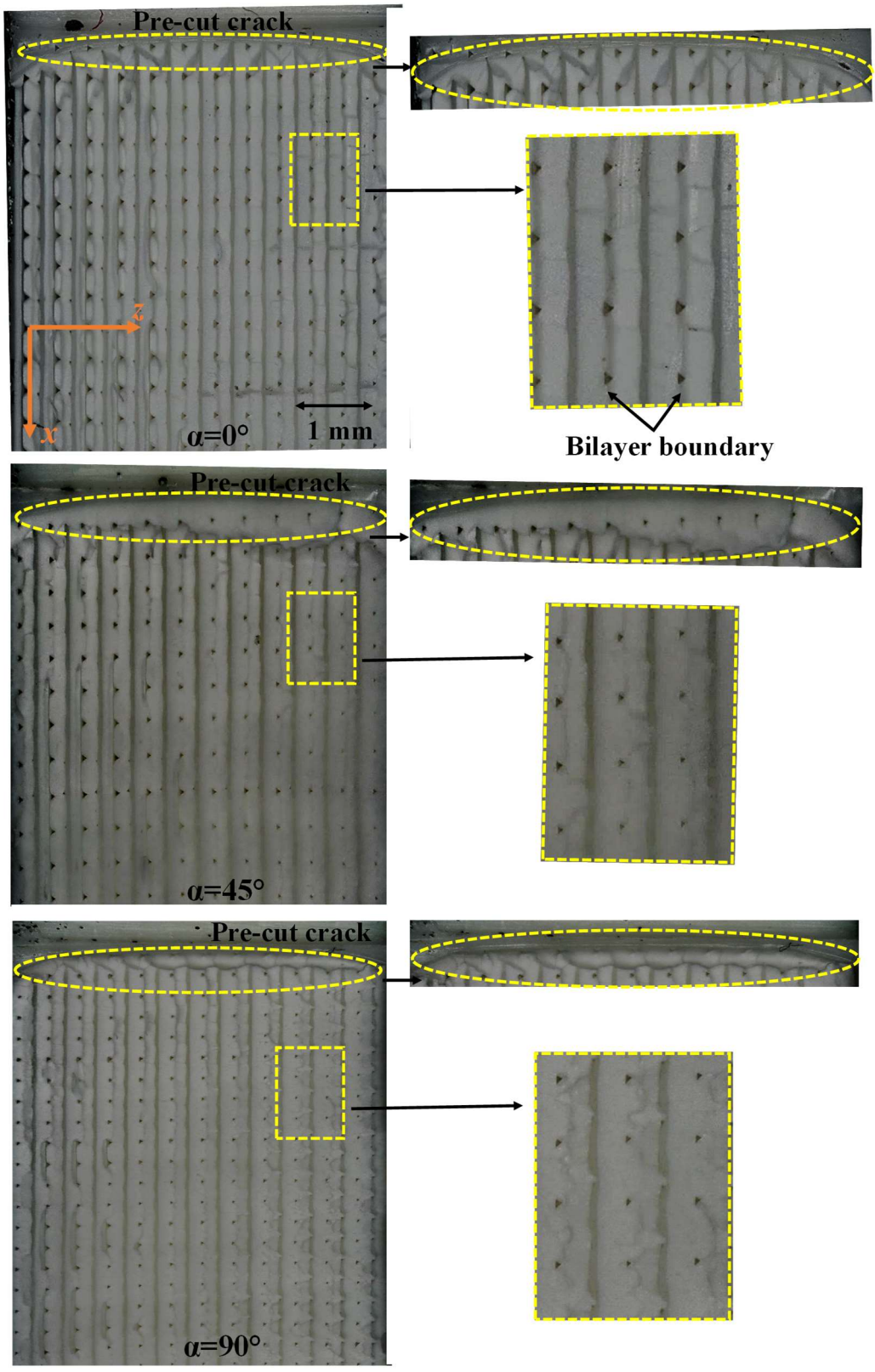

Figure 5.29: Fractured cross-sections for the A1 architecture specimens tested at α = 0°, 45°, and 90°. (The *x*-*z* plane shown is with respect to the crack tip coordinates)

The fractured cross-sections for the A2 architecture specimens tested at α = 0°, 45°, and 90° are shown in Figure 5.30. At α = 0° the A2 architecture had a linear response until crack initiation and a gradual drop in energy release rate with crack growth. The specimen tested at α = 0° had a clean boundary between the layers ahead of the crack front highlighted by the region enclosed by the ellipse corresponding to the linear response observed until crack initiation. Once the crack propagates, denser undulated regions were observed along the crack propagation direction indicating considerable amount of energy absorbed during crack growth. For the specimen tested at α = 45° loading angle, dense featureless region was observed ahead the notch front. Also, slow crack growth was observed for this specimen, and this was evident looking at the bilayer boundary as the boundary appears to have fused together. For the specimen tested at α = 90° loading angle, unstable crack growth was observed with a significant nonlinear energy release rate response before crack initiation. The denser regions ahead of the crack front are linked to the nonlinearity and the shiny texture of the -45°/45° layers could be attributed to observed unstable crack growth.

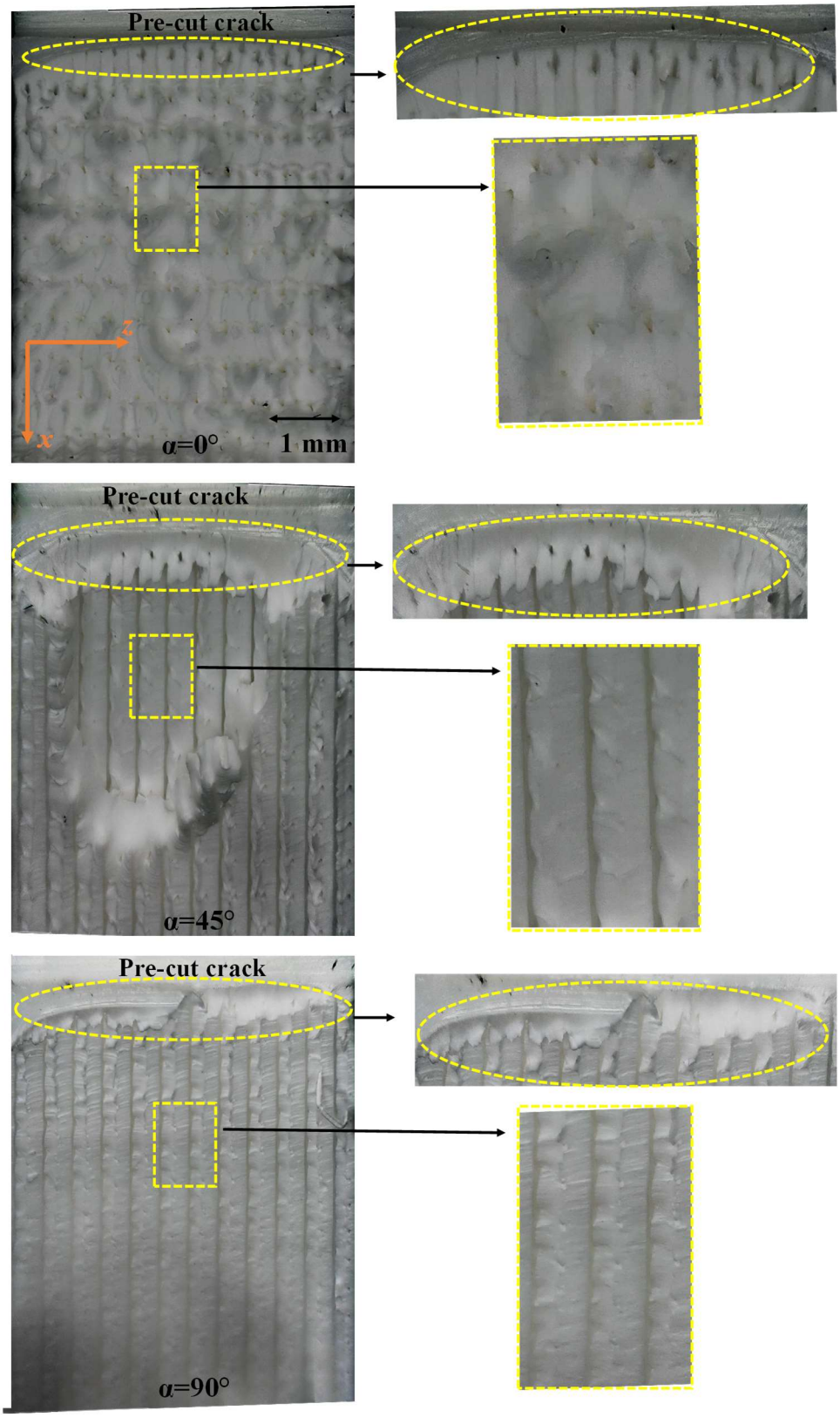

Figure 5.30: Fractured cross-sections for the A2 architecture specimens tested at α = 0°, 45°, and 90°. (The *x*-*z* plane shown is with respect to the crack tip coordinates)

The fractured cross-sections for the A3 architecture specimens tested at α = 0°, 45°, and 90° are shown in Figure 5.31. Similar to the previous two architectures, denser featureless regions could be observed ahead of the notch front for the specimens tested at α = 45° and 90° when compared to the one tested at 0°. The shear step pattern observed for the specimen at 0° loading angle could be attributed with the slow and stable crack growth exhibited by this specimen. Flat fracture surfaces observed for the α = 45° and 90° specimens correspond to the unstable crack growth that occurred in those specimens. An interesting phenomenon to be noted is that the shape of the deformed layers themselves appear to be the same for all three loading angles. In the A3 architecture specimen tested at α = 0°, primarily the 45°/90°/-45° layers support the load applied to the crack tip. In the specimen tested at α = 45°, the 90°/-45°/0° layers support the applied load. Specimen tested at α = 90° again has a similar fracture surface pattern as the one at α = 0° angle. To further simplify, the deformed four-layer pattern with clear boundaries appears in the same location in specimens tested α = 0° and 90° angles whereas a shift can be observed in the 45° specimen.

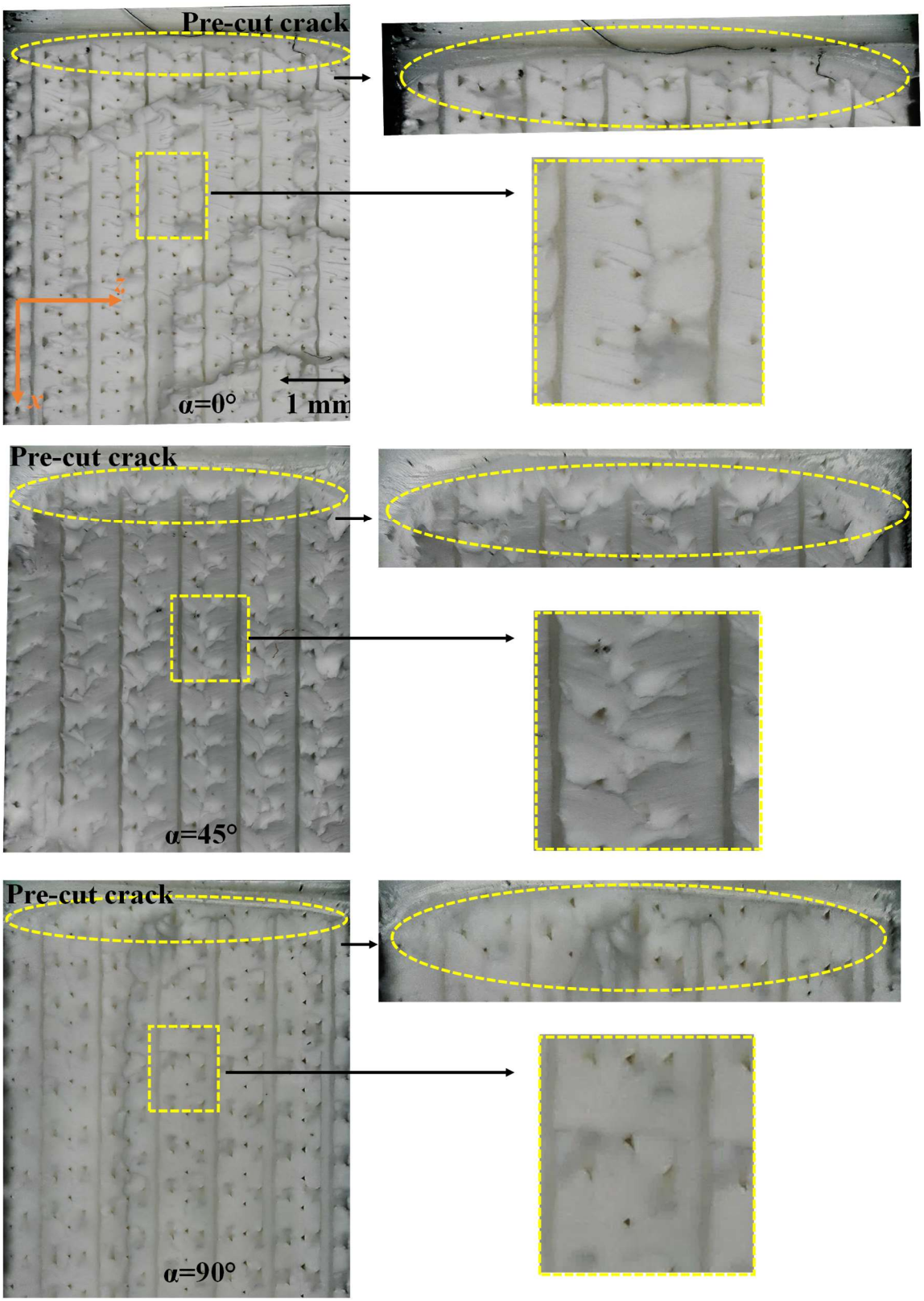

Figure 5.31: Fractured cross-sections for the A3 architecture specimens tested at α = 0°, 45°, and 90°. (The *x*-*z* plane shown is with respect to the crack tip coordinates)

5.5 Discussion

By comparing the energy release rates of all three architectures under pure mode-I and pure mode-II loading, it is evident that AM ABS has a better fracture toughness against in-plane shear loading when compared to pure tensile loading. This was expected and the results of unidirectional architectures (section 3.3.2) provide an insight as why this behavior is exhibited. The normal failure stress for the unidirectional architecture was found to be 34.8 MPa whereas the shear failure stress was 36.1 MPa. On the other hand, the shear strain at failure was ~23 %, ten times higher than the tensile failure strain of the 0° or 90° unidirectional architectures. For A1 architecture, the fracture performance improved when the loading angle changed from 0° to 15°. When α = 0°, only one layer in the bilayer architecture aids in energy absorption. At α = 15°, one layer still supports most of the load; however, the other layer aids in supporting shear load and hence higher energy absorption. At α = 30°, A1 architecture had its best fracture performance. Again, both layers aid in energy absorption and contribution of individual layers are better than in the 0° and 15° loading angles. Now at α = 45°, the expectation for A1 is to have its best fracture response but the contribution of mode-II being significant (ψ ~38°) and the weak layer (probable crack propagation layer) along the global 45° direction, the crack initiates well below the values observed for α = 30° loading angle.

The A2 architecture had its best response at α = 15°. The layers oriented at global 60° and -30° directions with the weak layer oriented at -45°/45° forces the crack to initiate and zig-zag along the two likely weak paths for crack growth. The crack paths in Figure 5.12 shows the crack initiation along -45° layer and the observed jagged crack path. Among the fracture behaviors observed in the presence of in-plane shear loading, A2 architecture had its lowest toughness values

for α = 45°. The weak layer oriented along the global 0°/90° provides a path with less resistance and hence, the lower values observed seem reasonable.

The A3 architecture had its best fracture performance in terms of crack initiation at α = 30°. This architecture, being a four-layer architecture, is a unique architecture with different mechanisms at play when compared to the A1 and A2 architectures. The A3 architecture at α = 0°, 45°, and 90° has three layers resisting crack growth whereas specimens tested at α = 15°, 30°, 60°, and 75° has all four layers aiding in resisting crack initiation and propagation. Also, relative to the A1 and A2 architectures, a more graceful/slow crack growth was observed for A3 as all four layers provide a probable crack path which in turn creates a jagged crack front compared to the two available in A1 and A2 architectures.

Typically, in mixed-mode fracture studies, validation of crack initiation angle based on theoretical criteria such as maximum tangential stress, strain energy density would be undertaken. However, considering the anisotropic nature of failure along the weak planes and the associated complexity, such a comparison is not attempted here.

Chapter 6. Conclusions

In this research, the role of print architecture on the fracture behavior of AM ABS is investigated with the aid of opto-mechanical characterization aided by DIC. Specifically, three print architectures, A1 or $[0^o/90^o]_n$, A2 or $[45^o/-45^o]_n$, and A3 or $[0^o/45^o/90^o/-45^o]_n$, are studied. The major outcomes of the work are itemized in the following:

- The optical method of 2D-DIC is extended for mapping crack tip deformations in 3D printed specimens in the whole field before crack initiation and during crack growth. A method of transferring optically measured displacement fields to companion finite element models as surface boundary conditions over the whole field for extracting failure parameters using an in-built domain integral algorithm for the *J*-integral evaluation is also conceived and demonstrated. Subsequently, individual SIFs are evaluated by computing the interaction integrals and adopting the mode-partitioning method using auxiliary fields.
- The tensile test results show that the printed parts of all three architectures are macroscopically isotropic in terms of their elastic properties within experimental errors. A follow-up ultrasonic evaluation further confirms this elastic isotropy. However, distinctly different failure stresses, failure strains, and fracture surface morphologies are observed in these three print architectures during tension tests. The ductility and toughness are higher for the A2 and A3 architectures when compared to the A1 counterparts. The higher failure strain is attributable to shear deformations evident from the failed specimen cross-section. The A3 architecture shows surprisingly higher ductility relative to A2. Synergistic constraint effects among different layers contribute to such an enhancement.
- The quasi-static fracture results show that the fracture toughness of A2 and A3 architectures are higher than the A1 counterpart. The results also demonstrate that ductility

and energy absorption during crack growth is higher for the above-said architectures. In addition, different failure modes and crack propagation paths are observed in these cases. The A2 architecture has the highest crack initiation toughness whereas the A3 counterpart has a marginally lower value but higher crack growth resistance. The crack growth is observed to be in a staircase pattern in the A2 architecture along ±45° planes whereas the crack growth is much more tortuous in the A3 counterpart due to crack growth along ±45° as well as 0° planes. The mechanics of these distinctly different failure behaviors are explained in terms of tension and shear tests performed on tensile and shear specimens with unidirectional print architectures. The high ductility seen in pure shear tests explains the failure behaviors seen in the fracture specimens.

- The high strain rate results are consistent with the quasi-static counterparts in terms of crack initiation toughness and crack growth resistance behaviors. That is, the A3 architecture outperforms its A2 and A1 counterparts, respectively, during crack growth. However, unlike the quasi-static fracture results, the tortuous staircase crack path pattern is not prominent in the high strain rate counterparts of the A3 architecture due to temporal limitations for the failure modes to manifest fully.
- An Arcan loading fixture that allows for optical measurements to be performed at the crack tip vicinity is developed for the mixed-mode fracture mechanics study of the three print architectures. The mixed-mode fracture behaviors of all three architectures are investigated under quasi-static loading conditions. Load vs. load-point displacement curves are obtained for the three architectures tested at seven different mode-mixities. The critical values at crack initiation are identified and fracture envelopes are plotted. The A3 architecture has the better fracture performance among the three architectures studied. Also, slow crack

propagation is observed for the A3 architecture in certain mixed-mode loading conditions for which unstable crack growth is observed for the respective A1 and A2 architectures.

- Fractured cross-sections are optically imaged, and the observed fracture response is corroborated with the captured microscopic features. Dense featureless regions are observed along the crack front for mode-II dominated loading conditions which are in line with the nonlinearity exhibited in the load and energy release rate histories prior to crack initiation in all three architectures. The fractured layers of A3 architecture behave uniformly under all loading conditions relative to the A1 and A2 counterparts where two layers depending upon the global layer direction affect the fracture performance.

6.1 Future work

The effect of mixed-mode loading on the high strain rate fracture behavior of AM ABS is worth exploring further. The resistance to in-plane shear loading which improved the fracture toughness of AM ABS under mixed-mode loading may not be able to influence the crack initiation and subsequent growth due to temporal limitations under high strain rate conditions.

This work has focused on improving the mechanical and fracture properties by designing different deposition paths. Although the $[0^o/45^o/90^o/-45^o]_n$ architecture had a better overall fracture profile, there might be many unexplored architectures with potential to have better mechanical and fracture responses. For example, developing bio-inspired architectures may result in unique topologies. Previously, manufacturing such architectures was impractical; however, with the freedom AM provides the user, the ability to manufacture biomimetic structures opens a range of possibilities. Architectural designs based on insect (cicada, dragonfly) wings, crustacean shells, and the internal structure of bone have been of interest in optimizing 2D and 3D topologies.

Material and failure characterization of such topologies may result in structures with improved performance over traditional structures.

Developing computational models that predict the response of FFF polymers must be a priority. With all the process parameters and numerous architectures involved with AM, it is simply not practical to test each possible combination. Tools such as machine learning and artificial intelligence could be incorporated into the computational models to use the available experimental results and improve the prediction accuracy for FFF polymers.

Hybrid DIC-FE is a robust method for extracting fracture properties from experimentally measured displacement fields. It provides unique advantages over the traditional method and can be successfully implemented to study other material systems, especially materials with an elasto-plastic behavior.

References

1. Technologies, A.C.F.o.A.M. and A.C.F.o.A.M.T.S.F.o. Terminology, *Standard terminology for additive manufacturing technologies*. 2012: Astm International.
2. Kodama, H., *Automatic method for fabricating a three-dimensional plastic model with photo-hardening polymer.* Review of scientific instruments, 1981. **52**(11): p. 1770-1773.
3. Hull, C.W., *The Birth of 3D Printing.* Research-Technology Management, 2015. **58**(6): p. 25-30.
4. Ligon, S.C., et al., *Polymers for 3D Printing and Customized Additive Manufacturing.* Chemical Reviews, 2017. **117**(15): p. 10212-10290.
5. Gradl, P.R. and C.S. Protz, *Technology advancements for channel wall nozzle manufacturing in liquid rocket engines.* Acta Astronautica, 2020. **174**: p. 148-158.
6. Markforged. *2020 additive manufacturing trends report*. 2020; Available from: https://markforged.com/additive-manufacturing-movement.
7. Mohamed, O.A., S.H. Masood, and J.L. Bhowmik, *Optimization of fused deposition modeling process parameters: a review of current research and future prospects.* Advances in Manufacturing, 2015. **3**(1): p. 42-53.
8. Osswald, T.A., J. Puentes, and J. Kattinger, *Fused filament fabrication melting model.* Additive Manufacturing, 2018. **22**: p. 51-59.
9. Bourell, D.L., D.W. Rosen, and M.C. Leu, *The Roadmap for Additive Manufacturing and Its Impact.* 3D Printing and Additive Manufacturing, 2014. **1**(1): p. 6-9.
10. Ahn, S.H., et al., *Anisotropic material properties of fused deposition modeling ABS.* Rapid Prototyping Journal, 2002. **8**(4): p. 248-257.
11. Al-Maharma, A.Y. and P. Sendur, *Review of the main factors controlling the fracture toughness and impact strength properties of natural composites.* Materials Research Express, 2018. **6**(2): p. 022001.
12. Dizon, J.R.C., et al., *Mechanical characterization of 3D-printed polymers.* Additive Manufacturing, 2018. **20**: p. 44-67.
13. Van de Velde, K. and P. Kiekens, *Biopolymers: overview of several properties and consequences on their applications.* Polymer Testing, 2002. **21**(4): p. 433-442.
14. Poh, P.S.P., et al., *Polylactides in additive biomanufacturing.* Advanced Drug Delivery Reviews, 2016. **107**: p. 228-246.
15. Riddick, J.C., et al., *Fractographic analysis of tensile failure of acrylonitrile-butadiene-styrene fabricated by fused deposition modeling.* Additive Manufacturing, 2016. **11**: p. 49-59.
16. Akiyama, H., M. Uchida, and Y. Kaneko. *Evaluation of effect of sample size and layer direction on mechanical property of specimen manufactured by FDM-type 3D printer*. 2019. Trans Tech Publ.
17. Gardan, J., A. Makke, and N. Recho, *A Method to Improve the Fracture Toughness Using 3D Printing by Extrusion Deposition.* Procedia Structural Integrity, 2016. **2**: p. 144-151.
18. Lanzillotti, P., et al., *Enhancement of fracture toughness under mixed mode loading of ABS specimens produced by 3D printing.* Rapid Prototyping Journal, 2019.
19. Papon, E.A. and A. Haque, *Fracture toughness of additively manufactured carbon fiber reinforced composites.* Additive Manufacturing, 2019. **26**: p. 41-52.

20. Jia, Z. and L. Wang, *3D printing of biomimetic composites with improved fracture toughness.* Acta Materialia, 2019. **173**: p. 61-73.
21. McLouth, T.D., et al., *The impact of print orientation and raster pattern on fracture toughness in additively manufactured ABS.* Additive Manufacturing, 2017. **18**: p. 103-109.
22. Aliheidari, N., et al., *Fracture resistance measurement of fused deposition modeling 3D printed polymers.* Polymer Testing, 2017. **60**: p. 94-101.
23. Dickson, A.N. and D.P. Dowling, *Enhancing the bearing strength of woven carbon fibre thermoplastic composites through additive manufacturing.* Composite Structures, 2019. **212**: p. 381-388.
24. De León, A.S., A. Domínguez-Calvo, and S.I. Molina, *Materials with enhanced adhesive properties based on acrylonitrile-butadiene-styrene (ABS)/thermoplastic polyurethane (TPU) blends for fused filament fabrication (FFF).* Materials & Design, 2019. **182**: p. 108044.
25. Young, D., N. Wetmore, and M. Czabaj, *Interlayer fracture toughness of additively manufactured unreinforced and carbon-fiber-reinforced acrylonitrile butadiene styrene.* Additive Manufacturing, 2018. **22**: p. 508-515.
26. Rabbi, M.F., V.B. Chalivendra, and D. Li, *A Novel Approach to Increase Dynamic Fracture Toughness of Additively Manufactured Polymer.* Experimental Mechanics, 2019. **59**(6): p. 899-911.
27. Samykano, M., et al., *Mechanical property of FDM printed ABS: influence of printing parameters.* The International Journal of Advanced Manufacturing Technology, 2019. **102**(9): p. 2779-2796.
28. Hart, K.R. and E.D. Wetzel, *Fracture behavior of additively manufactured acrylonitrile butadiene styrene (ABS) materials.* Engineering Fracture Mechanics, 2017. **177**: p. 1-13.
29. Sharafi, S., et al., *A review of factors that influence the fracture toughness of extrusion-based additively manufactured polymer and polymer composites.* Additive Manufacturing, 2021. **38**: p. 101830.
30. Vairis, A., et al., *On the Strain Rate Sensitivity of Abs and Abs Plus Fused Deposition Modeling Parts.* Journal of Materials Engineering and Performance, 2016. **25**(9): p. 3558-3565.
31. Vidakis, N., et al., *On the strain rate sensitivity of fused filament fabrication (Fff) processed pla, abs, petg, pa6, and pp thermoplastic polymers.* Polymers, 2020. **12**(12): p. 2924.
32. Verbeeten, W.M.H., R.J. Arnold-Bik, and M. Lorenzo-Bañuelos, *Print velocity effects on strain-rate sensitivity of acrylonitrile-butadiene-styrene using material extrusion additive manufacturing.* Polymers, 2021. **13**(1): p. 149.
33. Lee, W.S. and H.C. Shen, *Comparisons of deformation and fracture behaviour of PC/ABS blend and ABS copolymer under dynamic shear loading.* Materials science and technology, 2004. **20**(1): p. 8-15.
34. Peterson, A., et al. *Dynamic Behavior of Acrylonitrile Butadiene Styrene Under Impact Loads*. 2015. American Society of Mechanical Engineers.
35. Bahrami, B., et al., *The effect of in-plane layer orientation on mixed-mode I-II fracture behavior of 3D-printed poly-carbonate specimens.* Engineering Fracture Mechanics, 2020. **231**: p. 107018.

36. Ameri, B., F. Taheri-Behrooz, and M.R.M. Aliha, *Mixed-mode tensile/shear fracture of the additively manufactured components under dynamic and static loads.* Engineering Fracture Mechanics, 2022. **260**: p. 108185.
37. Șerban, D.-A., et al. *A Study of Yielding and Plasticity of Rapid Prototyped ABS*. Mathematics, 2021. **9**, DOI: 10.3390/math9131495.
38. Arcan, M., Z.a. Hashin, and A. Voloshin, *A method to produce uniform plane-stress states with applications to fiber-reinforced materials.* Experimental mechanics, 1978. **18**(4): p. 141-146.
39. Banks-Sills, L., M. Arcan, and Y. Bortman, *A mixed mode fracture specimen for mode II dominant deformation.* Engineering fracture mechanics, 1984. **20**(1): p. 145-157.
40. Mohr, D. and M. Doyoyo, *Analysis of the Arcan apparatus in the clamped configuration.* Journal of Composite Materials, 2002. **36**(22): p. 2583-2594.
41. Torun, A.R., Ş.H. Kaya, and N. Choupani, *Mixed-mode fracture behavior of 3D-printed PLA with zigzag filling.* Green Materials, 2020. **9**(1): p. 29-36.
42. Oskui, A.E.h., N. Choupani, and E. Haddadi, *Experimental and numerical investigation of fracture of ABS polymeric material for different sample's thickness using a new loading device.* Polymer Engineering & Science, 2014. **54**(9): p. 2086-2096.
43. Boğa, C., *Investigation of mechanical and fracture behavior of pure and carbon fiber reinforced ABS samples processed by fused filament fabrication process.* Rapid Prototyping Journal, 2021.
44. Schnittker, K., et al., *Integrating digital image correlation in mechanical testing for the materials characterization of big area additive manufacturing feedstock.* Additive Manufacturing, 2019. **26**: p. 129-137.
45. Kishore, V., et al., *Infrared preheating to improve interlayer strength of big area additive manufacturing (BAAM) components.* Additive Manufacturing, 2017. **14**: p. 7-12.
46. Duty, C.E., et al., *Structure and mechanical behavior of Big Area Additive Manufacturing (BAAM) materials.* Rapid Prototyping Journal, 2017. **23**(1): p. 181-189.
47. Zhang, Z., et al., *Effect of build orientation and raster pattern on the fracture behavior of carbon fiber reinforced polymer composites fabricated by additive manufacturing.* Additive Manufacturing, 2021. **47**: p. 102204.
48. Pan, B., et al., *Two-dimensional digital image correlation for in-plane displacement and strain measurement: a review.* Measurement Science and Technology, 2009. **20**(6): p. 062001.
49. Lee, D., et al., *Experimental Study of Dynamic Crack Growth in Unidirectional Graphite/Epoxy Composites using Digital Image Correlation Method and High-speed Photography.* Journal of Composite Materials, 2009. **43**(19): p. 2081-2108.
50. Kirugulige, M.S. and H.V. Tippur, *Measurement of Fracture Parameters for a Mixed-Mode Crack Driven by Stress Waves using Image Correlation Technique and High-Speed Digital Photography.* Strain, 2009. **45**(2): p. 108-122.
51. Kirugulige, M.S., H.V. Tippur, and T.S. Denney, *Measurement of transient deformations using digital image correlation method and high-speed photography: application to dynamic fracture.* Applied Optics, 2007. **46**(22): p. 5083-5096.
52. Bruck, H.A., et al., *Digital image correlation using Newton-Raphson method of partial differential correction.* Experimental Mechanics, 1989. **29**(3): p. 261-267.

53. Yoneyama, S., T. Ogawa, and Y. Kobayashi, *Evaluating mixed-mode stress intensity factors from full-field displacement fields obtained by optical methods.* Engineering fracture mechanics, 2007. **74**(9): p. 1399-1412.
54. Jajam, K.C. and H.V. Tippur, *An experimental investigation of dynamic crack growth past a stiff inclusion.* Engineering Fracture Mechanics, 2011. **78**(6): p. 1289-1305.
55. Bedsole, R.W., P.B. Bogert, and H.V. Tippur, *An experimental investigation of interlaminar and intralaminar dynamic fracture of CFRPs: Effect of matrix modification using carbon nanotubes.* Composite Structures, 2015. **132**: p. 1043-1055.
56. Nishioka, T. and S.N. Atluri, *Path-independent integrals, energy release rates, and general solutions of near-tip fields in mixed-mode dynamic fracture mechanics.* Engineering Fracture Mechanics, 1983. **18**(1): p. 1-22.
57. Williams, M.L., *On the stress distribution at the base of a stationary crack.* 1957.
58. Kobayashi, A., *Handbook on experimental mechanics.* Englewood Cliffs, NJ, Prentice-Hall, Inc., 1987, 1020, 1987.
59. Jayadevan, K.R., et al., *A numerical study of T-stress in dynamically loaded fracture specimens.* International Journal of Solids and structures, 2001. **38**(28-29): p. 4987-5005.
60. Cherepanov, G.P., *Crack propagation in continuous media: PMM vol. 31, no. 3, 1967, pp. 476–488.* Journal of Applied Mathematics and Mechanics, 1967. **31**(3): p. 503-512.
61. Rice, J.R., *A Path Independent Integral and the Approximate Analysis of Strain Concentration by Notches and Cracks.* Journal of Applied Mechanics, 1968. **35**(2): p. 379-386.
62. Xu, L. and H.V. Tippur, *Fracture parameters for interfacial cracks: an experimental-finite element study of crack tip fields and crack initiation toughness.* International Journal of Fracture, 1995. **71**(4): p. 345-363.
63. Shih, C.F. and R.J. Asaro, *Elastic-Plastic Analysis of Cracks on Bimaterial Interfaces: Part I—Small Scale Yielding.* Journal of Applied Mechanics, 1988. **55**(2): p. 299-316.
64. Gao, H., M. Abbudi, and D.M. Barnett, *Interfacial crack-tip field in anisotropic elastic solids.* Journal of the Mechanics and Physics of Solids, 1992. **40**(2): p. 393-416.
65. Barnett, D.M. and R.J. Asaro, *The fracture mechanics of slit-like cracks in anisotropic elastic media.* Journal of the Mechanics and Physics of Solids, 1972. **20**(6): p. 353-366.
66. Suo, Z. and R. Hill, *Singularities, interfaces and cracks in dissimilar anisotropic media.* Proceedings of the Royal Society of London. A. Mathematical and Physical Sciences, 1990. **427**(1873): p. 331-358.
67. O'Dowd, N.P., C.F. Shih, and M.G. Stout, *Test geometries for measuring interfacial fracture toughness.* International Journal of Solids and Structures, 1992. **29**(5): p. 571-589.
68. Jhaver, R. and H. Tippur, *Processing, compression response and finite element modeling of syntactic foam based interpenetrating phase composite (IPC).* Materials Science and Engineering: A, 2009. **499**(1): p. 507-517.
69. Hopkinson, B., *X. A method of measuring the pressure produced in the detonation of high, explosives or by the impact of bullets.* Philosophical Transactions of the Royal Society of London. Series A, Containing Papers of a Mathematical or Physical Character, 1914. **213**(497-508): p. 437-456.
70. Kolsky, H., *An investigation of the mechanical properties of materials at very high rates of loading.* Proceedings of the physical society. Section B, 1949. **62**(11): p. 676.

71. Fett, T., *Mixed-mode stress intensity factors for three-point bending bars.* International journal of fracture, 1991. **48**(4): p. R67-R74.
72. Fett, T., et al., *Fracture tests for ceramics under mode-I, mode-II and mixed-mode loading.* Journal of the European Ceramic Society, 1995. **15**(4): p. 307-312.
73. Suresh, S., et al., *Mixed-mode fracture toughness of ceramic materials.* Journal of the American Ceramic Society, 1990. **73**(5): p. 1257-1267.
74. Belli, R., et al., *Mixed-mode fracture toughness of texturized LS2 glass-ceramics using the three-point bending with eccentric notch test.* Dental Materials, 2017. **33**(12): p. 1473-1477.
75. Fett, T., *Stress intensity factors for edge crack subjected to mixed mode four-point bending.* Theoretical and applied fracture mechanics, 1991. **15**(1): p. 99-104.
76. Maccagno, T.M. and J.F. Knott, *The low temperature brittle fracture behaviour of steel in mixed modes I and II.* Engineering Fracture Mechanics, 1991. **38**(2): p. 111-128.
77. Gálvez, J.C., et al., *Mixed Mode Fracture of Concrete under Proportional and Nonproportional Loading.* International Journal of Fracture, 1998. **94**(3): p. 267-284.
78. Lim, I.L., et al., *Fracture testing of a soft rock with semi-circular specimens under three-point bending. Part 1—mode I.* International Journal of Rock Mechanics and Mining Sciences & Geomechanics Abstracts, 1994. **31**(3): p. 185-197.
79. Lim, I.L., et al., *Fracture testing of a soft rock with semi-circular specimens under three-point bending. Part 2—mixed-mode.* International Journal of Rock Mechanics and Mining Sciences & Geomechanics Abstracts, 1994. **31**(3): p. 199-212.
80. Ayatollahi, M.R., M.R.M. Aliha, and M.M. Hassani, *Mixed mode brittle fracture in PMMA—An experimental study using SCB specimens.* Materials Science and Engineering: A, 2006. **417**(1): p. 348-356.
81. Ayatollahi, M.R. and M.R.M. Aliha, *On determination of mode II fracture toughness using semi-circular bend specimen.* International Journal of Solids and Structures, 2006. **43**(17): p. 5217-5227.
82. Owens, A.T. and H.V. Tippur, *Measurement of mixed-mode fracture characteristics of an epoxy-based adhesive using a hybrid digital image correlation (DIC) and finite elements (FE) approach.* Optics and Lasers in Engineering, 2021. **140**: p. 106544.
83. Theocaris, P.S. and G.A. Papadopoulos, *The influence of geometry of edge-cracked plates on KI and KII components of the stress intensity factor, studied by caustics.* Journal of Physics D: Applied Physics, 1984. **17**(12): p. 2339.
84. Cho, S.W., K. Jonnalagadda, and I. Chasiotis, *Mode I and mixed mode fracture of polysilicon for MEMS.* Fatigue & Fracture of Engineering Materials & Structures, 2007. **30**(1): p. 21-31.
85. Singh, D. and D.K. Shetty, *Fracture toughness of polycrystalline ceramics in combined mode I and mode II loading.* Journal of the American Ceramic Society, 1989. **72**(1): p. 78-84.
86. Scherrer, S.S., et al., *Fracture toughness of aged dental composites in combined mode I and mode II loading.* Journal of Biomedical Materials Research: An Official Journal of The Society for Biomaterials, The Japanese Society for Biomaterials, and The Australian Society for Biomaterials and the Korean Society for Biomaterials, 2000. **53**(4): p. 362-370.
87. Choupani, N., *Mixed-mode cohesive fracture of adhesive joints: Experimental and numerical studies.* Engineering Fracture Mechanics, 2008. **75**(15): p. 4363-4382.

88. Duncan, B.C. and G. Dean, *Test methods for determining shear property data for adhesives suitable for design. Part 1: Notched-beam shear (Iosipescu) and notched-plate shear (Arcan) methods for bulk and joint test specimens. Part A: Summary.* 1996.
89. Greer Jr, J.M., S.E.G. Dorman, and M.J. Hammond, *Some comments on the Arcan mixed-mode (I/II) test specimen.* Engineering Fracture Mechanics, 2011. **78**(9): p. 2088-2094.
90. Sutton, M.A., et al., *A combined modeling–experimental study of the crack opening displacement fracture criterion for characterization of stable crack growth under mixed mode I/II loading in thin sheet materials.* Engineering Fracture Mechanics, 2000. **66**(2): p. 171-185.
91. Chakherlou, T.N., et al., *Experimental and numerical investigations of crack face adhesive bonding effect on the mixed-mode fracture strength of PMMA.* Journal of adhesion science and Technology, 2016. **30**(20): p. 2236-2256.
92. Alizadeh, F. and C.G. Soares, *Experimental and numerical investigation of the fracture toughness of Glass/Vinylester composite laminates.* European Journal of Mechanics-A/Solids, 2019. **73**: p. 204-211.
93. Moradi, E. and A. Zeinedini, *On the mixed mode I/II/III inter-laminar fracture toughness of cotton/epoxy laminated composites.* Theoretical and Applied Fracture Mechanics, 2020. **105**: p. 102400.
94. Zeinedini, A., *A novel fixture for mixed mode I/II/III fracture testing of brittle materials.* Fatigue & Fracture of Engineering Materials & Structures, 2019. **42**(4): p. 838-853.

Appendix A

A.1 Supplementary plots

To execute as elasto-plastic analysis using the hybrid DIC-FE approach, Abaqus requires the true stress-strain response of the material. The computed true stress-strain response for the three architectures is shown in Figure A1.

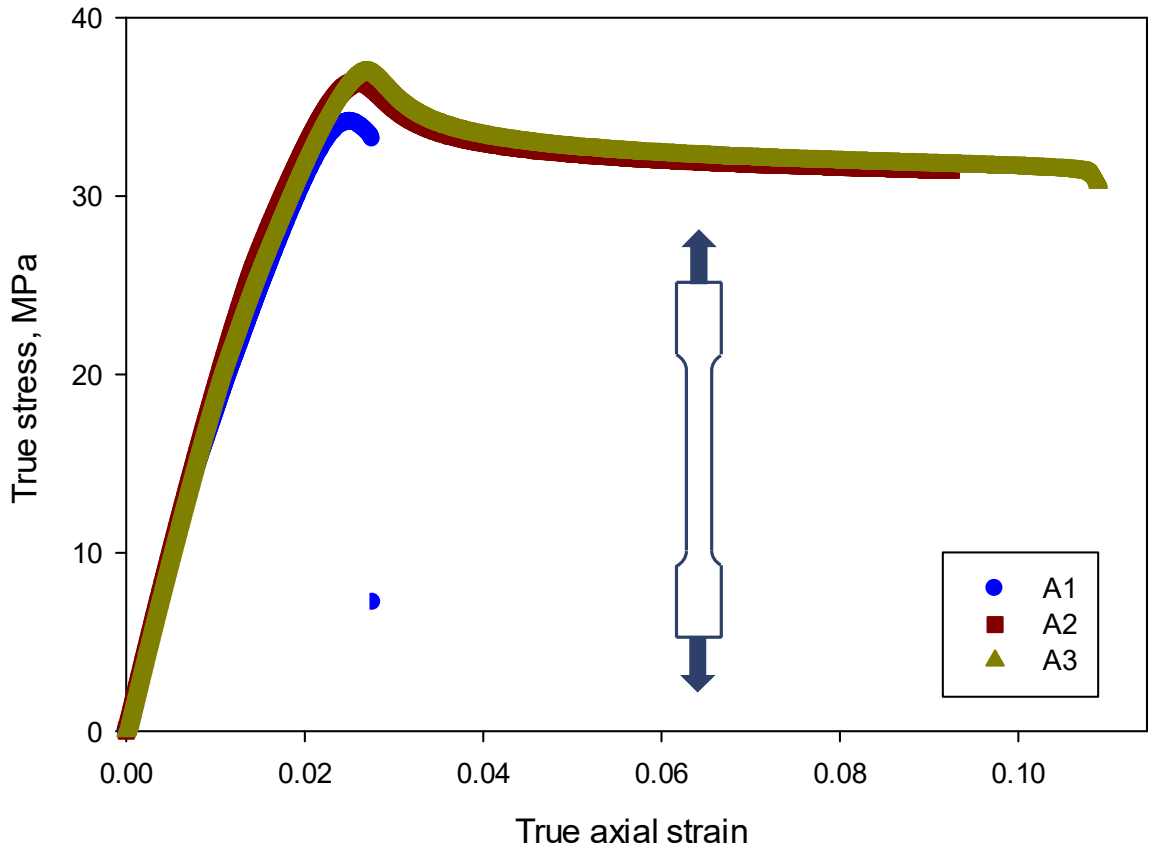

Figure A1: True stress-strain responses of dog-bone specimens of different print architectures.